ARIZONA STATE UNIVERSITY 1885 1985
ASU
EXCELLENCE FOR A NEW CENTURY

DEVELOPMENT OF HARMONIC PANEL METHODS FOR AEROELASTIC APPLICATIONS TO ELASTIC BODIES AND BODY-FIN COMBINATIONS IN SUPERSONIC FLOW

D. D. Liu and Pablo Garcia-Fogeda

Mechanical and Aerospace Engineering
Arizona State University
Tempe, AZ 85287-6106

January 1989

FINAL REPORT
Prepared for U.S. Army Research Office
under Contract DAAG 29-84-K-0004

ASU Report CR-R-89021

UNCLASSIFIED
SECURITY CLASSIFICATION OF THIS PAGE

MASTER COPY - FOR REPRODUCTION PURPOSES

REPORT DOCUMENTATION PAGE

1a. REPORT SECURITY CLASSIFICATION: Unclassified	1b. RESTRICTIVE MARKINGS
2a. SECURITY CLASSIFICATION AUTHORITY	3. DISTRIBUTION / AVAILABILITY OF REPORT: Approved for public release; distribution unlimited.
2b. DECLASSIFICATION / DOWNGRADING SCHEDULE	
4. PERFORMING ORGANIZATION REPORT NUMBER(S): CR-R-89021	5. MONITORING ORGANIZATION REPORT NUMBER(S): ARO 20928.6-EG
6a. NAME OF PERFORMING ORGANIZATION: Department of Mechanical and Aerospace Engineering; 6b. OFFICE SYMBOL (If applicable): MAE	7a. NAME OF MONITORING ORGANIZATION: U. S. Army Research Office
6c. ADDRESS (City, State, and ZIP Code): Arizona State University, Tempe, AZ 85287	7b. ADDRESS (City, State, and ZIP Code): P. O. Box 12211, Research Triangle Park, NC 27709-2211
8a. NAME OF FUNDING / SPONSORING ORGANIZATION: U. S. Army Research Office; 8b. OFFICE SYMBOL (If applicable)	9. PROCUREMENT INSTRUMENT IDENTIFICATION NUMBER: DAAG29-84-K-0004
8c. ADDRESS (City, State, and ZIP Code): P. O. Box 12211, Research Triangle Park, NC 27709-2211	10. SOURCE OF FUNDING NUMBERS — PROGRAM ELEMENT NO. / PROJECT NO. / TASK NO. / WORK UNIT ACCESSION NO

11. TITLE (Include Security Classification)
Development of Harmonic Potential Panel Methods for Aeroelastic Applications to Elastic Bodies and Body-Fin Combinations in Supersonic Flow

12. PERSONAL AUTHOR(S)
D.D.Liu and Pablo Garcia-Fogeda

13a. TYPE OF REPORT	13b. TIME COVERED	14. DATE OF REPORT (Year, Month, Day)	15. PAGE COUNT
Final Report	FROM 8401 TO 8812	1989 January	

16. SUPPLEMENTARY NOTATION
The view, opinions and/or findings contained in this report are those of the author(s) and should not be construed as an official Department of the Army position, policy, or decision, unless so designated by other documentation.

17. COSATI CODES		
FIELD	GROUP	SUB-GROUP

18. SUBJECT TERMS (Continue on reverse if necessary and identify by block number)
Unsteady Aerodynamics, Supersonic Flow, Aeroelasticity

19. ABSTRACT (Continue on reverse if necessary and identify by block number)

Recent development of several unsteady supersonic methods for computations of airloads for elastic bodies of revolution, asymmetric bodies and body-wing configurations are reported. These methods include the Harmonic Potential Panel (HPP) method, the Bundle Triplet Method (BTM) and the combined method of BTM and the Harmonic Gradient Method (HGM) for body-wing combinations. All methods are based on the generic Harmonic-Gradient (H-G) model, which is essential in providing accurate solutions in the full frequency domain and the low Mach number range.

Extensive comparisons of computed results obtained from these methods show good correlations with existing data. Comparison examples range from simple cones and ogive bodies to Saturn SA-1 configuration, to the cylindrical panel membrance and to the NACA wing-body combinations.

(see reverse side)

20. DISTRIBUTION / AVAILABILITY OF ABSTRACT	21. ABSTRACT SECURITY CLASSIFICATION
☐ UNCLASSIFIED/UNLIMITED ☐ SAME AS RPT. ☐ DTIC USERS	Unclassified
22a. NAME OF RESPONSIBLE INDIVIDUAL	22b. TELEPHONE (Include Area Code) / 22c. OFFICE SYMBOL

(Block 19 continued)

Cases computed yield steady and unsteady pressures, generalized forces, stability derivatives, aerodynamic dampings and divergence and flutter boundaries for these configurations.

The developed methods have been validated with existing theories or measured data. For supersonic aeroelastic analysis, these methods yield results that are accurate and cost-effective, thus rendering them very favorable for technology transfer and industry applications.

FORWARD

This research effort was conducted from January 1984 to December 1988 in the Department of Mechanical and Aerospace Engineering, Arizona State University, under the sponsorship of the Army Research Office (ARO), contract number DAAG29-84-K-0004. Dr. D.D. Liu was the principal investigator and Mr. Pablo Garcia-Fogeda was the Graduate Research Assistant in the first and the second phases of the contract. In 1987, Mr. Garcia-Fogeda obtained his Doctorate from ASU, and since then he has been the co-investigator in the third phase of the contract. Dr. Garcia-Fogeda is now an assistant professor of University of Madrid, Spain.

This contract was monitored by Dr. Robert E. Singleton and Dr. Thomas Daligalski of ARO.

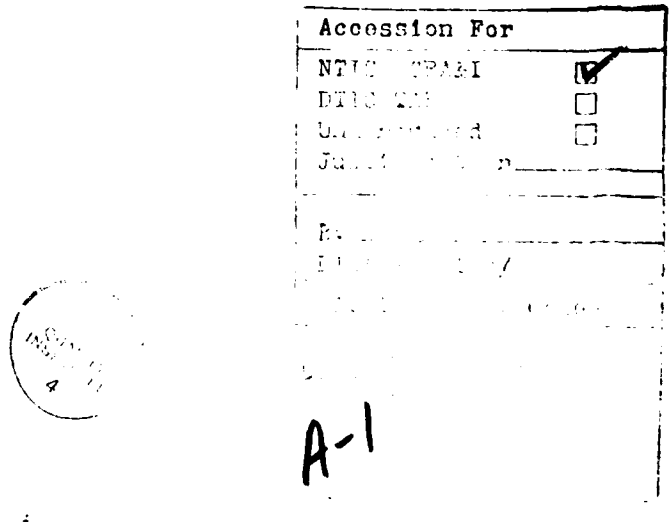

ABSTRACT

Recent development of several unsteady supersonic methods for computations of airloads for elastic bodies of revolution, asymmetric bodies and body-wing configurations are reported. These methods include the Harmonic Potential Panel (HPP) method, the Bundle Triplet Method (BTM) and the combined method of BTM and the Harmonic Gradient Method (HGM) for body-wing combinations. All methods are based on the generic Harmonic-Gradient (H-G) model, which is essential in providing accurate solutions in the full frequency domain and the low Mach number range.

Extensive comparisons of computed results obtained from these methods show good correlations with existing data. Comparison examples range from simple cones and ogive bodies to Saturn SA-1 configuration, to the cylindrical panel membrance and to the NACA wing-body combinations. Cases computed yield steady and unsteady pressures, generalized forces, stability derivatives, aerodynamic dampings and divergence and flutter boundaries for these configurations.

The developed methods have been validated with existing theories or measured data. For supersonic aeroelastic analysis, these methods yield results that are accurate and cost-effective, thus rendering them very favorable for technology transfer and industry applications.

TABLE OF CONTENTS

LIST OF FIGURES

NOMENCLATURE

Symbol	Definition
a	speed of sound
C_{M_α}	pitching moment coefficient
$C_{M_{\dot{\alpha}}+C_{M_q}}$	damping-in-pitch moment coefficient
C_p	pressure coefficient, $\frac{P - P_\infty}{1/2\rho_\infty U_\infty^2}$
C^0_p	mean flow pressure coefficient
C^1_p	unsteady flow pressure coefficient
$F(\xi)$	dipole strength distribution
$f(\xi)$	source strength distribution
$f_n(\xi)$	vortex multiplets strength distribution
$g(x)$	normalized natural mode shape
$h(t)$	generalized coordinate for plunging oscillation
$h(x,t')$	instantaneous normal displacement of the body
I_α	mass moment of inertia of the body
K_h	stiffness of the body in plunging
K_α	stiffness of the body in pitching
k	reduced frequency, $\frac{\omega L}{U_\infty}$
L	body length (dimensional)
M_∞	free-stream Mach number
m	total mass of the body
$\vec{n}$	outward normal to the body surface
$p(x)$	normalized natural mode shape expressed in the pseudo-wind-fixed coordinate system

Q_{IJ}	generalized forces
R	body radius
r_α	dimensionless radius of gyration about pitch axis, $\sqrt{\frac{I_\alpha}{mL^2}}$
S = 0	body surface
S_α	static moment of the body
t	time measured in a body-fixed reference frame
t'	time measured in a wind-fixed reference frame
U_∞	free-stream speed (dimensional)
$\vec{V}$	total velocity vector
$\vec{V}_B$	velocity vector of the body surface
x_G	pitching axis location of the body
x, r, θ	body-fixed cylindrical coordinates
x, y, z	body-fixed cartesian coordinates
x', r', θ'	wind-fixed cylindrical coordinates
x', y', z'	wind-fixed cartesian coordinates

Greek Symbols

$\alpha(t)$	generalized coordinate for pitching oscillation
β	$\sqrt{M_\infty^2 - 1}$
γ	ratio of specific heats
$\delta(t')$	instantaneous amplitude of oscillation
δ_o	amplitude of oscillation
λ	flexible part of the unsteady flow potential in the pseudo-wind-fixed coordinate system
ξ	source of dipole coordinate
ρ_∞	free-stream density

Φ	complete time-dependent perturbation potential
ϕ_o	mean flow perturbation potential
ϕ_o	mena flow first-order iteration potential
ϕ_1	cross flow perturbation potential
X_o	homogeneous solution for the mean flow second-order iteration equation
ψ	rigid part of the unsteady flow potential in the pseudo-wind-fixed coordinate system
ψ_o	particular solution to the mean flow second-order iteration equation
Ω	full potential
ω	frequency of oscillation (dimensional)
ω_h	uncoupled angular frequency in vertical translation
ω_α	uncoupled angular pitching frequency
∇	gradient operator
∇^2	Laplacian operator
$\nabla\cdot$	divergence operator

Subscripts and Superscripts

$()', ()'', \text{etc.}$	derivatives with respect to the independent variable
$()_{x,r,\theta,t}$	partial derivatives
$(\cdot)$	defivative with respect to time

CHAPTER 1

INTRODUCTION

Long slender missiles or rockets at cruising supersonic speeds are susceptible to a number of aeroelastic instabilities. First, it is known that the stability and control characteristics of high speed flexible bodies may be significantly influenced by the distortion of the structure under transient loading conditions. Second, the body/fin configurations are likely to flutter as a result of the properly phased short-period rigid body-fin mode and the body bending mode. In fact, the earlier flutter incident of the British JTVI ramjet missile in 1955, as shown in Figs. 1 and 2, is one such example (Ref. 1). Furthermore, the problem of the store-airframe interaction, during the cruise and/or maneuver phase, of modern aircraft has been a major concern for design and performance. The effects of this type of interaction could sometimes change the airload, and hence the wing flutter characteristics, rather drastically. For example, problems such as stores in pitch-yaw combined oscillations and the tip-missile influence are among the critical factors related to aircraft flutter. Clearly, the prediction of these boundaries relies almost exclusively on the unsteady aerodynamic inputs. The objective of the present work is therefore to provide a generalized Harmonic Potential Panel (HPP) method for computing the unsteady aerodynamics of arbitrary flexible bodies and body-fin configurations in the supersonic flow regime.

1.1 Survey of Literature

Currently, several panel methods have claimed success for predictions of the steady aerodynamics for wing-body combinations in the supersonic flow regime (Refs. 2 and 3). In recent years, computational methods for unsteady supersonic flow prediction have been extensively investigated (Ref. 4). However, these approaches are mostly formulated for wing planform calculations. On the other hand, the investigation of unsteady supersonic flow for oscillating bodies in the past has been mostly based on slender body or not-so-slender body theories for rigid-body oscillations in the low-frequency range.

In the slender body limit the Adams and Sears theory (Ref. 5) was extended to unsteady flow by Garrick (Ref. 6). Although Garrick's theory is valid for all frequencies and for flexible bodies, it has the limitations of being independent of the Mach number and it is found too inaccurate for bodies of practical thickness.

In the not-so-slender body limit, Lansing (Ref. 7) used a frequency expansion procedure for treatment of rigid-body oscillations, and Platzer and Sherer (Ref. 8) applied the linearized method of characteristics (LMOC) for rigid bodies in low-frequency oscillations. Tobak and Wehrend (Ref. 9) extended Van Dyke's first- and second-order theories (Ref. 10) to unsteady flow for cones. Bond and Packard's theory (Ref. 11) for flexible bodies appeared in 1961; however, it was found to involve

erroneous boundary conditions, as was pointed out by Hoffman and Platzer (Ref. 12).

It appears that little progress has been made in the development of a viable computational method for wing-body or body-fin combinations, for unsteady supersonic aerodynamic predictions, which is uniformly valid in the complete frequency domain. Hence, the present work consists of the development of a viable method in the full-frequency domain for computations of the unsteady aerodynamics of arbitrary flexible bodies in the supersonic flow regime.

1.2 Outline

For bodies in pitch motion, the proper choice of the coordinate system has been subject to some controversy in the past. In Chapter 2 the formulations in the wind-fixed, the body-fixed (Appendix A), and the pseudo-wind-fixed coordinate systems are presented.

In Chapter 3 the solution procedure for the steady mean flow problem is developed. The linearized equation for the mean flow is solved by using the Karman and Moore procedure (Ref. 13). The nonlinear equation for the mean flow is solved according to Van Dyke's iterative scheme (Ref. 10). Computed mean-flow velocities and pressures for a cone-cylinder, a parabolic-ogive, and a parabolic-ogive-boattail bodies are presented.

In Chapter 4 the solutions of the equations in various coordinate systems as derived in Chapter 2 are obtained. The Harmonic Gradient concept is applied to the dipole strength so that the number of panel elements becomes least affected by the

given Mach number and reduced frequency. It is shown that when the wind-fixed system is applied in a straight-forward manner, the solution obtained is totally contaminated by a spurious leading-edge singularity. In Appendix C, it is shown that such singularity is totally removed in a conical coordinate system. Effects of frequency and mean-flow nonlinearities are investigated in the body-fixed coordinate system. Comparisons of the present results with NASA'S measured data (Refs. 14 and 15) of the aerodynamic damping coefficients for different bodies are shown.

In Chapter 5 the equations for flutter computations are presented. Flutter boundaries for a 7.5° cone are determined by using the linear and nonlinear method. Comparisons of the present results with NASA's measured data (Ref. 16) are presented.

In Chapter 6 the formulation for bodies with asymmetric cross-section is presented in the body-fixed coordinate system. For ease of application a spline panel method is used to determine the pressure and forces acting on the body. Comparisons of the mean flow pressures and static forces for elliptic cones with those computed by USSAERO code (Ref. 2) show clear limitations of the present method when the asymmetry in the body cross-section increases.

In Chapter 7, the development of the Bundle Triplet Method (BTM) is presented. The BTM is a more general method in treatments of asymmetric bodies in that the line doublet formulation of the spline panel method is generated to a

generalized triplet one. The body cross-section is also divided into the so-called "pie sectors" but a line source and a line doublet are superposed in each sectors; thus forming a bundle of triplet lines. A least square procedure is used to account for the interference between sectors. Substantial improvements are found in the results over those obtained using the methods in Chapter 6. Moreover, the BTM is validated through the application cases of cylindrical panel flutter in which the generalized forces obtained are in excellent agreement with exact theories in the higher frequency range and for higher order modes.

In Chapter 8, the formulation for the body-wing combinations is presented. The acceleration potential version of the Harmonic Gradient Method (AHGM) is in combined use for computations of the body-wing aerodynamics. The present formulation not only allows the computed domain to be confined to the surface panels but it also directly yields the unsteady pressure on the wing surface. Therefore, the present method is a very effective one in treatments of unsteady aerodynamics over body-wing configurations.

Finally, conclusions from the present investigation and recommendations for future work are presented in Chapter 9.

In what follows, all variables are nondimensionalized by the true length, and time scales defined by the body length, and the body length divided by the freestream velocity, respectively.

CHAPTER 2

FORMULATION

In this chapter, the formulation for a body of revolution performing bending oscillations is presented.

The fluid flow is assumed to be inviscid and isentropic. Thus, the fluid velocity V can be defined by the scalar potential $\Omega(x',y',z',t')$, i.e.

$$V = \nabla\Omega \tag{2.1}$$

The governing equation for the potential Ω is the full potential equation

$$a^2 \nabla^2 \Omega = \Omega_{t',t'} + \frac{\partial}{\partial t'} (\nabla\Omega)^2 + \frac{1}{2} (\nabla\Omega\cdot\nabla)(\nabla\Omega)^2 \tag{2.2}$$

where "a" is the local speed of sound given by

$$a^2 = \frac{1}{M_\infty^2} - (\gamma-1) \left\{\Omega_{t'} + \frac{1}{2} [(\nabla\Omega)^2 - 1]\right\} \tag{2.3}$$

The time coordinate above, t', is based on a spatial coordinate system, (x',y',z'), that is fixed with respect to the fluid at infinity.

It is known that various linearized small disturbance equations can be derived from Eqs. (2.2) and (2.3) depending on the coordinate system chosen. Their formulations according to the wind-fixed, the body-fixed and the pseudo-wind-fixed coordinate systems are discussed in order.

2.1 Wind-Fixed Coordinate System

If a cylindrical coordinate system with its x'-axis parallel to the freestream velocity is adopted (see Fig. 3) then the full potential can be written as

$$\Omega\,(x',r',\Theta',t') = x' + \Phi\,(x',r',\Theta',t') \qquad (2.4)$$

where $\Phi(x',r',\Theta',t')$ is the perturbation potential.

Substituting Eq. (2.4) into Eqs. (2.2) and (2.3) and retaining only linear terms in Φ yields the following linear equation

$$(1 - M_\infty^2)\Phi_{x'x'} + \Phi_{r'r'} + \frac{1}{r'}\Phi_{r'} - 2M_\infty^2\Phi_{x't'} - M_\infty^2\Phi_{t't'} = 0 \qquad (2.5)$$

For a body of revolution in unsteady motion with small amplitude of oscillation the perturbation potential can be split into two parts; the mean flow, zero-angle-of-attack, potential, $\phi_0(x',r')$, and the unsteady flow potential, $\phi_1(x',r')\cos\Theta'$

$$\Phi(x',r',\Theta',t') = \phi_0(x',r') + \delta(t')\phi_1(x',r')\cos\Theta' \qquad (2.6)$$

where $\delta(t')$ is the instantaneous amplitude of oscillation. For simple harmonic oscillations $\delta(t')=\delta_0 e^{ikt'}$, where k is the reduced frequency. Substituting these relations into Eq. (2.5) and collecting terms of order one and δ_0, one obtains

$$(1 - M_\infty^2)\,\phi_{0x'x'} + \phi_{0r'r'} + \frac{1}{r'}\phi_{0r'} = 0 \qquad (2.7)$$

$$(1 - M_\infty^2)\,\phi_{1x'x'} + \phi_{1r'r'} + \frac{1}{r'}\,\phi_{1r'}$$

$$- \frac{1}{r'^2}\,\phi_1 - 2ikM_\infty^2\,\phi_{1x'} + M_\infty^2 k^2 \phi_1 = 0 \qquad (2.8)$$

These are the governing equations in the wind-fixed coordinate system for ϕ_0 and ϕ_1.

2.1.1 Boundary Conditions

Physical considerations suggest that all perturbations should vanish upstream of the Mach wave emanating from the body apex,

$$\left.\begin{aligned} \phi_0(x',r') = \phi_{0x'}(x',r') = \phi_{0r'}(x',r') = 0 \\ \phi_1(x',r') = \phi_{1x'}(x',r') = \phi_{1r'}(x',r') = 0 \end{aligned}\right\} \text{at } x'-\beta r' \le 0 \qquad (2.9)$$

and that at any instant the flow must be tangent to the body surface. In the wind-fixed coordinate system the latter condition can be expressed as

$$\frac{\partial S}{\partial t} + \nabla\Omega\cdot\nabla S = 0 \qquad \text{at } S = 0 \qquad (2.10)$$

where $S(x',r',\Theta',t')=0$ describes the body surface. For a body of revolution performing small amplitude bending oscillations, the equation of the body surface can be simplified (Ref. 17) to

$$S(x',r',\Theta',t') = r'-R(x') + \delta(t')g(x')\cos\Theta' + O(\delta_0^2) = 0 \qquad (2.11)$$

where $g(x')$ is the normalized natural mode shape.

Now, substituting Eqs. (2.11), (2.4) and (2.6) into (2.10) yields

$$\phi_{0r'} - R'(1+\phi_{0x'}) + \delta(t')\cos\Theta'$$
$$[g'(1+\phi_{0x'}) - R'\phi_{1x'} + \phi_{1r'} + ikg] + O(\delta_0^2) = 0 \qquad (2.12)$$
$$\text{at } r' = R(x') - \delta(t')g(x')\cos\Theta'$$

It is now necessary to remove the implicit dependence on $\delta(t')$ in the potential functions by expressing the boundary condition at the mean position (Ref. 17) $r'=R(x')$. This is accomplished by using a Taylor-series expansion about $r'=R(x')$. Performing this expansion in Eq. (2.12) and collecting terms of order one and δ_0, yields

$$\phi_{0r'} - R'\phi_{0x'} = R' \qquad \text{at } r' = R(x') \quad (2.13)$$

$$\phi_{1r'} - R'\phi_{1x'} = -g'(x')(1+\phi_{0x'}) + g(x').$$
$$(\phi_{0r'r'} - R'\phi_{0x'r'}) - ikg(x')$$
$$\text{at } r' = R(x') \quad (2.14)$$

2.1.2 Pressure Coefficient

Based on the time-dependent Bernoulli equation, the exact isentropic pressure coefficient is expanded to yield the mean flow and unsteady flow pressure coefficients,

$$C_p = C_p^0 + C_p^1 \delta_0 e^{ikt'}\cos\Theta' \qquad (2.15)$$

and after Taylor-series expansion about the mean position $r'=R(x')$, C_p^0 and C_p^1 can be expressed as

$$C_p^0 = \frac{2}{\gamma M_\infty^2}\left[S_0^{\gamma}-1\right] \qquad \text{at } r'=R'(x) \quad (2.16)$$

$$C_p^1 = -2S_0\left\{(1+\phi_{0x'})\,\phi_{1x'} + \phi_{0r'}\phi_{1r'} + ik\phi_1 - g(x')\right.$$
$$\left.[\phi_{0x'r'}(1+\phi_{0x'}) + \phi_{0r'r'}\phi_{0r'}]\right\} \quad \text{at } r=R(x) \quad (2.17)$$

and

$$S_0 = \left[1 - \frac{\gamma-1}{2} M_\infty^2(2\phi_{0x'} + \phi_{0x}^2{}_{'} + \phi_{0r'}^2)\right]^{1/\gamma-1} \qquad (2.18)$$

As shown in Appendix C, in the slender body approximation, ϕ_{0r} is given by

$$\phi_{0r'} = \frac{RR'}{r'} .$$

and its derivatives with respect to x' and r' are respectively

$$\phi_{0r'x'} = \frac{R'^2 + RR''}{r'} , \text{ and } \phi_{0r'r'} = -\frac{RR'}{r'^2} .$$

At the body apex both terms behave like

$$\frac{R'(0)}{R(0)} ,$$

thus, if R'(0) does not vanish, the second order derivatives $\phi_{0r'x'}$ and $\phi_{0r'r'}$ are singular at the body apex since R(0)=0. Hence, the second order derivative terms in Eqs. (2.14) and (2.17) associated with g(x') will result in an apex singularity

if g(0) does not vanish. The cause of this apex singularity was discussed by Platzer and Liu (Ref. 17), where they pointed out that it was due to the assumption that $\delta_0^2 g^2(x')/R^2(x') \ll 1$ was not uniformly valid at the apex for a nonvanishing g(0). Apparently, this singularity is inherent to the thickness part of the solution, since in the slender body limit, Hoffman and Platzer (Ref. 12) have shown that the unsteady pressure remains regular. It is shown in Appendix C that this finding also applies to not-so-slender bodies. Hence, to circumvent this singularity in the formulation, the obvious choice is the body-fixed coordinate system.

2.2 Body-Fixed Coordinate System

As shown in Fig. 3 the body-fixed coordinate system requires that the x-axis remain, at all times, the axis of the body, whereby each right cross section is circular and contains the r-axis.

Let h(x,t') be the instantaneous normal displacement of the body, i.e.

$$h(x,t') = \delta_0 e^{ikt'} g(x) \qquad (2.19)$$

The full potential in a cartesian coordinate system (x,y,z) (see Appendix A) can be written as:

$$\Omega(x,y,z,t) = x + h_x(x,t)z + \Phi(x,y,z,t) \qquad (2.20)$$

The linearized equation for Φ as derived in Appendix A is

$$\Phi_{xx} - 2h_{xx}z\Phi_{xx} - h_{xxx}z\Phi_x + \Phi_{yy} + h_{xx}\Phi_z$$

$$= M_\infty^2\left[\Phi_{tt} - h_{xtt}z\Phi_x - h_{xt}z\Phi_{xt} + h_{tt}\Phi_z + h_t\,\Phi_{zt}\right.$$

$$+ 2\Phi_{xt} - 2h_{xxt}z\Phi_x - 2h_{xx}z\Phi_{xt} + 2h_{xt}\Phi_z$$

$$+ 2h_x\Phi_{zt} - 2h_{xt}z\Phi_{xx} + 2h_t\Phi_{xz} + \Phi_{xx}(1 - 2h_{xx}z)$$

$$\left. - h_{xxx}z\Phi_x + h_{xx}\Phi_z + 2\Phi_{xz}h_x\right] \qquad (2.21)$$

Clearly, it can be seen that the linearized equation in the body-fixed coordinate system is different from the one obtained in the wind-fixed system.

As derived in Appendix A, Eqs. (A.18) and (A.19), the governing equations for ϕ_0 and ϕ_1 for a body of revolution in the cylindrical coordinates (x,r,Θ) are

$$(1 - M_\infty^2)\,\phi_{0xx} + \phi_{0rr} + \frac{1}{r}\,\phi_{0r} = 0 \qquad (2.22)$$

$$(1 - M_\infty^2)\,\phi_{1xx} + \phi_{1rr} + \frac{1}{r}\,\phi_{1r}$$

$$- \frac{1}{r^2}\,\phi_1 - 2ikM_\infty^2\phi_{1x} + M_\infty^2k^2\phi_1 = G_1(g,\phi_0) \qquad (2.23)$$

where G_1 represents the mean flow and the flexible mode interaction and is given by

$$G_1(g,\phi_0) = M_\infty^2\left[2\frac{\partial}{\partial x}(\phi_{0r} - r\phi_{0x}\frac{\partial}{\partial x})(g' + ikg)\right.$$

$$\left. - (\phi_{0r} - r\phi_{0x}\frac{\partial}{\partial x})(gk^2 + g'')\right] + r\frac{\partial}{\partial x}(\phi_{0x}g'')$$

$$+ g''(\phi_{0xx}r - \phi_{0r}) \qquad (2.24)$$

Eq. (2.23) contains Van Dyke's (Ref. 10) steady angle of attack equation and Hoffman and Platzer's (Ref. 18) low-frequency equation as special cases. It should be pointed out that Eq. (2.23) for steady angle of attack differs from McCanless' (Ref. 19) equation which is clearly in error since his formulation starts from a linearized equation rather than the full potential equation.

2.2.1 Boundary Conditions

The boundary conditions at the apex are the same as those given by Eq. (2.9), while the tangential boundary condition in the body-fixed system states that the relative normal velocity of a fluid particle to the body surface is zero at any instant, i.e.

$$(\nabla\Omega - V_B)\cdot n = 0 \qquad \text{at } S = 0 \qquad (2.25)$$

where V_B is the velocity of the body surface, S is the body surface which for a body of revolution in a cylindrical coordinate system can be expressed as

$$S = r - R(x) = 0 \qquad (2.26)$$

and n is the outward normal to the body surface. For a body performing bending oscillations, V_B can be shown to be

$$\vec{V}_B = \dot{\delta}(t)[g' R\cos\Theta\, \vec{e}_x - g(\cos\Theta\, \vec{e}_r - \sin\Theta\, \vec{e}_\Theta)] \qquad (2.27)$$

The total velocity in this curvilinear coordinate system is obtained (see Appendix A) as

$$\nabla\Omega = [1 + \phi_{0x} - \delta(t)\, g''\, \phi_{0x} R\cos\Theta + \delta(t)\phi_{1x}\cos\Theta]\vec{e}_x$$

$$+ [\phi_{0r} + \delta(t)\phi_{1r}\cos\Theta + g'\, \delta(t)\, \cos\Theta]\vec{e}_r$$

$$- \delta(t)[g'\, \sin\Theta + \frac{1}{R}\, \phi_1\, \sin\Theta]\vec{e}_\Theta \qquad (2.28)$$

Now substituting Eqs. (2.28) and (2.27) into (2.25) yields

$$[1 - \delta(t)g''\, R\, \cos\Theta + \phi_{0x} + \delta(t)\phi_{1x}\cos\Theta$$

$$- \dot{\delta}(t)g'\, R\, \cos\Theta](-R') + \phi_{0r}$$

$$+ (\delta(t)g' + \delta(t)\phi_{1r} + \dot{\delta}(t)g)\, \cos\Theta = 0 \qquad \text{at } r=R(x) \qquad (2.29)$$

where for simple harmonic oscillations $\dot{\delta}(t)=ik\delta(t)$ and $\delta=\delta_0 e^{ikt}$. Substituting this relation into Eq. (2.29) and collecting like terms of order one and δ_0, yield

$$\phi_{0r} - R'\phi_{0x} = R' \qquad (2.30)$$

$$\phi_{1r} - R'\phi_{1x} = -g' - ik(g + g'RR') - g''RR'\phi_{0x}$$

$$\text{at } r=R(x) \qquad (2.31)$$

Eq. (2.31) reduces, to the Lighthill's (Ref. 20) boundary conditions when the second-order terms are neglected.

2.2.2 Pressure Coefficient

The exact isentropic pressure coefficient can be expressed as

$$C_p = \frac{2}{\gamma M_\infty^2}\left\{\left[1 - \frac{\gamma-1}{2}M_\infty^2((\nabla\Omega)^2 + 2\Omega_{t'}-1)\right]^{\gamma/\gamma-1} - 1\right\} \quad (2.32)$$

where t' is the nondimensional time in the wind-fixed system. The partial derivative with respect to t' as measured by an observer moving with the harmonically oscillating body-fixed system is given by

$$\frac{\partial\Omega}{\partial t'} = \frac{\partial\Omega}{\partial t} - g'\dot{\delta}(t)r\cos\theta\frac{\partial\Omega}{\partial x} + g\dot{\delta}(t)(\cos\theta\frac{\partial\Omega}{\partial r} - \frac{1}{r}\sin\theta\frac{\partial\Omega}{\partial\theta}) \quad (2.33)$$

Note that Eqs. (2.22), (2.31) and (2.33) contain Revell's equations (Ref. 21) for rigid-body oscillations as a special case.

Substituting Eqs. (2.33) and (2.28) into (2.32) and, after binomial expansion, collecting terms of order δ_0 the pressure coefficient for unsteady flow C_p^1 can be written as

$$C_p^1 = -2S_0\{\phi_{1x}(1 + \phi_{0x}) - (1 + \phi_{0x})g''R\phi_{0x} + \phi_{0r}(\phi_{1r} + g') + ik\,(g\phi_{0r} + \phi_1 - g'R\phi_{0x})\} \quad (2.34)$$

at r=R(x)

were S_0 is given by Eq. (2.18) and the pressure coefficient for the mean flow C_p^0 by Eq. (2.16).

Eqs. (2.23), (2.31) and (2.34) together with the Mach wave conditions at the apex, Eq. (2.9), constitute the formal formulation according to the body-fixed coordinate system. However, to solve Eq. (2.23) is rather tedious. For this reason, a justification for simplified form of this equation is sought. Van Dyke (Ref. 10) has shown that his "first-order" steady cross flow equation,

$$(1 - M_\infty^2)\, \phi_{1xx} + \phi_{1rr} + \frac{1}{r}\, \phi_{1r} - \frac{1}{r^2}\, \phi_1 = 0$$

is superior in yielding better results to the linearized equation, which contains one extra term, in the higher Mach number range. For bodies in low-frequency oscillations, Platzer et al. (Ref. 8) and Tobak et al. (Ref. 9) adopted the first-order equation formulation to obtain stability derivatives. Their results were found in good agreement with computed results using Euler's equations. Thus, extending Van Dyke's first-order equation further in the general frequency domain amounts to neglecting the interaction terms $G_1(g, \phi_0)$ in Eq. (2.23). In this way, the linearized wave equation is employed for the present formulation. Admittedly, this level of approximation is injustifiable mathematically. Nevertheless, the interaction effect due to the term G_1 can be recovered formally by a Green function approach as proposed in Chapter 4.

2.3 Pseudo-Wind-Fixed Coordinate System

The present coordinate system is a hybrid one. The x-axis chosen here is not the body axis, but remains rigid in motion,

thus avoiding the complexity of using the curvilinear coordinates. Meanwhile, the front-end of the bending mode g(x) when expressed in this coordinate is required to attach to the origin of the x-axis at all times, as indicated in Fig. 3. In this way, the apex singularity can be totally removed. Admittedly, such a formulation for singularity removal is not totally justifiable but intended to serve as a regular approximation.

Hence, the linearized equation can be obtained in the same form as Eq. (2.23) by letting $g(x)=x-x_0$ in Eq. (2.24), and G_1 is replaced by $G_2(g,\phi_0)$ as follows

$$G_2(g,\phi_0) = M_\infty^2 \{2\phi_{0xr} + k^2[r\,\phi_{0x} - (x-x_0)\,\phi_{0r} + 2ik \phi_{0r} - r\phi_{0xx} + (x-x_0)\phi_{0rx}\} \qquad (2.35)$$

where x_0 is a point chosen on the x-axis such that $p(0)=0$. Since this equation is a degenerate form of the body-fixed equation, the justification for neglecting G_2 terms also remains valid here. The mode shape g(x) expressed in this system now becomes p(x), where

$$p(x) = g(x) - (x_0-x) \qquad (2.36)$$

The potential is split into two components,

$$\phi_1 (x,r) = \psi(x,r) + \lambda(x,r) \qquad (2.37)$$

where ψ and λ represent the rigid part (x-axis motion) and the flexible part (p(x) motion) of the potential, respectively. Thus, the boundary conditions, after Taylor-expansion transferal to the mean surface, become, at r=R(x)

$$\psi_r - R'\psi_x = -1 - ik(x - x_0 + RR') \qquad \text{at } r=R(x) \quad (2.38)$$

$$\lambda_r - R'\lambda_x = -p'(x)(1 + \phi_{0x} - ikp(x) + p(x)\phi_{0rr} - p(x)R'\phi_{0xr} \quad \text{at } r=R(x) \quad (2.39)$$

Notice that Eq. (2.39) is essentially the same as Eq. (2.14) of the wind-fixed system with g(x) replaced by p(x). The pressure coefficients C_p^{1r} and C_p^{1f}, corresponding respectively to ψ and λ, read

$$C_p^{1r} = -2S_0 \cdot \{[(1 + \phi_{0x})\psi_x + \phi_{0r}(\psi_r + 1) + ik(\psi - R\phi_{0x} + (x - x_0)\phi_{0r})]\} \qquad \text{at } r=R(x) \quad (2.40)$$

and

$$C_p^{1f} = -2S_0 \cdot \{(1 + \phi_{0x})\lambda_x + \phi_{0r}\lambda_r + ik\lambda - p(x)[\phi_{0xr} + \phi_{0x}\phi_{0xr} + \phi_{0r}\phi_{0rr}]\} \qquad \text{at } r=R(x) \quad (2.41)$$

where

$$C_p^1 = C_p^{1r} + C_p^{1f} \quad (2.42)$$

In the present system p(0)=0. Therefore, this condition guarantees, all second-order coupling terms in the bracket of Eq. (2.41) when multiplied by p(x) become necessarily finite at the apex.

It should be noted that although the apex singularity is removed in the pseudo-wing-fixed system Eq. (2.41) is still not uniformly valid, because these second-order derivative terms will bear local singularities at other body slope discontinuities such as the cone-cylinder junctions. In the case of the body-fixed system, however, such singularities do not appear, since the unsteady pressures only involve first-order derivative terms.

2.4 Generalized Forces and Stability Derivatives

One of the main purposes of the unsteady aerodynamic computations is to determine the generalized forces (Q_{IJ}), which appear in the Lagrange's equations of motion for the structural system. There, the generalized force Q_{IJ} represents the work done by the aerodynamic force F^J per unit displacement g^I with all other generalized coordinates fixed.

In the present case, once the unsteady pressure coefficients as provided by Eqs. (2.17), (2.34) or (2.42) are determined, the generalized forces can be computed according to

$$Q_{IJ} = \frac{-1}{S_{ref}} \int_0^{2\pi} \int_0^1 C_p^{I(J)} R[g^{(I)} + RR'g'^{(I)}]\cos^2\theta d\theta dx \tag{2.43}$$

where $g^{(I)}$ is the Ith structural mode; $C_p^{I(J)}$ is the pressure coefficient due to the Jth mode of motion and S_{ref} is the

reference area of the body. Here, S_{ref} is defined as the based area for the open-end bodies and the maximum cross-section area for the closed-end bodies.

As will be shown in Chapter 5, the generalized forces resulting from the unsteady flow caused by the changing deformations of the body surface occur in the equations of flutter. Thus the determination of reliable flutter boundaries depends on the accurate evaluation of the generalized forces.

Once the generalized forces have been determined the stability derivatives for rigid low-frequency body motion can be determined in the following form

$$\left.\begin{aligned} C_{N\dot{\alpha}} &= -RE(Q_{12}) \\ C_{M\dot{\alpha}} &= -RE(Q_{22}) \\ C_{N\dot{\alpha}} + C_{Nq} &= -IM(Q_{12})/k \\ C_{M\dot{\alpha}} + C_{Mq} &= -IM(Q_{22})/k \\ C_{L\dot{\alpha}} &= -RE(Q_{11})/k^2 \\ C_{M\dot{\alpha}} &= -RE(Q_{21})/k^2 \end{aligned}\right\} \qquad (2.44)$$

where "1" is the plunging mode and "2" the pitching mode, and RE means the real part and IM the imaginary part.

CHAPTER 3

STEADY MEAN FLOW

The purpose of solving the steady mean flow problem is two-fold. First, it is necessary to obtain the mean flow velocities on the body in order to proceed with the unsteady flow computations because the unsteady flow potential and the unsteady pressure coefficient depend on the mean flow solution. Second, it is important to establish a robust unsteady computational procedure, which can be first established by the steady mean flow studies as a primary step, as the steady mean-flow is provided with more readily available data for result verifications.

It has been noted that first-order theory predicts the cross flow more accurately than the axial flow because smaller disturbances, in the convective direction, are involved. This suggests that it is more important to refine the axial flow than the cross flow. In fact this type of hybrid theory has been suggested previously by Van Dyke (Ref. 10) involving a linear-equation model for the cross flow and a nonlinear-equation model for the mean flow.

For the cross-flow model the use of this hybrid theory can only be justified by previous numerical studies. In the past Van Dyke (Ref. 10) obtained accurate results for bodies at steady angle of attack, and Tobak and Wehrend (Ref. 9) obtained results for the static and dynamic stability derivatives for cones, which are in good agreement with those obtained based on the Euler's solution. Thus, in this chapter, together with the solution of

the linear equation for the mean flow, Eq. (2.7), a nonlinear equation for the mean flow is derived. Its solution, by employing an iterative procedure first suggested by Van Dyke, is presented. In the latter development and for legends in Figures presented, this unsteady hybrid model is termed "nonlinear".

3.1 Solution of the Linear Equation

The governing equation for the mean flow as derived in Chapter 2, Eq. (2.7) can be written as:

$$(1 - M_\infty^2)\phi_{0xx} + \phi_{0rr} + \frac{1}{r}\phi_{0r} = 0 \qquad (3.1)$$

Along the apex Mach wave and on the body surface the boundary conditions are:

$$\phi_0 = \phi_{0x} = \phi_{0r} = 0 \qquad \text{at } x - \beta r \leq 0 \qquad (3.2)$$

$$\phi_{0r} - R'\,\phi_{0x} = R' \qquad \text{at } r = R(x) \qquad (3.3)$$

Since Eq. (3.1) is linear, it admits superposition of solutions. Therefore, for a body of revolution, whose upstream pointed end is at x=0, the solution to Eq. (3.1) can be sought as a superposition of supersonic sources along the x-axis. The potential at (x,r) can be expressed as (Ref. 13)

$$\phi_0(x,r) = -\int_0^{x-\beta r} \frac{f(\xi)}{\sqrt{(x-\xi)^2-\beta^2 r^2}}\, d\xi \qquad (3.4)$$

where ξ denotes the distributed source location along the x-axis and $f(\xi)$ is the source strength at ξ.

The velocity components, after differentiation of Eq. (3.4), are given by

$$\phi_{0x}(x,r) = -\int_0^{x-\beta r} \frac{f'(\xi)\,d\xi}{\sqrt{(x-\xi)^2-\beta^2 r^2}}$$

$$\phi_{0r}(x,r) = \frac{1}{r}\int_0^{x-\beta r} \frac{(x-\xi)f'(\xi)\,d\xi}{\sqrt{(x-\xi)^2-\beta^2 r^2}} \qquad (3.5)$$

Eqs. (3.4) and (3.5) satisfy the conditions given by Eq. (3.2) if $f(0)=0$ and the source strength function f will be determined from the tangency condition, Eq. (3.3). This leads to a Volterra integral equation, which can, in general, only be solved numerically. The procedure introduced by von Karman and Moore (Ref. 13) proceeds by replacing the body by one consisting of a head cone and a sequence of truncated cones. The procedure is clearly described in the standard texts such as Sauer (Ref. 22) and Ferri (Ref. 23). Its generalization to the unsteady problems is described in the next chapter.

3.2 The Nonlinear Equation and Its Solution

A nonlinear equation for the mean flow perturbation potential $\phi_0(x,r)$ can be obtained by starting with the full potential as $\Omega(x,r,\Theta)=x+\phi_0(x,r)$. Substituting this expression into Eqs. (2.2) and (2.3) yields

$$(1-M_\infty^2)\phi_{0xx} + \phi_{0rr} + \frac{1}{r}\phi_{0r} = M_\infty^2\left\{\frac{\gamma-1}{2}(\phi_{0xx} + \phi_{0rr} + \frac{1}{r}\phi_{0r})\right.$$

$$(2\phi_{0x} + \phi_{0x}^2 + \phi_{0r}^2)$$

$$+ 2\phi_{0r}\phi_{0xr}(1 + \phi_{0x}) \qquad (3.6)$$

$$\left. + \phi_{0xx}(2\phi_{0x} + \phi_{0x}^2) + \phi_{0r}^2\phi_{0rr}\right\}$$

According to Van Dyke (Ref. 10), Eq. (3.6) can be solved by an iterative procedure. Letting $L(\cdot)$ be the left-hand side operator and $R(\cdot)$ the right-hand side operator, Eq. (3.6) can be simply expressed as

$$L(\phi_0) = R(\bar{\phi}_0) \qquad (3.7)$$

where the potential $\bar{\phi}_0$ is the first-order iteration obtained by solving the linearized equation $L(\bar{\phi}_0)=0$. Making use of this fact, the right-hand side $R(\bar{\phi}_0)$ can be expressed as

$$R(\bar{\phi}_0) = M_\infty^2\{2\bar{\phi}_{0xr}\bar{\phi}_{0r} + [2 + (\gamma - 1)M_\infty^2]\bar{\phi}_{0xx}\bar{\phi}_{0x} + \bar{\phi}_{0rr}\bar{\phi}_{0r}^2 \qquad (3.8)$$

$$+ \frac{\gamma-1}{2}M_\infty^2\,\bar{\phi}_{0xx}\bar{\phi}_{0r}^2 + 2\bar{\phi}_{0xr}\bar{\phi}_{0x}\bar{\phi}_{0r} + (1 + \frac{\gamma-1}{2}M_\infty^2)\bar{\phi}_{0xx}\bar{\phi}_{0x}^2\}$$

For the second order iteration all the triple products in Eq. (3.8) can be neglected except the term $\bar{\phi}_{0rr}\bar{\phi}_{0r}^2$, which, as can be shown from the slender-body theory, is of the same order as the other two quadratic terms. Thus, the equation for the second-order iteration can be written as

$$L(\phi_0) = M_\infty^2 \left[2\bar{\phi}_{0x}\bar{\phi}_{0r} + [2 + (\gamma-1)M_\infty^2]\,\bar{\phi}_{0xx}\bar{\phi}_{0x} + \bar{\phi}_{0rr}\bar{\phi}_{0r}^2\right] \tag{3.9}$$

To solve Eq. (3.9) Van Dyke's particular solution ψ_0 is employed.

$$\psi_0 = M_\infty^2\left[\bar{\phi}_{0x}(\bar{\phi}_0 + Nr\,\bar{\phi}_{0r}) - \frac{r}{4}\,\bar{\phi}_{0r}^3\right] \tag{3.10}$$

where $N=(\gamma+1)M_\infty^2/[2(M_\infty^2-1)]$. It should be noted that ψ_0, when substituted on the left-hand side of Eq. (3.9), besides accounting for all the terms on the right-hand side, also gives some triple products involving x derivatives of $\bar{\phi}_0$. These triple product terms are of order equal to or higher than those terms already neglected in Eq. (3.8). Hence, for the second order iteration, ψ_0 can be considered as an exact particular solution. Then, ϕ_0 can be expressed as $\phi_0=X_0+\psi_0$, where X_0 satisfies $L(X_0)=0$.

Both potential ϕ_0 and $\bar{\phi}_0$ must satisfy the Mach wave condition Eq. (3.2), this dictates that both ψ_0 and X_0 should also satisfy the same condition independently. The problem of X_0 is just the first order problem, with the tangency condition Eq. (3.3) replaced by

$$X_{0r}(x,r) - R'X_{0x}(x,r) = R'(1+\psi_{0x}(x,r)) \qquad (3.11)$$
$$- \psi_{0r}(x,r) \qquad \text{at } r = R(x)$$

The complete second order perturbation velocities are found as the sums of the contributions from ψ_0 and X_0. Then, the pressure coefficient can be calculated according to Eq. (2.16).

3.3 Results and Discussions

To demonstrate the present method and to validate its procedures several computed cases are presented: the mean flow total velocity for a cone-cylinder, mean flow pressures for a parabolic-ogive, and an ogive-cylinder-boattail bodies are shown as examples.

Figure 4 demonstrates that the present linear method yields correct values for the velocity. It is seen that the present result is in good agreement with the USSAERO result as well as those obtained by other theories (see Ref. 10) for a cone-cylinder body. The deviation of USSAERO result on the aft-cylinder is probably caused by an erroneous wave influence generated by the lower junction of the cone-cylinder. In Figs. 5 and 6 the linear and the nonlinear results are compared with those computed by USSAERO code, and by the exact method of characteristics (Ref. 24), for a 26% thick ogive-cylinder body at Mach numbers of 2.0 and 3.0, respectively. The nonlinear results compare very well with those computed by the exact method of characteristics. It is seen that the nonlinear effect due to the thickness is substantial from the apex to mid-body.

Next, the hybrid theory (nonlinear iterative scheme for the mean flow and linear for the cross flow) is applied to a 16% thick ogive-cylinder-boattail body at Mach number of 3.0 and placed at moderate angles of attack (α_0=3.2 and 6.3). Again, very good correlations are found with the computed results of the Parabolized Navier-Stokes (PNS) code and the Euler code (Ref. 25) for both cases in Figs. 7a and 7b. Considerable deviations between the linear and the nonlinear results are again observed particularly on the windward side of the ogive part of the body.

It can be concluded that, as long as the flow remains attached, the present nonlinear method should yield results in favorable agreement with those obtained by computational methods in the supersonic Mach number range. This agreement also implies that for the given range of Mach number, body thickness and angle-of-attack, effects of rotationality as introduced by supersonic shock waves are nearly inconsequential.

CHAPTER 4

UNSTEADY FLOW COMPUTATIONS

In this chapter, the method of solution for a uniform flow over a body performing bending oscillations is presented. The formulations in the wind-fixed, body-fixed and pseudo-wind-fixed coordinate systems, as described in Chapter 2, are used. To compute the oscillatory flow in the cross plane, a line doublet distribution scheme (see Fig. 8) is adopted. The strength of the doublet along the axis is modeled according to the Harmonic Gradient model for treating wing planforms (Ref. 4) This model is capable of rendering the unsteady potential solution and its convective gradient uniformly valid throughout the complete frequency domain.

To verify the present method, numerical examples for various body shapes are presented, in terms of unsteady pressures, stability derivatives, generalized forces, and aerodynamic damping, and compared with various theories and measured data.

4.1 The Integral Solution

The general integral solution to the unsteady wave equation, e.g. Eq. (2.8) or Eq. (2.23), can be obtained by applying the Green function method.

$$\phi_1(x,r) = \frac{-1}{2\pi} \int_0^{x-\beta r} F(\xi) \frac{\partial}{\partial r} K(x-\xi, \beta r) d\xi + \phi_g \qquad (4.1)$$

where

$$\phi_g = \frac{1}{2\pi} \int\int_A G_n(\phi_0(\xi,\eta),g)\ K(x-\xi,\ \beta r)\,d\eta\,d\xi$$

The function $G_n(\phi_0, g)$ is the inhomogeneous term of the unsteady wave equation, G_1 in Eq. (2.23) or G_2 in Eq. (2.35) and the area A is defined in the domain downstream of the Mach wave, emanating from the apex, excluding the body, i.e.

$$R(x) \le \eta \le \xi/\beta\ , \qquad \text{for } 0 \le \xi \le 1$$

$$0 \le \eta \le \xi/\beta\ , \qquad \text{for } 1 \le \xi \le \infty$$

The first term of Eq. (4.1) represents the linear unsteady solution as modeled by the distribution of doublets along the x-axis, and the second term, ϕ_g, the mean flow-mode shape interaction.

In the present analysis, we shall drop the term ϕ_g in Eq. (4.1) for simplicity. But in principle ϕ_g can be included in the analysis since ϕ_0 is known from the mean flow computation and g(x) is given. The kernel function K is an elementary solution of Eq. (2.6) (see Garrick, Ref. 26)

$$K(x-\xi,\ \beta r) = e^{-i\mu(x-\xi)}\ \frac{\cos\lambda R}{R} \qquad (4.2)$$

where R is now the hyperbolic distance and is defined as

$R = \sqrt{(\bar{x}-\bar{\xi})^2 - \beta^2 \bar{r}^2}$, $\mu = kM_\infty^2/\beta^2$ and $\lambda = kM_\infty/\beta^2$

and $F(\xi)$ is the dipole strength to be sought.

Now, integrating Eq. (4.1) by parts, and making use of the Mach wave condition at $x=\beta r$, yields

$$\phi_1(x,r) = \frac{-1}{2\pi}\int_{x}^{\beta r} \frac{\partial}{\partial x_0}\left[F(x-x_0)e^{-i\mu x_0}\right]\frac{\partial}{\partial r}S(x_0,\beta r)\,dx_0 \qquad (4.3)$$

where

$$\frac{\partial}{\partial r}S(x_0,\beta r) = \frac{\partial}{\partial r}\int_{\beta r}^{x_0}\frac{\cos\lambda R_\tau}{R_\tau}\,d\tau$$

$$x_0 = x-\xi \text{ and } R_\tau = \sqrt{\tau^2-\beta^2r^2} \qquad (4.4)$$

Notice that from this point onward "x_0" is used to represent the relative dipole coordinate.

4.2 Harmonic Gradient Model

The solution of Eq. (4.3) is based on a line-doublet panel method similar to Karman and Moore's (Ref. 13) procedure for the source solution formulation to the mean flow. Thus, a set of N points with coordinates $(x_j,r_j,0)$ $j=1,\ldots N$ are distributed on the body surface, such that $x_{j+1}>x_j$. These points are called the control points. To determine the induced potential at each control point the intersection of the inverse Mach cone, from the control point $(x_j,r_j,0)$, with the body axis is first determined, (see Fig. 8). The set of points so obtained are given by $\xi_{j+1}=x_j-\beta r_j$ $j=1,\ldots N$, with ξ_1 being the body apex. The segment between each two points $(\xi_j,\ \xi_{j+1})$ is called a panel. Each panel

is assumed to have different dipole strength $F_j(\xi)$. The potential ϕ_1 at (x_j, r_j) can then be expressed as

$$\phi_1(x_j, r_j) = \frac{-1}{2\pi} \sum_{i=1}^{L} \int_{x_j - \xi_i}^{x_j - \xi_{i+1}} \frac{\partial}{\partial x_0}\left[F_i(x_j - x_0)e^{-i\mu x_0}\right] \frac{\partial}{\partial r_j} S(x_0, \beta r_j)\, dx_0 \quad . \tag{4.5}$$

In order to achieve computational accuracy and effectiveness for handling solutions in the high-frequency range, it is important to render the doublet solution and its convective gradient uniformly valid throughout the complete frequency domain. This is to say that the characteristics of the doublet solution should be spatially harmonic. Therefore, the panel size from ξ_i to ξ_{i+1} is regulated and maintained compatible to the wave number generated along the body in oscillation (see Fig. 9). This is the Harmonic Gradient concept introduced by Chen and Liu[4] for unsteady supersonic computations. Following this concept, one can model the integrand of Eq. (4.5) in a similar manner, i.e.,

$$\frac{\partial}{\partial x_0}\left[F_i(x_j - x_0)e^{-i\mu x_0}\right] = \left[a_i(x_j - x_0) + b_i\right]e^{-i\mu x_0} \tag{4.6}$$

where a_i and b_i on the right-hand side are complex constants representing a linear-harmonic doublet gradient.

4.3 Evaluation of Velocities

With the Harmonic Gradient (H-G) model of Eq. (4.6), Eq. (4.5) can be differentiated to obtain the discretized velocities ϕ_{1x} and ϕ_{1r}, i.e.

$$\phi_{1x}(x_j, r_j) = \frac{-1}{2\pi} \sum_{i=1}^{j} a_i \int_{x_j - \xi_i}^{x_j - \xi_{i+1}} e^{-i\mu x_0} \frac{\partial}{\partial r_j} S(x_0, \beta r_j) dx_0 \quad (4.7)$$

$$\phi_{1r}(x_j, r_j) = \frac{-1}{2\pi} \sum_{i=1}^{j} \int_{x_j - \xi_i}^{x_j - \xi_{i+1}} [a_i(x_j - x_0) + b_i] e^{-i\mu x_0}$$

$$\frac{\partial^2}{\partial r_j^2} S(x_0, \beta r_j) dx_0 \quad (4.8)$$

For detailed evaluation of these integrals one is referred to Appendix B. There it is shown that Eqs. (4.5), (4.7) and (4.8) can be integrated numerically by employing Lashka's (Ref. 27) exponential substitution scheme.

4.4 Method of Solution

After Eqs (4.5), (4.7) and (4.8) have been integrated, the potential and the velocities at (x_j, r_j) can be expressed as functions of the a_i's and b_i's. However, the b_i's can be determined as functions of the a_i's by imposing the condition that the potential must be continuous between each two adjacent

panels. With this condition the following recurrence formula can be established, i.e.

$$b_n = \frac{-a_1}{i\mu}(1-e^{i\mu\xi_1}) - \sum_{j=2}^{n-1} \frac{a_j}{i\mu}(e^{i\mu\xi_{j-1}}-e^{i\mu\xi_j}) \qquad (4.9)$$

$$+ \frac{a_n}{i\mu}(1 - e^{i\mu\xi_{n-1}}) \quad , n > 1$$

$$b_1 = 0$$

where $b_1=0$ is due to the application of the apex Mach wave condition.

Since the b_i's are expressed in terms of a_i's, the latter can be evaluated by applying the tangency condition at the control points. In matrix form this condition can be expressed as

$$[W_{ji}]\ \{a_i\} = \{B_j\} \qquad (4.10)$$

where $[W_{ji}]$ can be expressed as $[V_{ji}]-R'(x_j)[U_{ji}]$ and V_{ji} and U_{ji} are the velocity influence coefficients in r and x directions respectively of the oscillatory flow at x_j, r_j due to the panel i. The right-hand-side of the tangency condition evaluated at the control point j is denoted by $\{B_j\}$, which represents the given downwash.

In supersonic flow, the governing equation is hyperbolic, the problem becomes an initial value problem; hence the matrix $[W_{ji}]$ is a lower tridiagonal one. The solution method for

solving the system of equations given by Eq. (4.10) is straightforward.

Once the $\{a_i\}$ are determined, we can compute the velocities and the potential at the control points and therefore the unsteady pressure coefficient. Once the unsteady pressures have been determined, the generalized forces, can be determined by using Eq. (2.43).

4.5 Results and Discussions

To verify the present method, numerical examples are presented in terms of unsteady pressures, stability derivatives, and generalized forces. Free-free mode aerodynamic damping for bodies in bending oscillations are presented for various configurations, including that of the Saturn SA-1 launch vehicle.

4.5.1 Results According to Various Coordinate Systems

Figures 10, 11 and 12 present the in-phase and out-of-phase pressure coefficients of a 10% thick cone at Mach number M_∞ =2.0 and reduced frequency k=2.0 in the wind-fixed, body-fixed and pseudo-wind-fixed coordinates. The oscillating cone performs in pitching mode, first-bending mode and second-bending mode, respectively. Free-free mode beam theory was used to determine these modes. For the rigid mode oscillation in Fig. 10 the pseudo-wind-fixed and the body-fixed systems become identical; thus only one result is presented.

In general, the results of the body-fixed and the pseudo-wind-fixed systems and those of the slender body theory (Ref. 6) are in good agreement. In contrast to these results, the in-

phase pressures of the wind-fixed results persistently show the effects of the apex singularity in all cases, as expected. Consequently, the overall pressure distributions downstream are contaminated by this singular behavior originated from the apex. It is noted that when the oscillation center x_G is placed at the apex, or the mode shape $g(x)$ at the apex is zero, the apex singularity disappears and all wind-fixed results are in close agreement with the others. Also, it can be observed that the pressures due to the flexible modes are one order higher than those of the rigid mode, and that the out-of-phase pressures resemble the mode shape. The reason for this latter behavior can be simply analyzed from the slender body limit. There, the out-of-phase pressure, as shown in Appendix C, is proportional to $(R(x)g(x))'$ and because $R(x)$ goes to zero at the apex, the dominant term is $R'(x)g(x)$.

From Figs. 13 through 18, generalized aerodynamic forces on a cone, a parabolic-ogive and a cone-cylinder oscillating in first and second bending modes with reduced frequency of $k=2.0$ are plotted versus freestream Mach number. (Due to the singularity originated from the apex, the generalized forces resulted from the wind-fixed coordinate system will not be presented here.) As expected, the present results approach the slender body results in the decreasing order of thickness.

While the pseudo-wind-fixed and body-fixed results are in satisfactory agreement, their deviations increase with increased Mach number and thickness. In Fig. 18, the sudden departure of the pseudo-wind-fixed phase angle (argument) could be caused by

the mode-shape/expansion-fan interaction which is further amplified by the second derivative term ϕ_{orr}. In general, it can be observed that again higher order modes result in higher value of generalized forces. For example, the magnitude (modulus) of the generalized forces for the second bending mode is about twice that of the first one.

In terms of the effects of Mach number, it can be seen that when the Mach number approaches the low supersonic regime, i.e. M_∞=1.5, all magnitudes increase rapidly. This trend is similar to that obtained for rigid modes. When approaching the higher Mach number range, the changing rate of the force magnitudes appears to be less sensitive to the Mach number for a given body thickness or given mode shape. Similar trends, in the high supersonic Mach number range, are found in the solution to Euler's equations for steady flow.

To simplify the matter, in the following sub-sections, only results in the body-fixed coordinate system, are presented.

4.5.2 Effects of Frequency

In the low frequency limit, the damping-in-pitch moment coefficients for a parabolic-ogive, an ogive-cylinder and a cone-frustrum body are presented in Figs. 19, 20 and 21. Throughout the supersonic range the present results are found in good agreement with those of Platzer's (Ref. 8) linearized method of characteristics (LMOC), Tobak and Wehrend's (Ref. 9) cone theory, which are limited to the low frequency domain, and various experimental data (Ref. 8). Across the frequency range, the magnitude and the phase angle of the generalized forces Q_{ij} for a

cone and an ogive in pitching motion are presented in Figs. 22a and 22b. The force magnitude increases with increased frequency, whereas the phase angle is less frequency dependent. Notice also that the effects of body shape become apparent in the high frequency range. All results merge in the low frequency limit. Similar trends were found in the sonic-flow studies by Landahl (Ref. 28).

In the high frequency limit, Fig. 23 presents results of the present method compared against the piston-theory (Ref. 29) results for a very slender parabolic ogive. The thickness ratio τ=.02 for this case is selected baased on the order analysis $\tau M_\infty k \ll 1$ and $M_\infty k > 1.0$ as required by the piston theory. For M_∞= 1.5 the agreement seems to be very good for the two selected reduced frequencies, k=4.0 and 7.5. It is also interesting to compare the effects of frequency and flow dimensionality on unsteady pressures. Figure 24 shows comparisons of unsteady pressure coefficients for a 5.7° cone and a flat plate pitching about the apex at M_∞=2.0. The flat plate results are computed by the LPP code (Ref. 30). As expected, the unsteady pressure magnitude for an oscillating cone is smaller than that of a flat plate at k=1.0 and k=2.0. Similar to the case of steady supersonic cone and wedge flow, the present finding shows that the cone in oscillation yields weaker compression than the flat plate as a result of the three dimensionality of the flow, irrespective of the oscillation frequency.

4.5.3 Nonlinear Results

The effects of the nonlinear mean-flow in the unsteady aerodynamic forces, are presented in Figs. 27 and 28. In these figures the legend "Present HPP" represents the HPP linear results to distinguish them from the "Present HPP nonlinear" results. It should be noted that the latter results are obtained based on the unsteady hybrid approach developed in Chapter 3.

Figure 27 shows that a good agreement of HPP nonlinear results with Brong's (Ref. 31) exact Euler unsteady results is obtained for the pitch-damping forces for a cone. The linear results deviate from the nonlinear ones as the Mach number increases. The nonlinear effect is enhanced by either increasing the hypersonic parameter $M_\infty \tau$ or by decreasing the Mach number toward the transonic range.

Figure 28 shows that the present HPP methods are in fair agreement with the measured damping-in-pitch moment coefficient for a 20% thick ogive-cylinder throughout the Mach number range. The computed results of SPINNER code (Ref. 32) and Ericsson's (Ref. 32) show large discrepancies with the measured data; in fact, weak dependency on the Mach number range was found in these results. By contrast, strong Mach number dependency is shown in the results of the HPP code, which show a favorable trend with the measured data. However, no appreciable difference is found between the HPP linear and nonlinear results for this case.

From these figures, it is seen that the unsteady aerodynamics can be altered substantially by the mean flow influence through the tangency condition and the pressure

coefficient. These improved results prompt further development of the nonlinear method for aeroelastic applications.

4.5.4 Elastic Bodies

Next, computed results of the HPP method for an elastic cone-cylinder body are compared with the aerodynamic damping data measured by Hanson and Dogget (Ref. 14) where the aerodynamic damping derivative is defined as

$$C_h^{\cdot} = 2k\mu(C_A/C_{cr}) = -\frac{I_m(Q_{11})}{\pi k} \qquad (4.11)$$

and μ is the mass ratio. Physically, this coefficient, $C_h^{\cdot}$, represents the ratio of aerodynamic damping to the critical damping. The reduced frequency of the first bending mode (Fig. 29a) lies in the range between 1.12 to 1.6 corresponding to M_∞=3.0 to 1.5. For the second bending mode (Fig. 29b), it lies between 2.9 and 4.2 for the same Mach number range. It is seen that the present results establish close trends with the measured data. By contrast, all quasi-steady theories yield inferior predictions. Due to an inconsistent formulation, in their boundary condition, Bond and Packard theory (Ref. 11) results in considerable discrepancy with the measured data, as can be seen in Fig. 29b.

Aeroelastic analysis of the Saturn SA-1 launch vehicle are presented in Figs. 30 and 31. Steady mean flow pressure, and the in-phase and out-of-phase pressures for the vehicle in rigid mode are computed in Figs. 30a to 30c. The in-phase and out-of-phase pressures practically follow the same trend as that predicted by

the slender body theory. Clearly the deviation between the slender body results and the present HPP results are due to the inclusion of the Mach number and the thickness effects in the latter approach.

The mode shape determined by experiments at NASA-Langley (Ref. 15) is used as input to compute the aerodynamic damping coefficient. This coefficient is now defined as $C_h = -Im(Q_{33})/nk\eta$, where "3" denotes the first bending mode and η is a parameter involving the body shape and the mode shape (η=1.763, see Ref. 15). The natural frequency for the actual vehicle is 2.8 Hertz. However, because of the large reference length, the reduced frequency k lies between 1.4 and 2.53 for a Mach number range of 3.0 to 1.2, respectively. Therefore, the present case of study needs an accurate prediction method in the high-frequency range. Again, good agreement is found between the present results and the measured data. To model this complex configuration, less than 100 panels were used in the prescribed frequency range. Consequently, only 30 seconds of CPU time in an IBM 3081 were needed to obtain all the data reported in Figs. 30 and 31.

CHAPTER 5

FLUTTER COMPUTATION

One of the main applications of unsteady aerodynamics is the computation of flutter. The phenomenon of flutter is a result of an interaction of aerodynamic forces and airframe response in such a way that the structure receives energy from the airstream rather than giving it up as damping. In this chapter the flutter boundaries for a 7.5° cone, in pitching and plunging oscillations are compared with experiments and different theories for different Mach numbers. The effects of the nonlinear mean flow are studied.

For the same cone the divergence boundary as a function of the Mach number is presented.

5.1 Flutter Equations

The equations of motion for a body in plunging and pitching oscillations as shown in Fig. 30 can be shown to be

$$\left.\begin{aligned} mh(t) + S_\alpha \alpha(t) + K_h h(t) &= -\frac{1}{2}\rho_\infty U_\infty^2 \left[Q_{11}\frac{h(t)}{L} + Q_{12}\alpha(t)\right] S_{ref} \\ S_\alpha h(t) + I_\alpha \alpha(t) + K_\alpha \alpha(t) &= -\frac{1}{2}\rho_\infty U_\infty^2 L \left[Q_{21}\frac{h(t)}{L} + Q_{22}\alpha(t)\right] S_{ref} \end{aligned}\right\} \tag{5.1}$$

where $h(t)$ and $\alpha(t)$ are the generalized coordinates for plunging and pitching respectively and are defined positive down for $h(t)$ and clockwise for $\alpha(t)$.

For harmonic oscillations $h(t)$ and $\alpha(t)$ can be expressed as $h(t)=h_o e^{i\omega t}$ and $\alpha(t)=\alpha_o e^{i\omega t}$. Using the conventional notation for the flutter equations we let $K_h=m\omega_h^2$, $K_\alpha=I_\alpha\omega_\alpha^2$, $\mu=m/\pi\rho\, LR(L)^2$ and $r^2=I_\alpha/mL^2$, where ω_h and ω_α are the natural frequencies of the body in plunging and pitching oscillations respectively, μ is the mass ratio, and r_α is the dimensionless radius of gyration about the pitch axis.

Eqs. (5.1) can now be expressed in a matrix form as follows

$$\begin{bmatrix} 1-\left(\frac{\omega_h}{\omega_\alpha}\right)^2\cdot\left(\frac{\omega_\alpha}{\omega}\right)^2-\frac{1}{2}\frac{Q_{11}}{\mu k^2} & \frac{x_G-x_\alpha}{L}-\frac{1}{2}\frac{Q_{12}}{\mu k^2} \\ \frac{x_G-x_\alpha}{L}-\frac{1}{2}\frac{Q_{21}}{\mu k^2} & r_\alpha^2\left(1-\frac{\omega_\alpha^2}{\omega^2}\right)-\frac{1}{2}\frac{Q_{22}}{\mu k^2} \end{bmatrix} \begin{Bmatrix} \frac{h(t)}{L} \\ \alpha(t) \end{Bmatrix} = \{0\} \tag{5.2}$$

In Eqs. (5.2) for a fixed Mach number the unknowns are ω, ρ_∞ and U_∞, which represent the flutter frequency, the altitude at which flutter will occur, and the flutter speed respectively. The U-g method (Ref. 33) is used to determine the flutter boundary. Complex roots are obtained by introducing the artificial structural damping factor g, and a root of the equation represents a point on the flutter boundary if the corresponding value of g equals zero. Thus Eqs. (5.2) are replaced by

$$\begin{bmatrix} 1 - \left(\frac{\omega_h}{\omega_\alpha}\right)^2 \lambda^2 - \frac{1}{2}\frac{Q_{11}}{\mu k^2} & \frac{x_G - x_\alpha}{L} - \frac{1}{2}\frac{Q_{12}}{\mu k^2} \\ \frac{x_G - x_\alpha}{L} - \frac{1}{2}\frac{Q_{12}}{\mu k^2} & r_\alpha^2(1-\lambda^2) - \frac{1}{2}\frac{Q_{22}}{\mu k^2} \end{bmatrix} \begin{Bmatrix} \frac{h(t)}{L} \\ \alpha(t) \end{Bmatrix} = \{0\} \tag{5.3}$$

where $\lambda^2 = \left(\frac{\omega_\alpha}{\omega}\right)^2 (1 + ig)$.

If flutter exists, h(t) and α(t) do not vanish identically. Thus, for a nontrivial solution to exist requires the determinant of the coefficient matrix of Eq. (5.3) be set to zero. Mathematically this amounts to solving an eigenvalue problem.

Solving the determinant for λ yields roots $(\lambda_1, \lambda_2, \ldots)$ from which a new frequency and damping value for each mode are obtained as follows

$$\omega_i = \frac{\omega_\alpha}{\text{Real}(\lambda_i)}$$

$$g_i = \left(\frac{\omega_i}{\omega_\alpha}\right)^2 \text{Imag}(\lambda_i)$$

The velocities corresponding to ω_i are obtained from k as

$$U_i = \frac{\omega_i L}{k} .$$

Since the generalized forces are functions of k the eigenvalue problem can be solved for a number of k's to obtain

$(\omega_i, g_i, U_i)_k$ for each k and plot a root locus (U-g) diagram. The zero crossing of a g locus denotes a flutter point.

5.2 Flutter Results

For a 7.5° cone at Mach numbers M_∞=2.0 and 3.0, the flutter boundaries in terms of flutter speeds and flutter frequencies versus the wind-off frequency ratio are presented in Figs. 31 and 32. Two rigid modes, plunging and pitching, are investigated. As reported in Ref. 16, the measured data were obtained in order to evaluate the sufficiency and the applicability of the then existing unsteady theories for flutter analysis, namely the quasi-steady (Q.S.) approaches (Refs. 10 and 13) and the frequency expansion theory (Ref. 7). For this reason, the reduced frequency range is confined to one below 0.4 so that the compared quasi-steady theories can be valid. While all methods yield rather accurate flutter frequencies, it is seen that the quasi-steady method fails to predict the flutter speed consistently with the measured data. The present method however consistently slightly underpredicts the flutter speed, whereas as expected the slender body theory predicts the most conservative boundary.

In order to investigate the effects of the nonlinear mean flow, the flutter boundaries for the same cone are now presented in Figs. 33 and 34 versus the Mach number for a wind-off frequency ratio of ω_h/ω_α=1.8. From the comparison with the measured data (Ref. 16) it is seen that consistent improvement in trends are obtained over the linear ones. However, the predicted boundaries become less conservative in the

order of slender body, the HPP linear and the HPP nonlinear results.

The phenomenon of divergence is inherent to the static aeroelasticity. Divergence occurs when the static moment created by the aerodynamic forces equals the elastic moment

$$L \; q \; S_{ref} \; \frac{\partial C_L}{\partial \alpha} = K_\alpha$$

In Ref. 16, the divergence parameter is defined as

$$\frac{2Lq\pi R(L)^2}{K_\alpha} = \frac{2}{\frac{\partial C_L}{\partial \alpha}} \; .$$

In Fig. 35 the divergence boundary for a 7.5° is presented versus the Mach number. Interestingly, the nonlinear results behave like the slender body results in this case, whereby the former show little dependency on Mach number up to M_∞=5.0.

CHAPTER 6

ASYMMETRIC BODIES

In this chapter, the formulation for an asymmetric body performing bending oscillations is presented. The differential equations, boundary conditions, and pressure coefficients in the body-fixed coordinate system are properly formulated, and the solution of the first order equation, using a spline panel method, is obtained. Comparisons of the steady and unsteady pressures, forces and moments for conical bodies of various cross sections are made with other methods, whenever available.

6.1 Formulation

As shown in Appendix A, Eq. (A.7), the full potential in the body-fixed system for asymmetric bodies can be written as

$$\Omega(x,y,z,t) = x + h_x(x,t)z + \Phi(x,y,z,t) \qquad (6.1)$$

The linearized equation for the perturbation potential Φ obtained by substituting Eq. (6.1) into Eqs. (2.2) and (2.3) is given in Appendix A by Eq. (A.13). There it is also shown that the governing equations for ϕ_0 and ϕ_1, in cylindrical coordinates, are given by

$$(1-M_\infty^2)\phi_{0xx} + \phi_{0rr} + \frac{1}{r}\phi_{0r} + \frac{1}{r^2}\phi_{0\theta\theta} = 0 \qquad (6.2)$$

$$(1-M_\infty^2)\phi_{1xx} + \phi_{1rr} + \frac{1}{r}\phi_{1r}$$

$$+ \frac{1}{r^2}\phi_{1\theta\theta} - 2ikM^2{}_\infty\phi_{1x} + M_\infty^2 k^2 \phi_1 = G_3(g,\phi_0) \qquad (6.3)$$

where $G_3(g,\phi_0)$ represents the mean flow and flexible mode interaction (like in Chapter 2 Eq. (2.23) for bodies of revolution) and is given explicitly as a function of g and ϕ_0 in Appendix A, Eq. (A.17).

6.1.1 Boundary Conditions

The condition at the apex Mach wave for asymmetric bodies is given by

$$\left.\begin{aligned} \phi_0 &= \phi_{0x} = \phi_{0r} = \phi_{0\theta} = 0 \\ \phi_1 &= \phi_{1x} = \phi_{1r} = \phi_{1\theta} = 0 \end{aligned}\right\} \text{ at } x \le \beta r \qquad (6.4)$$

and the condition of the velocity to be tangent to the body surface at all the times can be expressed (the same as Eq. (2.25) for bodies of revolution) as

$$(\nabla\Omega - \vec{V}_B)\cdot\vec{n} = 0 \qquad \text{at } S = 0 \qquad (6.5)$$

where V_B is the velocity of the body surface and is given by

$$\vec{V}_B = \dot{\delta}(t)[g'R\cos\theta\,\vec{e}_x - g(\cos\theta\,\vec{e}_r - \sin\theta\,\vec{e}_\theta)] \qquad (6.6)$$

S the body surface and n the outward normal to S. In the body-fixed coordinate system the body surface S is simply given by

$$S = r - R(x,\Theta) = 0 \tag{6.7}$$

The normal n is then obtained as

$$\vec{n} = \nabla S = - R_x \vec{e}_x + \vec{e}_r - \frac{R_\Theta}{R} \vec{e}_\Theta \tag{6.8}$$

The total velocity $\nabla\Omega$ is given in terms of the perturbation potential Φ in Appendix A, Eq. (A.8) as

$$\nabla\Omega = (1 + \Phi_x - h_{xx} z \Phi_x) \vec{e}_x + \Phi_y \vec{e}_y + (h_x + \Phi_z) \vec{e}_z \tag{6.9}$$

Now, expressing Eq. (6.9) in cylindrical coordinates and letting

$$\Phi(x,r,\Theta,t) = \phi_0(x,r,\Theta) + \delta(t)\ \phi_1(x,r,\Theta) \tag{6.10}$$

Eq. (6.9), when evaluated at the body surface, becomes

$$\begin{aligned} \nabla\Omega = {} & [1 + \phi_{0x}(1 - \delta(t)g''R\cos\Theta) + \delta(t)\phi_{1x}]\vec{e}_x \\ & + [\phi_{0r} + \delta(t)\phi_{1r} + \delta(t)g'\cos\Theta]\vec{e}_r \\ & + [\frac{1}{R}\phi_{0\Theta} + \delta(t)\frac{1}{R}\phi_{1\Theta} - \delta(t)g'\sin\Theta]\vec{e}_\Theta \quad \text{at } r=R(x,\Theta) \end{aligned} \tag{6.11}$$

Now substituting Eqs. (6.11), (6.8) and (6.6) into Eq. (6.5) and collecting like terms of order one and δ_0 yields

$$\phi_{0r} - R_x\phi_{0x} - \frac{R_\theta}{R^2}\phi_{0\theta} = R_x \qquad \text{at } r = R(x,\theta) \quad (6.12)$$

$$\phi_{1r} - R_x\phi_{1x} - \frac{R_\theta}{R^2}\phi_{1\theta} = -RR_x(g''\phi_{0x}+ikg')\cos\theta - (g' + ikg)(\cos\theta + \frac{R_\theta}{R}\sin\theta)$$

$$\text{at } r = R(x,\theta) \quad (6.13)$$

These are the boundary conditions for the mean flow and the cross flow for bodies of arbitrary cross section. It can be seen that when the body under consideration resumes its axisymmetry, (i.e. R_θ=0) Eqs. (6.13) and (6.12) reduce to Eqs. (2.30) and (2.31) respectively.

6.1.2 Pressure Coefficient

The relation between the time derivative in the wind-fixed system, t', and the body-fixed system, t, is provided by

$$\frac{\partial\Omega}{\partial t'} = \frac{\partial\Omega}{\partial t} - g'\dot{\delta}(t)r\frac{\partial\Omega}{\partial x}\cos\theta + g\dot{\delta}(t)(\cos\theta\frac{\partial\Omega}{\partial r} - \frac{1}{r}\sin\theta\frac{\partial\Omega}{\partial\theta}) \quad (6.14)$$

Now if Eqs. (6.10) and (6.1) are substituted into Eq. (6.14) (recall that $h(x,t)=g(x)\delta_0 e^{ikt}$) and retaining only up to linear terms in δ_0 yields

$$\frac{\partial \Omega}{\partial t'} = \dot{\delta}(t)\phi_1(x,r,\theta) - g'\dot{\delta}(t)r\phi_0(x,r,\theta)\cos\theta$$

$$+ \dot{\delta}(t)g(\phi_{0r}\cos\theta - \frac{1}{r}\phi_{0\theta}\sin\theta) \qquad (6.15)$$

Substituting Eqs. (6.15) and (6.11) into the exact isentropic pressure coefficient as given by Eq. (2.32) and performing binomial expansion according to the small parameter δ_0, we obtain

$$C_p = C_p^0 + \delta(t)\, C_p^1 \qquad (6.16)$$

where $C_p^0 = \frac{2}{\gamma M_\infty^2}[S_0^\gamma - 1]$ (6.17)

and $C_p^1 = -2S_0\{(1+\phi_{0x})(\phi_{1x}-Rg''\phi_{0x}\cos\theta) + \phi_{0r}(\phi_{1r}+g'\cos\theta)$

$$+ \frac{1}{R}\phi_{0\theta}(\frac{1}{R}\phi_{1\theta}-g'\sin\theta) - ikRg'\phi_{0x}\cos\theta + ik\phi_1$$

$$+ ikg(\phi_{0r}\cos\theta - \frac{1}{R}\sin\theta\phi_{0\theta})\} \qquad \text{at } r=R(x,\theta) \quad (6.18)$$

where S_0 is now defined as

$$S_0 = [1 - \frac{\gamma-1}{2}M_\infty^2(2\phi_{0x} + \phi_{0x}^2 + \phi_{0r}^2 + \frac{1}{R^2}\phi_{0\theta}^2)]^{1/\gamma-1}$$

The generalized forces will be given now by

$$Q_{ij} = \frac{-1}{S_{ref}} \int_0^{2\pi} \int_0^1 C_p^{1(j)} [(g^{(i)} + g'^{(i)} RR_x) R\cos\Theta +$$

$$g^{(i)} R_\Theta \sin\Theta] \, dx d\Theta \qquad (6.19)$$

Once the generalized forces are determined, the stability derivatives can be obtained from Eq. (2.44), in the similar manner as to determine those for axisymmetric bodies.

6.2 Mean Flow Solution and Results

To establish a robust unsteady computational procedure for asymmetric bodies it is more appropriate to investigate first the method of solution of the mean flow since there are more available data for result verification. The mean flow problem is governed by Eq. (6.2) with the boundary condition Eqs. (6.4) and (6.12).

If the velocities are to be single-valued function the dependency on the polar angle Θ must occur through factors $\cos(n\Theta)$ and $\sin(n\Theta)$, where n is an integer. The elementary solutions in this form that satisfy Eq. (6.2) were obtained by Ward (Ref. 34) (Chapter 9, Eq. (9.3.22)) as

$$\phi_o^{(n}(x,r,\Theta) = - \begin{matrix}\cos(n\Theta) \\ \sin(n\Theta)\end{matrix} \int_0^{x-\beta r} \frac{1}{(\beta r)^n} \frac{1}{2} \{(x-\xi+\sqrt{(x-\xi)^2-\beta^2 r^2})^n$$

$$+ (x-\xi-\sqrt{(x-\xi)^2-\beta^2 r^2})^n\} \frac{f_n(\xi)}{\sqrt{(x-\xi)^2-\beta^2 r^2}} \, d\xi \qquad (6.20)$$

The potential given by Eq. (6.20) can be considered as a distribution along the body axis of 'vortex multiplets' of strength $f_n(\xi)$. For the case n=0 Eq. (6.20) reduces to Eq. (3.4) representing a distribution of sources as presented in Chapter 3. Since Eq. (6.2) is linear a general solution can be obtained by superposition of elementary solution, thus $\phi_0(x,r,\Theta)$ can be expressed

$$\phi_0(x,r,\Theta) = \sum_{n=0}^{N} \phi_0^{(n}(x,r,\Theta) \qquad (6.21)$$

The functions $f_n(\xi)$ that appear in Eq. (6.21) should be obtained from the boundary conditions. But, before a numerical procedure to determine them is developed, it is convenient to estimate the magnitude of the different terms in the integrand of Eq. (6.20) to see if convergency difficulties can arise during the numerical solution. It can be seen that the terms $[x-\xi+\sqrt{(x-\xi)^2-\beta^2 r^2}]^n$ and $[x-\xi-\sqrt{(x-\xi)^2-\beta^2 r^2}]^n$ are of order 1 since x is defined between 0 to 1; however the term $1/(\beta r)^n$ when evaluated at the body surface is of order $1/\tau^n$, where τ is the thickness of the body. Thus, for thin bodies this term can be very large if the total number of elementary solutions, N, is large. For example for a 10% thick body if N is 12 those terms are of order 10^{12}. Therefore, if the velocities have to be of the order of the thickness τ means that the functions $f_n(\xi)$ must be of order 10^{-12}. This implies that numerical difficulties should be expected if Eq. (6.21) is used to solve for the mean flow potential ϕ_0. To make the term $1/\tau^N$ small the body thickness τ has to be large, which

is in contradiction with the assumptions of small disturbances, or N has to be small. Since N will depend, in general, on the body cross section, this latter condition can not be guaranteed. Thus, the application of this method to develop a robust computational method should be disregarded.

Thus, Eq. (6.2) should be attempted to be solved by a method that guarantees N to be small. Eq. (6.21) can be considered, with respect to the dependency on θ, as if the mean flow potential ϕ_0 is fitted by $\cos(n\theta)$ and $\sin(n\theta)$ functions in the interval $0 \le \theta \le 2\pi$. Drawing the analogy of this method with the curve-fitting method would be like if in the latter a polynomial of N^{th} degree were used to fit a function s(x). However it is known that if a spline fit is used the curve s(x) can be fitted, with good accuracy, by piecewise low order polynomials. Thus, if the concept of the spline fit is used to solve for Eq. (6.2) it will amount to divide the body into interval along the θ direction, i.e.

$0 = \theta_1 < \theta_2 < \ldots < \theta_{j-1} < \theta_j < \theta_{j+1} < \ldots < \theta_N < \theta_{N+1} = 2\pi$, each interval defined by $\Delta\theta_j = \theta_{j+1} - \theta_j$ (see Fig. 36). On the interval $\Delta\theta_j$, the potential ϕ_0 ca be expressed, i.e. as

$$\phi_{0,j}(x,r,\theta) = \sum_{n=0}^{2} \phi_{0,j}^{(n)}(x,r,\theta) \quad , \qquad \theta_j \le \theta \le \theta_{j+1} \tag{6.22}$$

where $\phi_0^{(0)}$, $\phi_0^{(1}$ and $\phi_0^{(2}$ are given respectively by

$$\phi_{0,j}^{(0)} = -\int_0^{x-\beta r} \frac{f_{0,j}(\xi)}{\sqrt{(x-\xi)^2 - \beta^2 r^2}}\, d\xi \tag{6.23}$$

$$\phi^{(1}_{0,j} = -\cos\theta \int_0^{x-\beta r} \frac{1}{\beta r} \frac{(x-\xi) f_{1,j}(\xi)}{\sqrt{(x-\xi)^2-\beta^2 r^2}}\, d\xi \qquad (6.24)$$

$$\phi^{(2}_{0,j} = -\cos 2\theta \int_0^{x-\beta r} \frac{1}{(\beta r)^2} \frac{(2(x-\xi)^2-\beta^2 r^2) f_{2,j}(\xi)}{\sqrt{(x-\xi)^2-\beta^2 r^2}} d\xi \qquad (6.25)$$

where only $\cos(n\theta)$ functions have been considered.

On each interval $\Delta\theta_j$ a set of M points is distributed on the body surface with coordinates (x_i, r_i, θ_j) i=1,...M, where $\theta_j = 1/2(\theta_j + \theta_{j+1})$ and $r_i = R(x_i, \theta_j)$, such that $x_i < x_{i+1}$. Thus, a total of M×N points on the body surface are located which are called the control points. From each control point the intersection of the inverse Mach cone with the body axis is determined, to obtain $\xi_{i+1,j} = x_i - \beta r_j$ with $\xi_{1,j}$ being the body apex. The interval $\xi_{i,j}$ to $\xi_{i+1,j}$ is called a panel. On each panel the strengths of the sources ($f_{0,j}$), dipoles ($f_{1,j}$) and quadrupoles ($f_{2,j}$) is assumed to vary linearly, i.e.

$$\left.\begin{aligned} f_{0,j}(\xi) &= a_{i,j}\xi + b_{i,j} \\ f_{1,j}(\xi) &= c_{i,j}\xi + d_{i,j} \\ f_{2,j}(\xi) &= e_{i,j}\xi + \ell_{i,j} \end{aligned}\right\} \qquad \xi_i \le \xi \le \xi_{i+1} \qquad (6.26)$$

If the condition that the functions $f_{0,j}$, $f_{1,j}$, and $f_{2,j}$ must be continuous between each two panels is imposed, the constants $b_{i,j}$ can be expressed as a function of $a_{i,j}$, $b_{1,j}$, and $d_{i,j}$ of $c_{i,j}$, $d_{i,j}$ and $\ell_{i,j}$ of $e_{i,j}$, $\ell_{1,j}$. The constants $b_{1,j}$, $d_{i,j}$ and $\ell_{i,j}$ can be shown to be zero when the boundary condition at the Mach

wave emanating from the apex is satisfied. Thus the potential at the control point x_n, r_n, Θ_j can be shown to be after integration

$$\phi_0\ (x_n, r_n, \bar{\Theta}_j) = \sum_{i=1}^{n} - \left\{ a_{i,j} \left[(x_n - \xi) \cosh^{-1} \left(\frac{x_n - \xi}{\beta r_n} \right) \right.\right.$$

$$\left. - \sqrt{(x_n - \xi)^2 - \beta^2 r_n^2} \right] + \left[\left(\frac{c_{i,j}}{2} \right) \frac{x_n - \xi}{\beta r_n} \sqrt{(x_n - \xi)^2 - \beta^2 r_n^2} \right.$$

$$\left. - \beta r_n \cosh^{-1} \frac{x_n - \xi}{\beta r_n} \right] \cos \bar{\Theta}_j + e_{i,j} \frac{\beta r_n}{8}$$

$$\left[\frac{1}{3} \left\{ \left(\frac{(x_n - \xi) + \sqrt{(x_n - \xi)^2 - \beta^2 r_n^2}}{\beta r_n} \right)^3 \right.\right.$$

$$\left. - \left(\frac{\beta r_n}{x_n - \xi) + \sqrt{(x_n - \xi)^2 - \beta^2 r_n^2}} \right)^3 \right\}$$

$$+ \frac{\beta r_n}{(x_n - \xi) + \sqrt{(x_n - \xi)^2 - \beta^2 r_n^2}}$$

$$\left. \left. - \left(\frac{(x_n - \xi) + \sqrt{(x_n - \xi)^2 - \beta^2 r_n^2}}{\beta r_n} \right) \right] \cos (2\bar{\Theta}_j) \right\} \Bigg|_{\xi_{i,j}}^{\xi_{i+1,j}} \tag{6.27}$$

The velocities in the x,r,Θ directions can be obtained by applying the derivatives with respect to x,r, and Θ respectively. Thus, the mean flow potential and velocities can be expressed as function of 3M×N unknown constants $a_{i,j}$, $c_{i,j}$ and $e_{i,j}$ i=1,...M, j=1,...N. If the conditions that the potential as well as the tangential velocity in the Θ direction must remain continuous

between adjacent intervals i.e. $\Delta\theta_j$ to $\Delta\theta_{j+1}$ are imposed, a set of 2M×N equations relating $a_{i,j}$, $c_{i,j}$ and $e_{i,j}$ are obtained. These equations can be used to express, i.e. the $c_{i,j}$'s and the $e_{i,j}$'s as functions of the $a_{i,j}$'s. Now, by satisfying the tangency condition at the control points the $a_{i,j}$'s can be determined. Once the $a_{i,j}$'s are known, the velocities at the control points can be evaluated and from Eq. (6.17) the pressure coefficient.

It should be noted that the number of elementary solutions chosen, three in the above description, can be altered. For example, if instead of imposing the continuity in the tangential velocity in the θ direction, only the potential is required to be continuous between adjacent intervals, only two elementary solutions, i.e. sources and dipoles need to be considered on each interval. Also any other set of vortex multiplets, instead of sources, doublets and quadrupoles, can be used and the type of vortex multiplets used can change from one interval, $\Delta\theta_j$, to the next $\Delta\theta_{j+1}$. This method can be called spline panel method.

The simplest application of the method of solution described above is if only one elementary solution on each interval is considered. In that case, the potential and its derivatives in the θ direction are not continuous between adjacent intervals. The best choice of elementary solutions is the source distribution, since it is known to be the exact solution of the mean flow potential for bodies of revolution. Thus, the use of source singularities of different strength on each interval $\Delta\theta_j$ amounts to treating locally the body as a body of revolution with

radius $R(x,\Theta_j)$. Therefore, some restrictions regarding the arbitrariness of the body cross section at which this first approximation can be applied, should be expected.

In the Fig. 37 the mean flow pressure for a conical body at Mach number $M_\infty=2.0$ whose cross section varies as $\cos\Theta$ is compared, at x=1, with Devan's results (Ref. 35), and USSAERO results. It can be seen that except in the region $\Theta^\circ \leq \Theta \leq 30^\circ$, the agreement seems to be very good with both methods. The deviation in that region we believe is due to the use of only one elementary solution on each interval. However it is seen that this small deviation does not affect in the prediction of the axial and normal forces when compared to the other two methods. The small difference between Devan's results and USSAERO results can be due to the different method used to solve the differential equation. The first used the finite difference method while the second used the panel surface method. The computer time taken by these two methods is at least one order of magnitude larger than the present method.

In the Fig. 38 the mean flow pressure for a conical body of circular cross section for $-\pi/2 \leq \Theta \leq \pi/2$ and elliptical, with ellipticity ratio 1/2, for $\pi/2 \leq \Theta \leq 3/2\pi$ at Mach number $M_\infty=2.0$ is compared with Devan's (Ref. 35) and USSAERO results. It can be seen that a slight deviation occurs overall the values of Θ when compared to the other two methods and the normal force coefficient has a difference of about 6%. However the axial force coefficient is very well predicted. The reason for the discrepancy is that an ellipticity ratio of 1/2 is, too low for

the present method to produce accurate results. As will be shown later for ellipticity ratio of 0.75 to 1.3, the present method gives good agreement when compared to USSAERO results.

6.3 Unsteady Flow Solution and Results

The unsteady flow problem is governed by Eq. (6.3) with the boundary conditions Eqs. (6.4) and (6.13). Like for bodies of revolution, Chapter 4, only the homogeneous unsteady wave equation will be solved. The term $G_3(g,\phi_0)$ can be taken into account in a similar manner to that described for bodies of revolution Eq. (4.1).

To extend the method described in the previous section to unsteady flow it is necessary first to obtain a general elementary solution, equivalent to Eq. (6.20) for the mean flow, for the unsteady flow. This solution can be assumed in the form

$$\phi_1^{(n}(x,r,\Theta) = -\begin{matrix}\cos(n\Theta)\\ \sin(n\Theta)\end{matrix}\int_0^{x-\beta r} F_n(\xi)\, e^{-i\mu(x-\xi)}\, \frac{\cos\left(\gamma\sqrt{(x-\xi)^2-\beta^2 r^2}\right)}{\sqrt{(x-\xi)^2-\beta^2 r^2}}$$

$$m\left(\cosh^{-1}\left(\frac{x-\xi}{\beta r}\right);\ n\right)\, d\xi \qquad (6.28)$$

where $e^{-i\mu(x-\xi)}\ \frac{\cos\left(\gamma\sqrt{(x-\xi)^2-\beta^2 r^2}\right)}{\sqrt{(x-\xi)^2-\beta^2 r^2}}$ represents the kernel

for a distribution of unsteady sources along the body axis, and it is known to satisfy the equation (see Garrick (Ref. 26))

$$(1-M_\infty^2)\ \phi_{1xx} + \phi_{1rr} + \frac{1}{r}\ \phi_{1r}$$

$$- \frac{n^2}{r^2}\ \phi_1 - 2ikM_\infty^2\ \phi_{1x} + k^2M_\infty^2\ \phi_1 = 0 \quad \text{when } n=0. \qquad (6.29)$$

Thus, in Eq. (6.28) m represents a function of x,r,ξ and n to modify the source kernel so it satisfies Eq. (6.29) for n different of zero. Then, m must satisfy $m(x,\xi,r;\ 0)=1$. To determine m we first make the following transformation in Eq. (6.28)

$$\xi = x - \beta r \cosh \sigma \qquad d\xi = - \beta r \sinh \sigma\ d\sigma$$

$$\text{at } \xi = 0 \qquad \sigma = \cosh^{-1} \frac{x}{\beta r}$$

$$\text{and at } \xi = x-\beta r \qquad \sigma = 0$$

Eq. (6.28) then becomes

$$\phi_1^{(n}(x,r,\Theta) = \begin{matrix}\cos(n\Theta)\\ \sin(n\Theta)\end{matrix}\int_0^{\cosh^{-1}(\frac{x}{\beta r})} F_n(x-\beta r\cosh\sigma)e^{-i\mu\beta r\cosh\sigma}$$

$$\cos(\gamma\beta r\sinh\sigma)\ m(\sigma;n)\ d\sigma \qquad (6.30)$$

To determine $m(\sigma;n)$ the derivatives with respect to x and r in Eq. (6.30) are determined and substituted into Eq. (6.29). In this way it can be shown that Eq. (6.30) satisfies Eq. (6.29) if $m''-n^2m=0$. Therefore, the solution to this equation together with the condition $m(\sigma;0)=1$, implies that m should be

$m(\sigma;n)=\cosh(n\sigma)$. Thus, the generalized elementary solution of Eq. (6.29) is given by

$$\phi_1^{(n}(x,r,\Theta) = \begin{matrix}\cos(n\Theta)\\ \sin(n\Theta)\end{matrix}\int_0^{\cosh^{-1}(\frac{x}{\beta r})} F_n(x-\beta r\cosh\sigma)e^{-i\mu\beta r\cosh\sigma}$$

$$\cos(\gamma\beta r\sinh\sigma)\ \cosh(n\sigma)\ d\sigma \qquad (6.31)$$

Now, the extension of the spline panel method to unsteady flow can be done by letting

$$\phi_{1,j}(x,r,\Theta) = \sum_{n=0}^{2} \phi_{1,j}^{(n}(x,r,\Theta)\ ,\quad \Theta_j \le \Theta \le \Theta_{j+1} \qquad (6.32)$$

where $\phi_{1,j}$ means the unsteady flow potential at the interval j. $\phi_1^{(0}(x,r,\Theta)$ represents a distribution of unsteady sources along the body axis, $\phi_1^{(1}$ of unsteady doublets (it can be shown that $\phi_1^{(1}$ is equal to that given by the first term in Eq. (4.1) for bodies of revolution by integrating by parts), and $\phi_1^{(2}$ of unsteady quadrupoles. The Harmonic Gradient concept needs now to be applied to the strengths $F_{0,j}(\xi)$, $F_{1,j}(\xi)$, and $F_{2,j}(\xi)$ in a similar manner as was done in Chapter 4, Eq. (4.6) for $F_1(\xi)$.

The integration of $\phi_1^{(0}$, and $\phi_1^{(2}$ will not be carried out here; however it is similar to that shown in Appendix B for bodies of revolution (which is the same as for $\phi_1^{(1}$). Once the integration is done the method of solution to determine ϕ_1, and the velocities ϕ_{1x}, ϕ_{1r} and $1/r\phi_{1\Theta}$, at the control points is the

same as the one described in the previous section for the mean flow.

Since for the mean flow numerical results were determined using only one elementary solution on each interval $\Delta\Theta_j$, consistently the same will be done for the unsteady flow. Thus, on each interval a distribution of unsteady doublets of strength $F_{1,j}(\xi)$ is distributed. Like for bodies of revolution the doublet strength is discretized along the body axis and the Harmonic Gradient concept is applied.

For the unsteady flow a set of conical bodies of elliptic cross section and ellipticity ratio a/b from 0.75 to 1.3 have been investigated, at Mach number M_∞=3.0, and compared, whenever possible with USSAERO results.

In the Figs. 39 and 40 the static normal force and moment coefficients are presented versus a/b and compared to those obtained from the USSAERO code. It can be seen that good agreement is obtained for both coefficients within the range studied.

In the Fig. 41 the dynamic normal force and moment coefficients are presented versus a/b. No comparison with other theories is made since, apparently, this is the first method able to compute the unsteady aerodynamics, for bodies of arbitrary cross section, in supersonic flow. At the present time no experimental data for the unsteady coefficients could be found. However since the static coefficients, within the range studied, are in good agreement with the USSAERO results, it is expected

that the unsteady coefficients should also be well predicted by the present method.

In the Figs. 42, 43 and 44 the real and imaginary part of the pressure coefficient for the elliptic cones in rigid, first bending, and second bending mode respectively are presented at $\Theta=0$, and reduced frequency $k=1.0$, along the x axis. In general we can see that the imaginary part of the pressure coefficient slightly changes with the ellipticity ratio, and that when a/b approaches one, the present results approach, as expected, those obtained for the body of revolution.

In the Figs. 45, 46 and 47, the real and imaginary part of the pressure coefficient, for rigid, first bending and second bending mode respectively are presented versus Θ at $x=1$. The real part of the pressure coefficient for the case $a/b=0.75$ deserves some attention. To investigate this behavior the pressure coefficient for an elliptic cone ($a/b=.75$) and a circular cone at steady angle of attack are compared to the pressure coefficient for a flat plate, obtained from the slender wing theory (Ref. 5) along the y axis in Fig. 48. Although for the present time lower values of a/b have not been obtained, it can be seen that the trend in pressure of the present method is the same as that obtained from the slender wing theory except in the region where y/b approaches one, where, for a flat plate, the pressure becomes singular.

It is interesting to notice that when a/b decreases the body becomes, as expected, more stable statically and dynamically. However, from the structural point of view we would say that the

body becomes more flexible and it might turn out to be more likely to flutter. Since the present approach has no limitations regarding frequency or mode shape it can be an excellent tool to estimate the advantages, from the stability point of view, and the disadvantages, from the aeroelastic point of view, of letting the ellipticity ratio to decrease and, thus, to obtain an optimized cross section body shape.

CHAPTER 7

BUNDLED TRIPLET METHOD

7.1 New Development of BTM

As mentioned in Chapter 6 using Fourier representation of an arbitrary body shape would introduce a formulation involving higher-order kernel function, which makes the determinant evaluation very difficult. On the other hand, the Splined-Panel Method used in the same chapter has shown limitations on the degree of asymmetry for bodies, which indicates that this method may not be general enough to handle arbitrary body-wing combinations. The proper treatment of the body-wing interference mandates to generalize the Spline-Panel method to the Bundle Triplet Method (BTM) in which at least two substantial features have been added. First, to keep the kernel function in low order, multiple lines of low order singularities, namely line sources and line doublets, are employed. Second, by using a least square procedure, the BTM can account for the circumferencial influence between panel elements, thus the method is sufficient to treat bodies of arbitrary cross-sections. As can be seen in the later computed cases, the results obtained by the BTM are all in good agreement with existing theories and measured data.

7.2 Formulation

As shown in Figs. 49 and 50 the body cross section is divided into 'M' intervals. Each interval contains a finite sector $\Delta\theta_m$, where $\Delta\theta_m = \theta_{m+1} - \theta_m$, $m = 1, \ldots M$, and $\theta_1 = 0$,

$\theta_{m+1} = 2\pi$. A three-dimensional "pie" shape is defined by a portion of the body within the sector $\Delta\theta_m$ whose vertex lies along the body axis. A line distribution of sources and another of doublets are superposed along the body axis for each pie segment. Within each pie segment an integral solution can be expressed as based on the superposition principle,

$$\phi_i(x_i, r_i, \bar{\sigma}_m) = \int_0^{x_i-\beta r_i} F_m(\xi) B(x_i - \xi, \beta r_i) d\xi$$

$$+ \int_0^{x_i-\beta r_i} G_m(\xi) \frac{\partial}{\partial r_i} B(x_i - \xi, \beta r_i) d\xi \cdot \cos\bar{\theta}_m \qquad (7.1)$$

$$+ \int_0^{x_i-\beta r_i} H_m(\xi) \frac{\partial}{\partial r_i} B(x_i - \xi, \beta r_i) d\xi \cdot \sin\bar{\theta}_m$$

where (x_i, r_i, θ_m) represents a typical control point lying on the body surface $r_i = R(x_i, \bar{\theta}_m)$ and $\bar{\theta}_m = (\bar{\theta}_m + \bar{\theta}_{m+1})/2$. The kernel function $B(x_i - \xi, \beta r_i)$ can be expressed as

$$B(x_i - \xi, \beta r_i) = e^{-i\mu(x_i-\xi)} \cdot \frac{\cos(\lambda R_o)}{R_o}$$

where $R_o = [(x_i - \xi)^2 - \beta^2 r_i^2]^{1/2}$ (7.2)

$$\mu = kM_\infty^2/\beta^2, \quad \lambda = kM_\infty/\beta^2$$

$F_m(\xi)$ denotes the source strength distribution and $G_m(\xi)$ and $H_m(\xi)$ the doublet strengths distributions in the m^{th} interval.

The fact that the doublet distribution has two unknown functions can be interpreted as that the doublet strength as well as the direction of the doublet axis are required to be determined. It is clear now, our triplet model is a "generalized triplet" in that the singularity strength functions are different from each other. In the case of $F_m = G_m = H_m$, the generalized triplet model then reduces to the regular triplet model (see Ref. 36).

Furthermore, along the body axis, each of the triplet lines is discretized by N segments where $\Delta\xi_{j,m} = \xi_{j+1,m} - \xi_{j,m}$ for a given pie sector $\Delta\theta_m$ (See Figs. 49 and 50). Also along the body axis, different source and doublet strength functions are discretized as $F_m^j(\xi)$, $G_m^j(\xi)$ and $H_m^j(\xi)$ within $\Delta\xi_{j,m}$. The velocity potential within this sector can then be expressed as

$$\phi_1(x_i, r_i, \bar{\theta}_m) = \sum_{j=1}^{i} \int_{\xi_j}^{\xi_{j+1}} F_{j,m}(\xi)\, B(x_i - \xi, \beta r_i)\, d\xi$$

$$+ \sum_{j=1}^{i} \int_{\xi_j}^{\xi_{j+1}} G_{j,m}(\xi) \frac{\partial}{\partial r_i} B(x_i - \xi, \beta r_i)\, d\xi \cdot \cos\bar{\theta}_m \quad (7.3)$$

$$+ \sum_{j=1}^{i} \int_{\xi_j}^{\xi_{j+1}} H_{j,m}(\xi) \frac{\partial}{\partial r_i} B(x_i - \xi, \beta r_i)\, d\xi \cdot \sin\bar{\theta}_m$$

7.3 Harmonic Gradient Model

To achieve computation accuracy and effectiveness in the high-reduced frequency and/or the low Mach number domains, it is essential to render the doublet solution uniformly valid in the

complete k and M_∞ domains. This can be simply achieved by modeling the doublet solution to maintain spatially harmonic in the mean flow direction. In so doing, the panel size $\Delta\xi_j$ is regulated and is made compatible to the wave number generated by the body oscillation. This is known as the Harmonic Gradient (H-G) model introduced in Ref. 4.

Here, the H-G model employed for wings (Ref. 4) is adopted to combine with the Bundle Triplet solutions. Application of the H-G model to Eq. (7.3) amounts to stating that in the interval $\xi_{j,m} < \xi < \xi_{j+1,m}$,

$$F_{m,j}(\xi) = a_{j,m}(1 - e^{-i\mu\xi})/i\mu \tag{7.4a}$$

for the source solution, and

$$\frac{\partial G_{j,m}(\xi)}{\partial \xi} = (b_{j,m}\xi + d_{j,m})e^{-i\mu(x_i-\xi)} \tag{7.4b}$$

$$\frac{\partial H_{j,m}(\xi)}{\partial \xi} = (C_{j,m}\xi + h_{j,m})e^{-i\mu(x_i-\xi)} \tag{7.4c}$$

for the doublet solutions.

Note that Eqs. (7.4b) and (7.4c) are the direct application of the H-G model whereas Eq. (7.4a) is a new extension of the H-G model to the source solution. It can be shown that both constants $d_{j,m}$ and $h_{j,m}$ can be expressed in terms of $b_{j,m}$ and $c_{j,m}$ respectively when a continuity condition in G_m and H_m is imposed between the adjacent segments. Introducing Eqs. (7.4a,b,c) to, and further discretization of the kernel integrals of Eq. (7.3) result in

$$\phi_i(x_i, r_i, \bar{\theta}_m) = \sum_{j=1}^{i} a_{m,j} S_j^{j+1} + (b_{j,m}\cos\bar{\theta}_m + C_{j,m}\sin\bar{\theta}_m) D_j^{j+1}) \qquad (7.5)$$

where S_j^{j+1} and D_j^{j+1} represent the induced potentials per unit source and doublet strengths respectively by the j^{th} segment of the triplet line at the point $(x_i, r_i, \bar{\theta}_m)$; they are given by

$$S_j^{j+1} = \int_{\xi_j}^{\xi_{j+1}} \left[\frac{e^{-i\mu x_i} - e^{-i\mu(x_i-\xi)}}{i\mu}\right] \frac{\cos\lambda R_o}{R_o} \, d\xi \qquad (7.6)$$

and

$$D_j^{j+1} = \int_{\xi_j}^{\xi_{j+1}} \frac{\partial}{\partial r_i} S(x_i - \xi, \beta r_i) d\xi \qquad (7.7)$$

where

$$S(x_i - \xi, \beta r_i) = \int_{\beta r_i}^{x_i - \xi} \frac{\cos(\lambda\sqrt{\tau^2 - \beta r_i^2})}{\sqrt{\tau^2 - \beta^2 r_i^2}} \, d\tau$$

Evaluations of D_j^{j+1} as well as its derivatives, with respect to x_i and r_i, are identical to those shown for bodies of revolution in Appendix B. For detailed evaluations of S_j^{j+1} and its derivatives, with respect to x_i and r_i, one is referred to Appendix D. There it is shown that after a transformation these integrals can easily be evaluated numerically by Gaussian quadrature.

The domain of influence is defined by a pie segment bounded by the sector $\Delta\theta_m$ and the inversed Mach cone intersection with

respect to P_i. Hence the effective triplet line is confined to the part from the body apex to the i^{th} segment where the discretized kernel integrals S_j^{j+1} and D_j^{j+1} represent the induced potential per unit source and doublet strengths by the j^{th} segment of the triplet line. Moreover, it should be noted that the steady mean flow potential ϕ_0 at the point (x_i, r_i, σ_m) can be obtained from Eq. (7.5) by letting k=0 in S_j^{j+1} and D_j^{j+1}.

7.4 Least Square Procedure

For convenience, a surface panel is defined as a body surface element whose area is bounded by $R \cdot \Delta\theta_m$ and $\Delta\ell_j$. A control point is located at $(x_i, R_i(x_i, \theta_m), \theta_m)$, the central point of each panel, where i=1,...N, m=1,...M, and $\theta_m=(\theta_m + \theta_{m+1})/2$. To obtain the potential values of $\phi_{i,m}$ at the control point, one of the effective ways is to relate the unknowns $a_{j,m}$, $b_{j,m}$ and $c_{j,m}$ to the cross flow potential $\phi_{i,m}$ by means of the method of weighted least squares. (For simplicity, we have dropped the subscript "1" in $\phi_{1i,m}$, hereafter.)

To apply the least square method one considers the induced potential by the singularities distributions at the m^{th} pie segment $\Delta\sigma_m$ at the points (x_i, r_i, θ_{m-1})* and (x_i, r_i, θ_{m+1}), i.e.

$$\phi_1(x_i, r_i, \bar{\theta}_{m-1}) = \sum_{j=1}^{i} a_{j,m} S_j^{j+1} + (b_{j,m}\cos\bar{\theta}_{m-1} + c_{j,m}\sin\bar{\theta}_{m-1}) D_j^{j+1}$$

and (7.7)

$$\phi_1(x_i, r_i, \bar{\theta}_{m+1}) = \sum_{j=1}^{i} a_{j,m} S_j^{j+1} + (b_{j,m}\cos\bar{\theta}_{m+1} + c_{j,m}\sin\bar{\theta}_{m+1}) D_j^{j+1}$$

* It should be noted that for this point $r_i = R(x_i, \bar{\theta}_{m-1})$ and for the next $r_i = R(x_i, \bar{\theta}_{m+1})$.

Let $\phi_{i,h}$ be the exact value of the potential at the body surface, the source- and doublet-strength solutions, due to the lease square approach, are the ones that minimize the residual

$$I = \frac{1}{2}\sum_{h=m-1}^{m+1} W_h\{[\sum_{j=1}^{i} a_{j,m}S_j^{j+1} + (b_{j,m}\cos\theta_h + c_{j,m}\sin\theta_h)D_j^{j+1}] - \phi_{i,h}\}^2 \quad (7.8)$$

where S_j^{j+1} and D_j^{j+1} are now evaluated at the control point $(x_i, R_i(x_i,\theta_h)\theta_h)$; $\phi_{i,h}$ represents the exact value of the potential at the i^{th} point and W_h are the introduced weight functions. Note that Eq. (7.8) is a least square procedure set up for three adjacent panels, namely from (m-1) to (m+1). Thus, imposing

$$\frac{\partial I}{\partial a_{i,m}} = \frac{\partial I}{\partial b_{i,n}} = \frac{\partial I}{\partial c_{i,m}} = 0 \quad (7.9)$$

yield,

$$\sum_{h=m-1}^{m+1} W_h\{\sum_{j=1}^{i} a_{j,m}S_j^{j+1} + (b_{j,m}\cos\bar{\theta}_h + c_{j,m}\sin\bar{\theta}_h)D_j^{j+1} - \bar{\phi}_{i,h}\}S_i^{i+1} = 0$$

$$\sum_{h=m-1}^{m+1} W_h\{\sum_{j=1}^{i} a_{j,m}S_j^{j+1} + (b_{j,m}\cos\bar{\theta}_h + c_{j,m}\sin\bar{\theta}_h)D_j^{j+1} - \phi_{i,h}\}D_i^{i+1}\cos\bar{\theta}_h = 0$$

$$\sum_{h=m-1}^{m+1} W_h\{\sum_{j=1}^{i} a_{j,m}S_j^{j+1} + (b_{j,m}\cos\bar{\theta}_h + c_{j,m}\sin\bar{\theta}_h)D_j^{j+1} - \bar{\phi}_{i,h}\}D_i^{i+1}\sin\bar{\theta}_h = 0 \quad (7.10)$$

These equations can be expressed in matrix form as

$$[A]_i \begin{Bmatrix} a_{j,m} \\ b_{j,m} \\ c_{j,m} \end{Bmatrix} + \sum_{j=1}^{i-1} [Y]_{j,i} \begin{Bmatrix} a_{j,m} \\ b_{j,m} \\ c_{j,m} \end{Bmatrix} = [H]_i \begin{Bmatrix} \bar{\phi}_{i,m-1} \\ \bar{\phi}_{i,m} \\ \phi_{i,m+1} \end{Bmatrix} \quad (7.11)$$

The matrices $[A]_i$, $[Y]_{j,i}$ and $[H]_i$ are given in Appendix E.

We can now relate the unknowns $a_{i,m}$, $b_{i,m}$ and $c_{i,m}$ to $\phi_{i,m-1}$, $\phi_{i,m}$ and $\phi_{i,m+1}$ by a least square matrix [LS], i.e.:

$$\begin{Bmatrix} a_{i,m} \\ b_{i,m} \\ c_{i,m} \end{Bmatrix} = [LS]\{\phi_{i,m}\} \tag{7.12}$$

for i = 1...N and m=1,...M. On the LHS of Eq. (7.12), the column vector has the dimension of (3xNxM), while on the RMS, [LS] is a matrix of dimension (3xNxM)x(NxM), and the unknown potential $\phi_{i,m}$ is a column vector of dimension (NxM).

Hence, the velocities at the control point can be expressed as:

$$\{\frac{\partial \phi}{\partial x_i}\} = [U][LS]\{\phi_{i,m}\} \tag{7.13}$$

$$\{\frac{\partial \phi}{\partial r_i}\} = [V][LS]\{\phi_{i,m}\} \tag{7.14}$$

$$\{\frac{1}{r_i}\ \frac{\partial \phi}{\partial \theta_m}\} = [W][LS]\{\phi_{i,m}\} \tag{7.15}$$

where [U], [V] and [W] are matrices of dimension (NxM)x(3xNxM) containing the velocity influence coefficients in the x, r and θ direction. Now, the velocities $\frac{\partial \phi}{\partial x_i}$, $\frac{\partial \phi}{\partial r_i}$ and $\frac{1}{r_1}\frac{\partial \phi}{\partial \theta_m}$ in the tnagency condition, Eq. (6.13), can be replaced by the cross flow potential $\phi_{i,m}$ through Eqs. (7.13-15). Consequently, $\{\phi_{i,m}\}$ is the unknown to be solved in Eq. (6.13)

In passing, we note that the evaluation of the steady mean flow potential follows the same procedure as described above,

except that the kernel integrals S_j^{j+1} and D_j^{j+1} are to be replaced by their steady counterparts.

7.5 Panel Flutter

To verify the solutions obtained in the high reduced-frequency range, one is required to apply the present BTM to the supersonic panel flutter problem for cylindrical shells. Previously, Dowell, and Widnall (Ref. 37) used Laplace transfer technique to study this problem, whereas Platzer et al. (Ref. 38) used the Linearized Method of Characteristics (LMOC). The objective of these studies is to evaluate the generalized forces acting on the vibrating cylindrical panel of an otherwise rigid, infinitely long, cylindrical shell.

Let L be the length of the cylindrical panel i.e. $(0 < x < L)$. Along the cylindrical shell, the oncoming flow upstream of the panel is uniformly supersonic. The cylindrical panel is allowed to perform small-amplitude harmonic oscillations (see Fig. 55).

For inviscid analysis of panel flutter, Eq. (6.3) ($G_3 = 0$) is the commonly used governing equation. On the mean surface of the cylindrical panel, r=R, the tangency condition reads:

$$\phi_{1r} = -ikh + h_x \quad , \quad 0 < x < L \qquad (7.16)$$
$$= 0 \quad , \quad x < 0$$

where h is the mode shape of the vibrating panel, defined as

$$h(x,\theta) = \sin(j\pi x)\cos(n\theta) \qquad (7.17)$$

The unsteady pressure coefficient C_p^1 on the panel surface is simply

$$C_p^1 = -2[\phi_{1x} + ik\phi_1] \tag{7.18}$$

and the generalized aerodynamic forces Q_{ij} reads

$$Q_{ij} = \frac{1}{2C} \int_0^{2\pi} \int_0^L C_p^{1(i)} \sin(j\pi x)\cos(n\theta) R \, d\theta \, dx \tag{7.19}$$

where $C_p^{1(i)}$ is the unsteady aerodynamic pressure due to the mode $\sin(i\pi x)\cos(n\theta)$ and $C = 2\pi$ for $n = 0$ and π for $n \neq 0$.

Bundled triplets are placed along the x-axis in the interval $-\beta R < \xi < L-\beta R$. The panel elements and control points between $0 < x < L$ and $0 < \theta < 2\pi$ on the mean surface are distributed according to the cosine law in both x and θ directions. Combining Eqs. (7.14), (7.16) and (7.17) results in the following tangency condition evaluated at the control points.

$$[V][LS]\{\phi_{i,m}\} = \{(ik \sin(j\pi x_i) + j\pi \cos(j\pi x_i))\cos(n\theta_m)\} \tag{7.20}$$

The potential values $\phi_{i,m}$ can now be obtained from the above equation. Thus, the unsteady pressure and the generalized forces can be evaluated according to Eqs. (7.18) and (7.19).

In the present formulation, the circumferential mode shape (i.e., the $\cos(n\theta)$ factor) is retained throughout the analysis, whereas Refs. 37 and 38, $\cos(n\theta)$ is factorized out in their formulation. As a result, the number of control points required in the circumferential direction increases rapidly with an increase in n, although the computation time is still

comparatively rapid. It is essential to point out that the present method is a full three dimensional one which can treat a much wider scope of problems than those in Refs. 37 and 38. Feasible applications in panel flutter using the present method include closed (pointed) bodies of circular or noncircular cross sections and vibrating panels of non-harmonic mode shapes (i.e., the case of partially oscillating shells).

7.6 Results and Discussion

To validate the present method, numerical examples in terms of steady pressures, stability derivatives, and generalized forces are presented for asymmetric bodies and for cylindrical panels.

7.6.1 Asymmetric Bodies

The steady pressure distributions for three different asymmetric conical bodies are presented in Figs. 51, 52 and 53 at the same freestream Mach number $M_\infty = 2.0$. Since the flowfields are conical, only the circumferential C_ps are presented for these cases. Asymmetric configurations as shown in Figs. 51 and 52 are placed at mean angle of attack $\alpha = 0$, whereas the elliptic cone in Figure 4 is at $\alpha = 5°$. Since the flow is symmetrical with respect to the meridian plane, pressures on half of the body are presented ($0 < \theta < 180°$). Because of the steeper variation in the given body curvature (due to cos 3θ), a bundle of 36 triplet lines is distributed in equal circumferential intervals for a full body in Fig. 51. The geometries in Figs. 52 and 53 are less complicated; only 18 triplet lines were used for full bodies in

both cases. It can be seen that the present computed results are in good agreement with Devan's results using the finite difference method (Ref. 35) and the USSAERO results (Ref. 2). Typically, we use 40 panels in the circumferential direction in the USSAERO program for obtaining results in Figs. 51, 52 and 53.

In the present method, 5 segments are used in the x direction. This amounts to a total of 100~200 panels and control points to be evaluated. Because the evaluation scheme of the present kernel is much simpler, the CPU time required is about one tenth of that needed in the USSAERO code.

Fig. 54 presents the static (Figs. 54a, 54b) and dynamic (Figs. 54c, 54d) normal force and moment coefficients at various Mach numbers for a family of elliptic cones placed at zero mean angle of attack. The ellipticity ratio as defined by a/b, ranges from .75 to 1.3. Figs. 54a and 54b compare the present results with those computed by USSAERO. There appears to be an increase in discrepancies as the elliptic cone becomes more wing-like, i.e., a/b > 1. When the ratio approaches one, all results converge to the results for a circular cone as obtained in Chapter 4.

Similarly, the computed results for the out-of-phase normal forces and moment coefficients (Figs. 54c and 54d) also converge to those obtained in Chapter 4 when a/b approaches one as expected. In passing, we note that little Mach dependency is observed for the static moments (about $x_G = 0$), whereas the damping moment decreases rapidly with increasing Mach number. Furthermore, all results confirm the expected trend that both the

static and the damping moments increase with decreasing ellipticity ratio, i.e., as the body becomes more wing-like.

7.6.2 Cylindrical Panel Flutter

In order to validate the present method in the high-frequency domain, supersonic cylindrical flutter cases (Fig. 55) are selected for comparison with existing theories (Refs 37 and 38).

A bundle of triplet lines are arranged according to a cosine distribution both in the circumferential and in the axial directions ($0 < \theta < 2\pi$ and $0 < x < 1$). The cylindrical panel is first evenly divided into n intervals in the circumferential direction, say n=5. Within each interval, eight control points are used, given a total of 40 control points. In the axial direction, 25 points are used for all n's.

The real and the imaginary parts of the generalized forces on the cylindrical panel are presented in Figs. 56 and 57 for the freestream Mach number $M_\infty = \sqrt{2}$ and the reduced frequencies k=0 and 1.0. The generalized forces are computed based on Eq. (7.19).

It is seen that good agreements are found between the present results and those of Dowell and Widnall (Ref. 37) and of Platzer et al. (Ref. 38) up to n=5 for both reduced frequencies (k=0 and 1.0).

7.6.3 Salient Features of BTM

It has been shown that the present method has the following features:

a. With the H-G model, the BTM is computationally efficient and robust for unsteady flow computations in the full frequency range.

b. Although the total number of panels needed for BTM is comparable to that of a surface panel method, the CPU time is only one tenth of the latter.

c. The BTM places the control points on the exact body surface whereas a surface panel method usually places the control points on the approximate surface.

CHAPTER 8

Body-Wing Combinations

8.1 Unsteady Lifting Surface Method

Previously, an effective panel method has been fully developed for oscillating lifting surfaces in supersonic flow HGM (Ref. 4). This analysis has been further extended from the velocity potential treatment to that of an acceleration potential one so that the regions of wake can be completely avoided in the calculation. For this reason, the acceleration potential version of the HGM (called AHGM) is most advantageous in coping with the unsteady problems for wing-body combinations, in that only the panels lying on the wing-body surfaces are needed to be accounted for.

According to AHGM, the normal velocity and the unknown linearized pressure can be related by the familiar expression, i.e.

$$\frac{\partial \phi_1}{\partial n}(x,y,z) = \int\int_A \Delta c_p \; K \; ds \tag{8.1}$$

where

$$K = e^{-i\mu(x-\xi)} \; \frac{\partial}{\partial \eta} \int \frac{\cos(\lambda \bar{R})}{\bar{R}} \; e^{-i\mu(x-\nu)} \, d\nu$$

$$\bar{R}^2 = (x - \nu)^2 - \beta^2 [(y - \eta)^2 + (z - \zeta)^2]$$

$$\Delta c_p = c_p{}^l - c_p{}^u$$

and S is the effective wing area enclosed by the intersections due to the inversed Mach code originated from the control point (x,y,z).

8.2 Body-Wing Formulation

The interference between the body and the wing is essentially provided by the flow tangency condition. In the case of the lifting surfaces, the pressure-normal velocity relation is the result of the tangency condition, i.e.

$$\int_W \Delta c_p K ds = v_N \tag{8.2}$$

in which v_N is the normal velocity, or the downwash on the lifting surface. In terms of the body influence and the given wing mode, v_N represents a difference between these two

$$v_N = B_w - (v_N)_B \tag{8.3}$$

where $(v_N)_B$ is the normal velocity induced by the presence of the body; as related to Eq. (7.1), $(v_N)_B = \frac{\partial \phi_1}{\partial n}$. The term B_w represents the wing mode. Thus, Eq. (8.2) becomes

$$(\int_W \Delta c_p K ds)_w + (\frac{\partial \phi_1}{\partial n})_w = B_w \quad , \text{ on the wing} \tag{8.4}$$

Note that in the RHS of Eq. (8.4), kernel K and $(\frac{\partial \phi_1}{\partial n})_w$ are evaluated on the lifting surfaces. Similarly, the relationship on the body can be derived, i.e.

$$\left(\frac{\partial \phi_{.}}{\partial n}\right)_B + \left(\int_W \Delta c_p K ds\right)_B = B_B \quad , \text{ on the body} \tag{8.5}$$

This time, the kernel K and $\left(\frac{\partial \phi_1}{\partial n}\right)_B$ are evaluated on the body surfaces.

With Eqs. (8.4) and (8.5), the body-wing tangency condition can be expressed in a matrix form,

$$\begin{bmatrix} \left(\frac{\partial E}{\partial n}\right)_{BB} & \left(\frac{\partial E}{\partial n}\right)_{Bw} \\ (K)_{wB} & (K)_{ww} \end{bmatrix} \begin{Bmatrix} \phi_B \\ \Delta c_{pw} \end{Bmatrix} = \begin{Bmatrix} B_B \\ B_w \end{Bmatrix} \tag{8.6}$$

where the kernel function $\left(\frac{\partial E}{\partial n}\right)$ is related to the least square matrix by the following equation

$$\left[\frac{\partial E}{\partial n}\right] = \{[u]\{n_x\} + [v]\{n_r\} + [w]\{n_\theta\}\} \cdot [LS] \tag{8.7}$$

n_x, n_r and n_θ are the directional consines of the body panels; B_B and B_w are the given body and wing modes respectively. Eq. (8.6) is solved to yield the Δc_p value on the wing. The velocities on the body can be evaluated at the control points from Eqs. (7.13, 7.14 and 7.15). Consequently, the pressure on the body can be determined from Eq. (6.18).

8.3 Pressure Coefficients

8.3.1 Unsteady Pressure Coefficient for the Body

Eq. (6.18) provides the explicit unsteady pressure formula in the cylindrical coordinate for an oscillating elastic body. For body-wing configurations, it is convenient to rewrite this expression in the Cartisien coordinate on the body surface.

$$C_p^1 = -2\,S_o \cdot \{(1+\phi_{ox})(\phi_{1x}-2z_B g''\phi_{ox}) + \phi_{oy}\phi_{1y} + \phi_{oz}\phi_{1z} + g'\phi_{oz} + ik(\phi_1 + \phi_{oz} g - z_B g'\phi_{ox})\} \quad (8.8)$$

where z_B is the control point location of the body panel and g is the given body mode.

8.3.2 Unsteady Pressure Coefficient for the Wing

Eq. (8.8) can be applied to account for the pressure on the lifting surface due to the body-wing interference, i.e.

$$\Delta c_p^1 = -2S_o \cdot \{\phi_{1x}(1+\phi_{ox}) + \phi_{1y}\phi_{oy} - \phi_{1z}\phi_{oz} + ik\phi_1\} \quad (8.9)$$

The steady velocities ϕ_{ox}, ϕ_{oy}, ϕ_{oz} and the S_o term are to be evaluated according to the effective body panels within the inversed Mach cone. Eq. (8.9) can be further simplified as

$$\Delta c_p^1 = -2S_o \cdot \{\phi_{1x} + ik\phi_1\} \quad (8.10)$$

since the second order terms in the bracket can be ignored. Further simplification of Eq. (8.10) results in the linearized pressure formula

$$\Delta c_p^1 = -2\,\{\phi_{1x} + ik\phi_1\} \quad (8.11)$$

which is essentially the pressure formula of the thin wing.

In passing, we note that to include the factor S_o might upgrade the accuracy in the higher Mach number range as it was previously noted by Van Dyke (Ref. 10).

8.4 Generalized Forces and Stability Derivatives

The generalized forces Q_{IJ} can be expressed in terms of the unsteady pressure coefficient c_p^1 and of the mode shape g as,

$$Q_{IJ} = \frac{1}{S_{ref}} \int \int_S C_p^{1(J)} (n_x g'^{(I)} z - g^{(I)} n_z) ds$$

where S is the wing plus the body surface area; n_x and n_z are the normal components in the x and z direction to the wing and body surfaces, respectively; z is the coordinate of the control point; $C_p^{1(J)}$ is the unsteady pressure coefficient due to the J-th mode; $g^{(I)}$ is the I-th mode of oscillation; and S_{ref} represents the maximum area or the based area for the body-alone cases, whereas it represents the wing planform area for the wing-body combination cases.

The stability derivatives are related to the generalized forces by the following formulae:

$$C_{L_\alpha} = R_e(Q_{12})$$

$$C_{m_\alpha} = \frac{R_e(Q_{22})}{L}$$

$$C_{N_{\dot{\alpha}}} + C_{N_q} = \frac{I_m(Q_{12})}{k}$$

$$C_{m_{\dot{\alpha}}} + C_{m_q} = \frac{I_m(Q_{22})}{kL}$$

where L is the body length for body alone cases, and the wing mean chord for body-wing combination cases; k in this instance is the reduced frequency based on L. Q_{12} and Q_{22} are the 12 and 22 components of the generalized force matrix representing two

rigid-body modes. The former is the plunging mode and the latter the pitching mode.

8.5 Results and Discussion

To verify the present results for wing-body combinations in the low-frequency limit, measured stability derivatives in Refs. 44 and 45 are selected for comparison. Two configurations are selected as shown in Fig. 58:

Case A: Aspect Ratio AR = 3.0, Triangular Wing-Body

Case B: Aspect Ratio AR = 3.0, Swept Wing-Body

To compute the stability derivatives for these configurations, a bundle of 20 triplet lines is used for the body. With 10 segments along the body axis, this amounts to 200 control points on the body surface. However, only 50 panels are required for modeling the wings.

Figs. 59 and 60 show the computed static and damping moments for the wing-body configurations in Cases A and B respectively. Good agreements are found between the present results and the measured data in the overall Mach number ranges at two pitching-axis locations, x_G = .25c and .35c (c is the chord length). For damping moment calculations, one notices that the predicted results of the analytical theory (Ref. 46) deviate further from the measured data than the present results. This is due to the fact that an analytical solution of a rectangular wing is used to approximate that of a delta and a swept wing planforms.

CHAPTER 9

CONCLUSION

Several unsteady supersonic methods have been developed for computation of unsteady aerodynamics for elastic bodies of revolution, asymmetric bodies and body-wing configurations. These methods include the Harmonic Potential Panel (HPP) method, the Bundle Triplet Method (BTM) and the combined method of BTM and Harmonic Gradient Method (HGM) for body-wing combinations. All methods are based on the Harmonic-Gradient (H-G) model in order to obtain accurate solutions in the full frequency domain and the lower Mach number range. Specific conclusions of the present development can be summarized as follows:

1. For bodies of revolution in oscillation the proper choice of the coordinate system has been subject to some controversy in the past. The formulation in the wind-fixed, body-fixed, and the pseudo-wind-fixed systems are presented. The solutions of the linearized equation in the wind-fixed system, and of the first-order equation in the body-fixed and the pseudo-wind-fixed systems are compared for a cone in rigid and bending oscillations. It is shown that when the wind-fixed system is used in a straight forward manner a singularity appears at the body apex and contaminates the solution downstream.

2. Further investigation of this problem shows that such apex singularities also appear in the body-fixed system if the linearized equation instead of the first order is solved. Also it is shown that the origin is due to the use of cylindrical

coordinates. When the problem is correctly formulated in a conical coordinate system the pressure coefficient is shown to remain regular at the body apex (see Appendix C).

3. The computational procedure for the mean flow has been developed for both the linear and nonlinear potential equations. Unlike the unsteady computation procedure for wing planforms, the steady mean flow solution enters into the boundary conditions and pressure coefficient for the unsteady flow. Hence, it is important to investigate the influence of the steady mean flow upon the unsteady pressures as well as the flutter boundaries. We believe that it is the first time that nonlinear effects have been included in an unsteady panel method. Computed steady pressures and stability derivatives using the present nonlinear method are found to agree well with the known results. Unsteady nonlinear results show that the influence of the mean flow nonlinearity is important. For a slender body, nonlinear effects become more apparent in the high Mach number range. Our unsteady nonlinear results are in better correlation with measured data and unsteady exact theories than all other results using different methods.

4. For a cone in plunging and pitching oscillations the flutter boundaries, as determined by the linear and nonlinear methods, are compared to those obtained by experiment and other theories in Figs. 33 and 34. With reference to the measured data, all of the computed flutter boundaries are conservative predictions. The computed boundaries become more conservative in the order of present nonlinear method, present linear method and

slender body theory. By contrast, all results as predicted by previous theories failed to provide a conservative flutter boundary.

5. The aerodynamic damping coefficient of a cone-cylinder in the first two free-free bending modes of oscillation and of the Saturn SA-1 model in the first free-free bending mode of oscillation are compared to those obtained by experiment and other theories in Figs. 29 and 31. For both configurations all the computed results establish close trends in the measured data. By contrast, all results as predicted by previous theories are in considerable discrepancy. For both configurations the aerodynamic damping is found positive, and therefore it provides stabilizing effects within the Mach number range considered.

6. With the H-G model, the BTM is computationally efficient and robust for unsteady flow computations in the full frequency range.

7. Although the total number of panels needed for BTM is comparable to that of a surface panel method, the CPU time is only one tenth of the latter.

8. The BTM places the control points on the exact body surface whereas a surface panel method usually places the control points on the approximate surface.

9. To validate the present method, numerical examples have been studied for various three-dimensional configurations. These include: steady pressures on three asymmetric conical bodies, generalized forces for cylinderical panel flutter and stability derivatives for bodies and wing-body combinations. It is found

that all computed results are in good agreement with existing theoretical results and measured data.

10. The combined use of the developed AHGM and the BTM allows the wing-body surface to be the only computed domain. Moreover, the body-wing formulation can directly yield the unsteady pressure on wing planforms. Hence, the present computation procedure clearly leads to the development of a user-friendly program code.

Finally, we conclude that all methods proposed have been thoroughly validated with existing theories or measured data. It is believed that all methods developed thus far can become effective tools for supersonic aeroelastic applications to realistic configurations.

Throughout three phases of this development, most of our work has been presented in the AIAA meetings as well as appeared in various kinds of AIAA Journals, (See Refs. 47 to 54). For technology transfer, one report along with the developed program code has been forwarded to Army Missile Command (MICOM) in Huntsville, Alabama in 1986 (Ref. 55).

APPENDIX A

LINEARIZED EQUATIONS IN THE BODY-FIXED COORDINATE SYSTEM

APPENDIX A

The body-fixed coordinate system can be related to the wind-fixed coordinate system of Fig. 3 by the following transformation

$$x = x' - \frac{\partial h}{\partial x'}(x',t')\, z' \qquad (A.1)$$

$$y = y'$$

$$z = z' + h(x',t')$$

where $h(x',t')$ is the instantaneous normal displacement of the body and only linear terms in h are retained since it is assumed to be small.

The operators ∇, ∇^2 and $\nabla\cdot$ of Eqs. (2.2) and (2.3) in curvilinear coordinates are given by (see Ref. 39)

$$\nabla\psi = \frac{1}{h_1}\frac{\partial\psi}{\partial q_1}\vec{a}_1 + \frac{1}{h_2}\frac{\partial\psi}{\partial q_2}\vec{a}_2 + \frac{1}{h_3}\frac{\partial\psi}{\partial q_3}\vec{a}_3 \qquad (A.2)$$

$$\nabla\cdot A = \frac{1}{h_1 h_2 h_3}\left[\frac{\partial}{\partial q_1}(h_2 h_3 A_1) + \frac{\partial}{\partial q_2}(h_3 h_1 A_2) + \frac{\partial}{\partial q_3}(h_1 h_2 A_3)\right] \qquad (A.3)$$

and

$$\nabla^2\psi = \frac{1}{h_1 h_2 h_3}\left[\frac{\partial}{\partial q_1}\left(\frac{h_2 h_3}{h_1}\frac{\partial\psi}{\partial q_1}\right) + \frac{\partial}{\partial q_2}\left(\frac{h_3 h_1}{h_2}\frac{\partial\psi}{\partial q_2}\right) + \frac{\partial}{\partial q_3}\left(\frac{h_1 h_2}{h_3}\frac{\partial\psi}{\partial q_3}\right)\right] \qquad (A.4)$$

where q_1, q_2 and q_3 are the curvilinear coordinates, $\vec{a}_1$, $\vec{a}_2$, and a_3 are unit vectors along these coordinates, h_1, h_2 and h_3 are the matrix coefficients defined as

$$h_i^2 = \left(\frac{\partial x'}{\partial q_i}\right)^2 + \left(\frac{\partial y'}{\partial q_i}\right)^2 + \left(\frac{\partial z'}{\partial q_i}\right)^2 \qquad (A.5)$$

and x', y' and z' are the cartesian coordinates.

In the present case

$$\left.\begin{aligned} h_1 &= 1 + \frac{\partial^2 h}{\partial x^2} z \\ h_2 &= 1 \\ h_3 &= 1 \end{aligned}\right\} \qquad (A.6)$$

where the nonlinear terms in h(x,t) have been neglected.

The total potential Ω in the body-fixed coordinate system can then be expressed as

$$\Omega(x,y,z,t) = x + h_x(x,t)z + \Phi(x,y,z,t) \qquad (A.7)$$

where $\Phi(x,y,z,t)$ is the perturbation potential. From Eqs. (A.2), (A.4) and (A.6) and retaining only linear terms in h we obtain

$$\nabla\Omega = (1 + \Phi_x - h_{xx}z\Phi_x)\, e_x + \Phi_y e_y + (h_x + \Phi_z)e_z \qquad (A.8)$$

$$\nabla^2\Omega = h_{xxx}z + \Phi_{xx} - 2h_{xx}z\Phi_{xx} - h_{xxx}z - h_{xxx}z\Phi_x + \Phi_{yy} + h_{xx}\Phi_z + \Phi_{zz} \qquad (A.9)$$

The time derivative in Eqs. (2.2) and (2.3) in the body-fixed system is given by

$$\begin{aligned} \frac{\partial}{\partial t'} &= \frac{\partial}{\partial t} + \frac{\partial x}{\partial t'}\frac{\partial}{\partial x} + \frac{\partial z}{\partial t'}\frac{\partial}{\partial z} \\ &= \frac{\partial}{\partial t} - h_{xt}\, z \frac{\partial}{\partial x} + h_t \frac{\partial}{\partial z} \end{aligned} \qquad (A.10)$$

Therefore

$$\frac{\partial \Omega}{\partial t'} = h_{xt}\, z + \Phi_t - h_{xt} z(1 + \Phi_x) + h_t \Phi_z \qquad (A.11)$$

$$\frac{\partial^2 \Omega}{\partial t'^2} = h_{xtt} z + \Phi_{tt} - h_{xtt} z(1 + \Phi_x) - h_{xt} z \Phi_{xt} + h_{tt} \Phi_z + h_t \Phi_{zt} \qquad (A.12)$$

We can now compute all the terms of Eqs. (2.2) and (2.3) in the body-fixed coordinate system. If only linear terms in Φ are retained the following linear equation is obtained

$$\begin{aligned} &\Phi_{xx} - 2h_{xx} z \Phi_{xx} - h_{xxx} z \Phi_x + \Phi_{yy} + h_{xx} \Phi_z + \Phi_{zz} \\ &= M_\infty^2 \big[\Phi_{tt} - h_{xtt} z \Phi_x - h_{xt} z \Phi_{xt} + h_{tt} \Phi_z + h_t \Phi_{zt} \\ &\quad + 2\Phi_{xt} - 2h_{xxt} z \Phi_x - 2h_{xx} z \Phi_{xt} + 2h_{xt} \Phi_z + 2h_x \Phi_{zt} \\ &\quad - 2h_{xt} z \Phi_{xx} + 2h_t \Phi_{xz} + \Phi_{xx}(1 - 2h_{xx} z) - h_{xxx} z \Phi_x \\ &\quad + h_{xx} \Phi_z + 2h_x \Phi_{xz} \big] \end{aligned} \qquad (A.13)$$

Now, letting $h(x,t) = g(x)\delta(t) = \delta_0 e^{ikt} g(x)$, and $\Phi(x,y,z,t) = \phi_0(x,y,z) + \delta_0 e^{ikt} \phi_1(x,y,z)$, with $\delta_0 \ll 1$, and substituting these into Eq. (A.13) yields the following equations:

$$(1 - M_\infty^2)\phi_{0xx} + \phi_{0yy} + \phi_{0zz} = 0 \qquad (A.14)$$

for order of one and,

$$(1-M_\infty^2)\,\phi_{1xx} + \phi_{1yy} + \phi_{1zz} - 2ikM_\infty^2\phi_{1x} + k^2M_\infty^2\phi_1$$

$$= M_\infty^2\left[k^2g'z\phi_{0x} - k^2g\phi_{0z} - 2ikg''z\phi_{0x} + 2g'ik\phi_{0z}\right.$$

$$- 2g'ikz\phi_{0xx} + 2gik\phi_{0xz} - g'''z\phi_{0x} - 2g''z\phi_{0xx} + g''\phi_{0z}$$

$$\left. + 2g'\phi_{0xz}\right] - g''\phi_{0z} + 2g''z\phi_{0xx} + g'''z\phi_{0x} \qquad (A.15)$$

for order of δ_0.

In cylindrical coordinates Eqs. (A.14) and (A.15) become

$$(1-M_\infty^2)\,\phi_{0xx} + \phi_{0rr} + \frac{1}{r}\,\phi_{0r} + \frac{1}{r^2}\,\phi_{0\theta\theta} = 0 \qquad (A.16)$$

$$(1-M_\infty^2)\,\phi_{1xx} + \phi_{1rr} + \frac{1}{r}\,\phi_{1r} - \frac{1}{r^2}\,\phi_{1\theta\theta} - 2ikM_\infty^2\phi_{1x} + k^2M_\infty^2\phi_1$$

$$= M_\infty^2\left\{\left(k^2g'r\phi_{0x} - k^2g\phi_{0r} - 2ikg''r\phi_{0x} + 2g'ik\phi_{0r}\right.\right.$$

$$- 2g'ikr\phi_{0xx} + 2gik\phi_{0xr} - g'''r\phi_{0x} - 2g''r\phi_{0xx}$$

$$\left.\left. + g''\phi_{0r} + 2g'\phi_{0xr}\right)\cos\theta + \left(k^2g\phi_{0\theta} - 2g'ik\phi_{0\theta}\right.\right.$$

$$\left.\left. - 2gik\phi_{0x\theta} - g''\phi_{0\theta} - 2g'\phi_{0x\theta}\right)\frac{1}{r}\sin\theta\right\}$$

$$- g''\left(\phi_{0r}\cos\theta - \frac{1}{r}\,\phi_{0\theta}\sin\theta\right) + 2g''r\phi_{0xx}\cos\theta$$

$$+ 2g'''r\phi_{0x}\cos\theta \qquad (A.17)$$

For a body of revolution the mean flow potential ϕ_0 is independent of θ, and the cross flow potential can be expressed as $\phi_1(x,r,\theta) = \phi_1(x,r)\cos\theta$. Thus Eqs. (A.16) and (A.17) become

$$(1-M_\infty^2)\,\phi_{0xx} + \phi_{0rr} + \frac{1}{r}\,\phi_{0r} = 0 \qquad (A.18)$$

$$
\begin{aligned}
(1-M_\infty^2)\,\phi_{1xx} + \phi_{1rr} + \frac{1}{r}\,\phi_{1r} - \frac{1}{r^2}\,\phi_1 - 2ikM_\infty^2\phi_{1x} + k^2M_\infty^2\phi_1 \\
= M_\infty^2\big[k^2g'r\phi_{0x} - k^2g\phi_{0r} - 2ikg''r\phi_{0x} + 2g'ik\phi_{0r} \\
- 2g'ikr\phi_{0xx} + 2gik\phi_{0xr} - g'''r\phi_{0x} - 2g''r\phi_{0xx} \\
+ g''\phi_{0r} + 2g'\phi_{0xr}\big] \\
+ 2g''r\phi_{0xx} + g'''r\phi_{0x} - g''\phi_{0r} \qquad \text{(A.19)}
\end{aligned}
$$

APPENDIX B

EVALUATION OF THE UNSTEADY POTENTIAL AND VELOCITIES APPLYING THE HARMONIC GRADIENT MODEL

APPENDIX B

The integral solution of the homogeneous unsteady wave equation, i.e. Eq. (2.8) reads

$$\phi_1(x,r) = -\frac{1}{2\pi}\int_0^{x-\beta r} F(\xi)\,\frac{\partial}{\partial r}\,K(x-\xi,\beta r)\,d\xi \qquad (B.1)$$

where the kernel function K, as defined in Eq. (4.2) is given by

$$K(x-\xi,\beta r) = e^{-i\mu(x-\xi)}\,\frac{\cos\lambda R}{R} \qquad (B.2)$$

where $R=\sqrt{(x-\xi)^2-\beta^2 r^2}$, $\mu = kM_\infty^2/\beta^2$, $\lambda = kM_\infty/\beta^2$

and $F(\xi)$ is the dipole strength. The value of $F(\xi)$ at $\xi=0$ is zero in order to satisfy the Mach wave condition.

For integration of Eq. (B.1) it is convenient to use the relative distance $x-\xi$ as the independent variable instead of ξ. Hence, we define $x_0 = x - \xi$ and $d\xi = - dx_0$

where at $\xi = 0$, $x_0 = x$

and at $\xi = x - \beta r$, $x_0 = \beta r$

and Eq. (B.1) becomes

$$\phi_1(x,r) = \frac{1}{2\pi}\int_x^{\beta r} F(x-x_0)\,e^{-i\mu x_0}\,\frac{\partial}{\partial r}\left(\frac{\cos\lambda R_0}{R_0}\right)dx_0 \qquad (B.3)$$

where $R_0 = \sqrt{x^2{}_0-\beta^2 r^2}$.

Integrating Eq. (B.3) by parts and applying the Mach wave condition at $x-\beta r=0$, we obtain

$$\phi_1(x,r) = \frac{1}{2\pi}\left[F(x-x_0)e^{-i\mu x_0}\ \frac{\partial}{\partial r}S(x_0,\beta r)\ \Big|_x^{\beta r}\right.$$

$$\left. - \int_x^{\beta r} \frac{\partial}{\partial x_0}[F(x-x_0)e^{-i\mu x_0}]\ \frac{\partial}{\partial r}S(x_0,\beta r)dx_0\right] \quad (B.4)$$

where $S(x_0,\beta r) = \int_{\beta r}^{x_0} \frac{\cos\lambda\sqrt{\tau^2-\beta^2r^2}}{\sqrt{\tau^2-\beta^2r^2}}d\tau$.

The first term of Eq. (B.4) is zero at the upper and the lower limits since $F(0)=0$ for a pointed body and $S(\beta r,\beta r)=0$ along the apex Mach wave. Consequently, $\phi_1(x,r)$ can be expressed as

$$\phi_1(x,r) = -\frac{1}{2\pi}\int_x^{\beta r} \frac{\partial}{\partial x_0}[F(x-x_0)\ e^{-i\mu x_0}]\ \frac{\partial}{\partial r}S(x_0,\beta r)dx_0 \quad (B.5)$$

As discussed in Section 4.2, to solve for Eq. (B.5) the dipole strength function is discretized into elements along the body axis and the potential is evaluated at the discrete field points (x_j, r_j).

$$\phi_1(x_j,r_j) = -\frac{1}{2\pi}\sum_{i=1}^{j}\int_{x_j-\xi_i}^{x_j-\xi_{i+1}}\frac{\partial}{\partial x_0}\ [F_i(x_j-x_0)e^{-i\mu x_0}]$$

$$\frac{\partial}{\partial r_j}\ S(x_0,\beta r_j)dx_0 \quad (B.6)$$

where $\xi_1=0$ and $\xi_{j+1}=x_j-\beta r_j$.

Introducing the Harmonic Gradient model (as discussed in Section 4.2),

$$\frac{\partial}{\partial x_0}[F_i(x_j-x_0)e^{-i\mu x_0}] = [a_i(x_j-x_0) + b_i]e^{-i\mu x_0} \quad (B.7)$$

Eq. (B.7) amounts to stating that the dipole strength is

$$F_i(x_j-x_0) = \left(\frac{b_i}{i\mu} + \frac{a_i}{\mu^2}\right)\left(e^{-i\mu(x_j-x_0)} - 1\right) - \frac{a_i}{i\mu}(x_j-x_0) \quad (B.8)$$

In the limit of $k\to 0$ (or $\mu\to 0$), Eq. (B.8) is reduced to

$$F_i(x_j-x_0) = -\frac{a_i}{2}(x_j-x_0)^2 - b_i(x_j-x_0) \quad (B.9)$$

Now, the doublet strength model as given by Eq. (B.9) is the same as the one used by Tsien[39] for the steady angle of attack case.

Substituting Eq. (B.7) into (B.6) yields

$$\phi_1(x_j,r_j) = -\frac{1}{2\pi}\sum_{i=1}^{j}\int_{x_j-\xi_i}^{x_j-\xi_{i+1}}[a_i(x_j-x_0)+b_i]e^{-i\mu x_0}\frac{\partial}{\partial r_j}S(x_0,\beta r_j)\,dx_0 \quad (B.9)$$

In order to determine $S(x_0,\beta r_j)$ it is convenient to apply the following transformation:

Let $\tau=\beta r_j\cosh\sigma$, and hence $d\tau=\beta r_j\sinh\sigma\,d\sigma$

where at $\tau=\beta r_j$, $\sigma=0$

and $\tau=x_0$, $\sigma=\cosh^{-1}\frac{x_0}{\beta r_j}$

$$\frac{\partial}{\partial r_j}S(x_0,\beta r_j) = \frac{\partial}{\partial r_j}\int_0^{\cosh^{-1}x_0/\beta r_j}\cos(\lambda\beta r_j\sinh\sigma)\,d\sigma.$$

By applying Leibnitz's rule,

$$\frac{\partial}{\partial r_j} S(x_0, \beta r_j) = - \frac{x_0 \cos(\lambda \sqrt{x_0^2 - \beta^2 r_j^2})}{r_j \sqrt{x_0^2 - \beta^2 r_j^2}}$$

$$- \int_0^{\cosh^{-1} x_0/\beta r_j} \lambda\beta \sinh\sigma \sin(\lambda\beta r_j \sinh\sigma) d\sigma \qquad (B.10)$$

Now a second transformation is introduced:

Let $\sinh\sigma = u$, hence $d\sigma = \frac{du}{\sqrt{1+u^2}}$

where at $\sigma = 0$, $u = 0$

and $\sigma = \cosh^{-1} \frac{x_0}{\beta r_j}$ $u = \sinh(\cosh^{-1}(\frac{x_0}{\beta r_j}))$.

The integral term of Eq. (B.10) now becomes

$$\int_0^{\sinh[\cosh^{-1}(\frac{x_0}{\beta r_j})]} \lambda\beta \frac{u}{\sqrt{u^2+1}} \sin(\lambda\beta r_j u) du.$$

Using Lashka's[27] exponential series substitution, namely

$$\frac{u}{\sqrt{1+u^2}} \simeq 1 - \sum_{n=1}^{N} a_n e^{-nc u} .$$

where the constant "c" and the coefficients "a_n" can be found in Ref. 27. Letting $x_0 = \beta r_j \cosh\tau$, and integrating Eq. (B.10) term by term yields

$$\frac{\partial}{\partial r_j} S(\tau, \beta r_j) = -\frac{\cosh\tau \cos(\lambda\beta r_j \sinh\tau)}{r_j \sinh\tau} + \frac{\cos(\lambda\beta r_j \sinh\tau)}{\lambda\beta r_j}\lambda\beta$$

$$+ \sum_{n=1}^{N} \frac{a_n e^{-nc\sinh\tau}\lambda\beta}{(\lambda\beta r_j)^2 + n^2 c^2}$$

$$[-n\ c\ \sin(\lambda\beta r_j \sinh\tau) - \lambda\beta r_j \cos(\lambda\beta r_j \sinh\tau)]$$

$$- \frac{\lambda\beta}{\lambda\beta r_j} - \sum_{n=1}^{N} \frac{a_n(-\lambda\beta r_j)\lambda\beta}{(\lambda\beta r_j)^2 + n^2 c^2} \qquad \text{(B.11)}$$

By substitution of Eq. (B.11) into Eq. (B.9) we obtain

$$\phi_1(x_j, r_j) = -\frac{1}{2\pi} \sum_{i=1}^{j} \int_{\cosh^{-1}\left(\frac{x_j - \xi_i}{\beta r_j}\right)}^{\cosh^{-1}\left(\frac{x_j - \xi_{i+1}}{\beta r_j}\right)} [a_i(x_j - \beta r_j \cosh\tau) + b_i]$$

$$e^{-i\mu\beta r_j \cosh\tau} \left\{-\beta \cosh\tau \cos(\lambda\beta r_j \sinh\tau)\right.$$

$$+ \sinh\tau\ \beta\Big[-1 + \cos(\lambda\beta r_j \sinh\tau)$$

$$+ \sum_{n=1}^{N} \frac{a_n e^{-nc\sinh\tau}}{(\lambda\beta r_j)^2 + (nc)^2} [-n\ c\ \sin(\lambda\beta r_j \sinh\tau)$$

$$\left.-\lambda\beta r_j \cos(\lambda\beta r_j \sinh\tau)]\beta r_j \lambda - \sum_{n=1}^{N} \frac{a_n(-\lambda^2\beta^2 r_j^2)}{(\lambda\beta r_j)^2 + (nc)^2}\Big]\right\} d\tau$$

(B.12)

Since all the terms of the integrand in Eq. (B.12) are regular, they can be integrated numerically by using a Gaussian quadrature formula.

The velocities in the x and r directions are determined by taking the derivative with respect to x and r in Eq. (B.3).

After the derivatives are taken the dipole strength function is discretized and the Harmonic Gradient model applied.

The x-component of the velocity can be expressed

$$\frac{\partial}{\partial x_j}\phi_1(x_j, r_j) = -\frac{1}{2\pi}\sum_{i=1}^{j}\int_{\cosh^{-1}\left(\frac{x_j-\xi_i}{\beta r_j}\right)}^{\cosh^{-1}\left(\frac{x_j-\xi_{i+1}}{\beta r_j}\right)} a_i e^{-i\mu\beta r_j\cosh\tau}$$

$$\left\{-\beta\cosh\tau\cos(\lambda\beta r_j\sinh\tau) + \beta\sinh\tau\right.$$

$$\left[-1 + \cos(\lambda\beta r_j\sinh\tau) + \sum_{n=1}^{N}\frac{a_n e^{-nc\sinh\tau}}{(\lambda\beta r_j)^2+(nc)^2}\right.$$

$$[-nc\sin(\lambda\beta r_j\sinh\tau) - \lambda\beta r_j\cos(\lambda\beta r_j\sinh\tau)]\beta r_j\lambda$$

$$\left.\left.-\sum_{n=1}^{N}\frac{a_n(-\lambda^2\beta^2 r_j^2)}{(\lambda\beta r_j)^2+(nc)^2}\right]\right\}d\tau \qquad (B.13)$$

Again Eq. (B.13) can be integrated numerically by using Gaussian quadrature since all the terms are regular.

The r component of the velocity becomes

$$\frac{\partial}{\partial r_j}\phi_1(x_j, r_j) = -\frac{1}{2\pi}\sum_{i=1}^{j}\int_{x_j-\xi_i}^{x_j-\xi_{i+1}}[a_i(x_j-x_0)+b_i]e^{-i\mu x_0}$$

$$\frac{\partial}{\partial r_j^2}S(x_0, \beta r_j)dx_0 \qquad (B.14)$$

next, letting $x_0 = \beta r_j\cosh\tau$ and applying the differentiation with respect to r_j, to Eq. (B.10) yields

$$\frac{\partial^2}{\partial r_j^2}S(\tau,\beta r_j) = -\frac{\partial}{\partial r_j}\frac{\cosh\tau\,\cos(\lambda\beta r_j\sinh\tau)}{r_j\sinh\tau}$$

$$-\frac{\partial}{\partial r_j}\int_0^\tau \lambda\beta\sinh\sigma\,\sin(\lambda\beta r_j\sinh\sigma)d\sigma$$

$$=\frac{\cosh\tau\,\cos(\lambda\beta r_j\sinh\tau)}{r_j^2\sinh\tau}$$

$$+\frac{\cosh\tau\,\lambda\beta\,\sin(\lambda\beta r_j\sinh\tau)}{r_j}$$

$$-\int_0^\tau \lambda^2\beta^2\sinh^2\sigma\sin(\lambda\beta r_j\sinh\sigma)d\sigma \qquad (B.15)$$

When the transformation $\sinh\sigma=u$ is introduced, the integral term of Eq. (B.15) becomes

$$\int_0^{\sinh\tau}\lambda^2\beta^2\,\frac{u^2}{\sqrt{1+u^2}}\sin(\lambda\beta r_j u)du$$

Again, when Lashka's exponential series substitution is used this integral becomes

$$\lambda^2\beta^2\,\frac{\beta r_j\sinh\tau}{\lambda(\beta r_j)^2}\sin(\lambda\beta r_j\sinh\tau)+\frac{\cos(\lambda\beta r_j\sinh\tau)}{\lambda^2\beta^2 r_j^2}\lambda^2\beta^2$$

$$-\lambda^2\beta^2\sum_{n=1}^{N}\frac{a_n e^{-nc\sinh\tau}}{(\lambda\beta r_j)^2+(nc)^2}\Big[\sinh\tau(-n\,c\,\cos(\lambda\beta r_j\sinh\tau))$$

$$+\lambda\beta r_j\sin(\lambda\beta r_j\sinh\tau)\Big]-\frac{\lambda^2\beta^2}{(nc)^2+(\lambda\beta r_j)^2}\Big[((nc)^2-(\lambda\beta r_j)^2)$$

$$\cos(\lambda\beta r_j\sinh\tau)-2\,n\,c\,\lambda\beta r_j\sin(\lambda\beta r_j\sinh\tau)\Big]$$

$$-\frac{\lambda^2\beta^2}{\lambda^2\beta^2 r_j^2}-\sum_{n=1}^{N}\frac{\lambda^2\beta^2 a_n((nc)^2-(\lambda\beta r_j)^2)}{((nc)^2+(\lambda\beta r_j)^2)^2} \qquad (B.16)$$

With Eq. (B.16), $\frac{\partial^2 S}{\partial r_j^2}$ of Eq. (B.15) can now be expressed in

a series form, i.e.,

$$\frac{\partial^2}{\partial r_j^2}S(\tau,\beta r_j) = \frac{\cosh\tau\ \cos(\lambda\beta r_j\sinh\tau)}{r_j^2\sinh\tau} + \frac{\lambda\beta\ \cosh\tau\ \sin(\lambda\beta r_j\sinh\tau)}{r_j}$$

$$- \frac{\lambda\beta\sinh\tau}{r_j}\sin(\lambda\beta r_j\sinh\tau) - \frac{\cos(\lambda\beta r_j\sinh\tau)}{r_j^2}$$

$$+ \lambda^2\beta^2 \sum_{n=1}^{N} \frac{a_n e^{-nc\sinh\tau}}{(\lambda\beta r_j)^2+(nc)^2}$$

$$\left[\sinh\tau(-n\ c\ \cos(\lambda\beta r_j\sinh\tau)+\lambda\beta r_j\sin(\lambda\beta r_j\sinh\tau)\right]$$

$$+ \frac{\lambda^2\beta^2}{(nc)^2+(\lambda\beta r_j)^2}[((nc)^2-(\lambda\beta r_j)^2)\cos(\lambda\beta r_j\sinh\tau)$$

$$- 2\ n\ c\ \lambda\beta r_j\sin(\lambda\beta r_j\sinh\tau)] - \frac{1}{r_j^2}$$

$$- \sum_{n=1}^{N} \frac{\lambda^2\beta^2 a_n((nc)^2-(\lambda\beta r_j)^2)}{((nc)^2+(\lambda\beta r_j)^2)^2} \qquad \text{(B.17)}$$

Finally where Eq. (B.17) is substituted into Eq. (B.14) and after some arrangement, we obtain

$$\frac{\partial}{\partial r_j}\phi_i(x_j,r_j) = -\frac{1}{2\pi}\sum_{i=1}^{j}\int_{\cosh^{-1}\left(\frac{x_j-\xi_i}{\beta r_j}\right)}^{\cosh^{-1}\left(\frac{x_j-\xi_{i+1}}{\beta r_j}\right)} [a_i(x_j-\beta r_j\cosh\tau)+b_i]$$

$$e^{-i\mu\beta r_j\cosh\tau}\ \beta\left\{\frac{\cosh\tau}{r_j}\cos(\lambda\beta r_j\sinh\tau)\right.$$

$$+ \lambda\beta\ \cosh\tau\ \sinh\tau\sin(\lambda\beta r_j\sinh\tau)$$

$$- \lambda\beta\ \sinh^2\tau\ \sin(\lambda\beta r_j\sinh\tau) - \frac{\sinh\tau}{r_j}$$

$$\cos(\lambda\beta r_j\sinh\tau) + \lambda^2\beta^2 r_j\sinh\tau$$

$$\sum_{n=1}^{N} \frac{a_n e^{-nc\sinh\tau}}{(\lambda\beta r_j)^2+(nc)^2} \left[\sinh\tau(-n\ c\ \cos(\lambda\beta r_j \sinh\tau)\right.$$

$$+ \lambda\beta r_j \sin(\lambda\beta r_j \sinh\tau)] + \frac{\lambda^2\beta^2 r_j \sinh\tau}{(nc)^2+(\lambda\beta r_j)^2}$$

$$[((nc)^2-(\lambda\beta r_j)^2)\cos(\lambda\beta r_j \sinh\tau)$$

$$\left. - 2\ n\ c\ \lambda\beta r_j \sin(\lambda\beta r_j \sinh\tau)]\right\}\ d\tau \qquad (B.18)$$

All the terms in Eq. (B.18) are regular and can be integrated numerically by a Gaussian quadrature.

APPENDIX C

ON THE APEX SINGULARITY FOR OSCILLATING POINTED BODIES: WIND-FIXED VERSUS BODY-FIXED COORDINATE SYSTEMS

APPENDIX C

It has been known for some time (see Refs. 17, 41, 42) that, in the cross flow potential for an oscillating body in the wind-fixed coordinates system, a singularity at the apex arises. The origin of this singularity is the second-order derivatives of the mean flow that appear in the boundary conditions and unsteady pressure coefficient when these are evaluated at the mean position of the body surface. For a body in rigid oscillation with respect to x_G the tangency condition and the unsteady pressure coefficient are respectively given by

$$\phi_{1r} - R'\phi_{1x} = 1 - \phi_{0x} + (x-x_G)(\phi_{0rr} - R'\phi_{0xr} - ik) + (x-x_G)(\phi_{0rr} - R'\phi_{0xr} - ik) \quad \text{at } r=R(x) \quad (C.1)$$

$$C_p^1 = 1 - 2S_0[(1 + \phi_{0x})\phi_{1x} + \phi_{0r}\phi_{1r} + ik\phi_1 - (x-x_G)(\phi_{0xr}(1 + \phi_{0x}) + \phi_{0rr}\phi_{0r})] \quad \text{at } r=R(x) \quad (C.2)$$

where $S_0 = [1 - \frac{\gamma-1}{2} M_\infty^2(2\phi_{0x} + \phi_{0x}^2 + \phi_{0x}^2)]^{1/\gamma-1}$, k is the reduced frequency, ϕ_0 the mean flow potential and ϕ_1 the unsteady flow potential. The second-order derivatives of ϕ_0 can be better shown to be singular from slender body theory. The velocity ϕ_{0r} in the slender body theory (Ref. 5) is given by $\phi_{0r} = \frac{RR'}{r}$, and its derivatives with respect to x and r by

$$\phi_{0rx} = \frac{R'^2 + RR''}{r} \text{ and } \phi_{0rr} = -\frac{RR'}{r^2} \quad (C.3)$$

On the body apex these terms behave like $\frac{R'(0)}{R(0)}$; therefore for a nonvanishing R'(0) they are singular.

In the body-fixed coordinate system the singularity at the apex has passed usually unnoticed because the first-order equation instead of the linearized one has been solved in this system and then the second-order derivative terms do not appear in the formulation.

For a body in rigid oscillation with respect to x_j the complete formulation in the body-fixed system is given by:

Governing equation;

$$(1-M_\infty^2)\,\phi_{1xx} + \phi_{1rr} + \frac{1}{r}\,\phi_{1r} - \frac{1}{r^2}\,\phi_1 + k^2M_\infty^2\phi_1 - 2ikM_\infty^2\phi_{1x}$$

$$= M_\infty^2[k^2(r\phi_{0x}-(x-x_G)\phi_{0r}) + 2ik(\phi_{0r}-r\phi_{0xx} + (x-x_G)\phi_{0xr})$$

$$+ 2\phi_{0xr}] \qquad (C.4)$$

Boundary conditions;

$$\phi_1 = \phi_{1x} = \phi_{1r} = 0 \qquad \text{at } x-\beta r\le 0 \quad (C.5)$$

$$\phi_{1r} - R'\phi_{1x} = -1 - ik(x-x_G+RR') \qquad \text{at } r=R(x) \quad (C.6)$$

Pressure coefficient;

$$C_p^1 = -2S_0[\phi_{1x}(1+\phi_{0x}) + \phi_{0r}(1+\phi_{1r}) + ik((x-x_G)\,\phi_{0r}$$

$$- R\phi_{0x} + \phi_1)] \qquad \text{at } r=R(x) \quad (C.7)$$

If the solution of the linearized equation in the body fixed is attempted we need to account for the right-hand-side terms in

Eq. (C.5). This can be done through the following particular solution

$$\phi_1^p(x,r) = r\phi_{0x} - (x-x_G)\phi_{0r} \qquad (C.8)$$

Therefore the solution of Eq. (C.5) can be expressed as $\phi_1(x,r) = \phi_1^h(x,r) + \phi_1^p(x,r)$ where ϕ_1^h is the solution to the homogeneous equation.

By substitution of this equation into Eq. (C.7) and (C.8) we obtain

$$\begin{aligned}\phi_{1r}^h - R'\phi_{1x}^h = {} & -1 - ik(x-x_G + RR') \\ & - \phi_{0x} - R\phi_{0xr} + (x-x_G)\cdot(\phi_{0rr} - R'\phi_{0xr}) \\ & + R'(\phi_{0xx}-\phi_{0r}) \qquad \text{at } r=R(x) \qquad (C.9)\end{aligned}$$

and

$$\begin{aligned}C_p^1 = {} & -2S_0\ \{\phi_{1x}^h(1+\phi_{0x}) + \phi_{0r}\phi_{1r}^h + ik\phi_1^h + R\phi_{0xx} \\ & - (x-x_G)(\phi_{0xr}(1+\phi_{0x}) + \phi_{0r}\phi_{0rr}) \\ & + R(\phi_{0x}\phi_{0xx} + \phi_{0r}\phi_{0xr})\} \qquad (C.10)\end{aligned}$$

It can be noticed that when the linearized equation is solved in the body fixed system also, second-order derivatives of the mean flow, and therefore singular terms, appear in the tangency condition and pressure coefficient.

In terms of slender body theory Hoffman and Platzer[12] have shown that although the velocity ϕ_{1r}, in the wind-fixed coordinate system is singular at the body apex, the pressure coefficient is regular. In the body-fixed system Revell[21] also

has shown that, within the approximation of the slender body theory, the pressure coefficient as obtained from the solution to the linearized equation for the unsteady cross flow, also remains regular.

In terms of not-so-slender body theory, this apex singularity has not been investigated before. In this Appendix the formulation in the wind-fixed system for unsteady flow is presented in a conical coordinate system (see Fig. 58) and shown that in this conical coordinate system the apex singularity is totally removed. For pointed bodies the body apex can be treated as a cone and, therefore, the assumption of conical flow and the use of a conical coordinate is justified at the apex.

The conical and cylindrical coordinates are related by the following equation

$$\left.\begin{aligned} s^2 &= x^2 + r^2 \\ \tan \nu &= r/x \end{aligned}\right\} \qquad (C.11)$$

The mean flow velocities in the x and r directions are given by (see Ref. 43)

$$\left.\begin{aligned} \phi_{0x} &= - a \cosh^{-1} \left(\frac{\cot \nu}{\beta}\right) \\ \phi_{0r} &= a \sqrt{\cot^2 \nu - \beta^2} \end{aligned}\right\} \qquad (C.12)$$

where $a = \dfrac{1}{\cot\sigma \sqrt{\cot^2\sigma - \beta^2} + \cosh^{-1}\left(\dfrac{\cot\sigma}{\beta}\right)}$.

and σ is the half-cone angle.

If the terms ϕ_{0rr} and ϕ_{0rx} are expressed in the conical coordinate we obtain

$$\left.\begin{aligned} \phi_{0rr} &= -\frac{a\cot^2\nu}{\sin\nu\sqrt{\cot^2\nu-\beta^2}}\frac{1}{s} \\ \phi_{0rx} &= -\frac{a\cot\nu}{\sin\nu\sqrt{\cot^2\nu-\beta^2}}\frac{1}{s} \end{aligned}\right\} \qquad (C.13)$$

and Eq. (C.1) when expressed in the conical system becomes

$$\phi_{1\nu} = -s\cos\sigma\left[1 + a\cosh^{-1}\left(\frac{\cot\sigma}{\beta}\right)\right] - \frac{a(\cos\sigma-s_G)}{\sin^3\sigma\sqrt{\cot^2\sigma-\beta^2}}$$

$$- ik(s\cos\sigma-s_G) \qquad \text{at } \nu=\sigma \qquad (C.14)$$

It can be seen that no singularity appears in this equation.

The form of Eq. (C.14) suggests that the solution ϕ_1 can be sought in the form of

$$\phi_1(s,\nu) = \sum_{n=0}^{\infty} s^n f_n(\nu) \qquad (C.15)$$

When the governing equation for ϕ_1 in the wind-fixed coordinate system is transformed to the (x,ν) coordinate and Eq. (C.15) is used we obtain

$$\sum_{n=0}^{\infty} s^{n-2}\Big[f_n(\nu)\big(n(n-1)(\sin^2\nu-\beta^2\cos^2\nu) + n(\cos^2\nu-\beta^2\sin^2\nu) + n - \frac{1}{\sin^2\nu}\big) + f'_n(\nu)\big(2\sin\nu\cos\nu(n-1)M_\infty^2 + \cot\nu\big) + f''_n(\nu)(\beta^2\sin^2\nu + \cos^2\nu)\Big] + k^2M_\infty^2 \sum_{n=0}^{\infty} s^n f_n(\nu) - 2ikM_\infty^2\Big[\sum_{n=0}^{\infty} s^{n-1}[f_n(\nu)n\cos\nu - f'_n(\nu)\sin\nu]\Big] = 0 \qquad (C.16)$$

When Eq. (C.15) is used to satisfy the boundary conditions, Eq. (C.14), the following equations and boundary conditions for f_0, f_1 and f_j (where $j=2,3,\ldots$) can be obtained from Eqs. (C.16) and (C.14)

$$\left.\begin{aligned} &(-\beta^2\sin^2\nu + \cos^2\nu)\, f''_0(\nu) - 2M_\infty^2 \sin\nu\cos\nu f'_0(\nu) \\ &+ \cot\nu f'_0(\nu) - \frac{1}{\sin^2\nu} f_0(\nu) = 0 \\ &f_0(\nu) = 0 \qquad \text{at } \nu=\mu \text{ (Mach wave)} \\ &f'_0(\nu) = s_G\Big(\frac{a}{\sin^3\sigma+\sqrt{\cot^2\sigma-\beta^2}} + ik\Big) \qquad \text{at } \nu=\sigma \text{ (cone surface)} \end{aligned}\right\} \qquad (C.17)$$

where s_G is the center of rotation in the conical coordinate system.

$$
\left.
\begin{aligned}
&(-\beta^2\sin^2\nu+\cos^2\nu)f_1''(\nu) + \cot\nu f_1'(\nu) \\
&- (\beta^2\sin^2\nu+\cos^2\nu\cot^2\nu)f_1(\nu) = -2ikM_\infty^2\sin\nu f_0(\nu) \\
&f_1(\nu) = 0 \qquad \text{at } \nu=\mu \\
&f_1'(\nu) = -\cos\sigma\Big[1 + \operatorname{acosh}^{-1}\Big(\frac{\cot\sigma}{\beta}\Big) \\
&\qquad + \frac{a}{\sin^3\sigma\sqrt{\cot^2\sigma-\beta^2}} - ik\Big] \qquad \text{at } \nu=\sigma
\end{aligned}
\right\} \quad (C.18)
$$

and finally a recurrence formulation can be written for $f_j(\nu)$ with $j=2,3,\ldots$

$$
\left.
\begin{aligned}
&f_j(\nu)\Big[j(j-1)\Big[\sin^2\nu-\beta^2\cos^2\nu) + j(\cos^2\nu-\beta^2\sin^2\nu) \\
&+ j - \frac{1}{\sin^2\nu}\Big] + f_j'(\nu)(2\sin\nu\cos\nu(j-1)M_\infty^2 + \cot\nu) \\
&+ f_j''(\nu)(\beta^2\sin^2\nu+\cos^2\nu) \\
&= -k^2M_\infty^2 f_{j-2}(\nu) + 2ikM_\infty^2 (f_{j-1}(\nu)(j-1)\cos\nu - f_{j-1}'(\nu)\sin\nu) \\
&f_j(\nu) = 0 \qquad \text{at } \nu=\mu \\
&f_j'(\nu) = 0 \qquad \text{at } \nu=\sigma, \text{ for } j\geq 2
\end{aligned}
\right\} (C.19)
$$

It can be seen that the solution to Eqs. (C.17), (C.18) and (C.19) do not give any singularity at the apex and therefore the potential as given by (C.15) will be regular at the apex. However, as with the slender body theory, the velocity ϕ_{1r} will be singular at the apex. As can be shown, it behaves like 1/s.

We need to investigate whether or not the pressure remains regular. To do so, let us consider first the terms $\phi_{0xr}(1+\phi_{0x}) + \phi_{0rr}\phi_{0r}$ in Eq. (C.2), which can be expressed at $\nu=\sigma$ as

$$\frac{1}{s}\frac{a\cot\sigma}{\sin\sigma\sqrt{\cot^2\sigma-\beta^2}}\left[1 - a\cosh^{-1}\left(\frac{\cot\sigma}{\beta}\right) - a\cot\sigma\sqrt{\cot^2\sigma-\beta^2}\right]$$

and by substitution of the value of a

$$\frac{a\cot\sigma}{ss\sin\sigma\sqrt{\cot^2\sigma-\beta^2}}\left[1 - \frac{\left(\cosh^{-1}\left(\frac{\cot\sigma}{\beta}\right)+\cot\sigma\sqrt{\cot^2\sigma-\beta^2}\right.}{\cot\sigma\sqrt{\cot^2\sigma-\beta^2}+\cosh^{-1}\left(\frac{\cot\sigma}{\beta}\right)}\right] = 0$$

and Eq. (C.2) for the pressure coefficient in the (s,ν) coordinate can be expressed as

$$C_p^1 = -2S_0\{(1+\phi_{0x})(\cos\nu\phi_{1s} - \frac{\sin\nu}{s}\phi_{1x}) + \phi_{0r}(\sin\nu\phi_{1s} + \frac{\cos\nu}{s}\phi_{1\nu}\} \qquad (C.20)$$

If Eq. (C.15) is substituted and the terms are rearranged, we obtain

$$C_p^1 = -2S_0\sum_{n=0}^{\infty} s^{n-1}\{nf_n(\nu)[\cos\nu(1+\phi_{0x}) + \sin\nu\phi_{0r}] - f_n'(\nu)(\sin\nu(1+\phi_{0x}) - \phi_{0r}\cos\nu)\} \qquad (C.21)$$

But $\sin\nu(1+\phi_{0x}) - \phi_{0r}\cos\nu) = -\phi_{0r} + \tan\nu(\phi_{0x}+1) = 0$ at $\nu=\sigma$ by the mean flow tangency condition. Therefore

$$C_p^1 = -2S_0 \sum_{n=0}^{\infty} s^{n-1} n f_n(\nu)(\cos\nu(1+\phi_{0x}) + \sin\nu\ \phi_{0r}) \quad (C.28)$$

Eq. (C.28) is finite everywhere. Therefore it is proved that for not-so-slender oscillating bodies the singularity at the body in the wind-fixed coordinate system is a spurious one and if the problem is formulated in a conical coordinate system, the pressure is regular at the apex. The same conclusions can be obtained if the previous formulation is done for the body-fixed coordinate system.

Since the singularity in the conical coordinate system is removed this solution for the body apex can be used as the starting solution. For the rest of the body a cylindrical coordinate system can be used and since the singularity has been removed a regular pressure coefficient will be obtained everywhere on the body.

APPENDIX D

EVALUATION OF THE INDUCED UNSTEADY POTENTIAL AND VELOCITIES BY A DISTRIBUTION OF SOURCES

APPENDIX D

As shown in Chapter 7 the induced potential by a distribution of unsteady sources at the point x_i, r_i, ϕ_m is given by

$$\phi_1(x_i, r_i, \theta_m) = \int_0^{x_i - \beta r_i} F_m(\xi) B(x_i - \xi, \beta r_i) d\xi \qquad (D.1)$$

When the transformation $\xi = x_i - \beta r_i \cosh\sigma$ is introduced to Eq. (D.1), the potential $\phi_1(x_i, r_i, \sigma_m)$ can be expressed as

$$\phi_1(x_i, r_i, \phi_m) = -\int_{\cosh^{-1}\frac{x_i}{\beta r_i}}^{0} F_m(x_i - \beta r_i \cosh\sigma)\ \bar{B}(\phi_1 \beta r_i) d\phi \qquad (D.2)$$

where $\bar{B}(\phi, \beta r_i) = e^{-i\mu\beta r_i \cosh\sigma} \cdot \cos(\lambda \beta r_i \sinh\phi)$.

After discretizing along the x-axis and upon applying the Harmonic Gradient model Eq. (D.2) can be expressed as

$$\phi_1(x_i, r_i, \sigma_m) = -\sum_{j=1}^{i} a_m^j \int_{\sigma_j}^{\sigma_{j+1}} [e^{-i\mu x_i} - e^{-i\mu\beta r_i \cosh\sigma}] \cdot \cos(\lambda \beta r_i \sinh\sigma) d\sigma \qquad (D.4)$$

where $\sigma_j = \cosh^{-1}(\frac{x_i - \xi_j}{\beta r_i})$ and $\sigma_{j+1} = \cosh^{-1}(\frac{x_i - \xi_{j+1}}{\beta r_i})$.

Since the integrand in Eq. (D.4) is regular the integration can be done numerically by a Gaussian quadrature.

The velocities in the x and r direction can be obtained by taking the derivatives with respect to x_i and r_i in Eq. (D.2). Thus, in the x direction we have

$$\frac{\partial \phi_j}{\partial x_i} = \frac{\partial}{\partial x_i}\left[\cosh^{-1}\frac{x_i}{\beta r_j}\right] F_m(0)\bar{B}\left(\cosh^{-1}\frac{x_i}{\beta r_i},\ \beta r_i\right)$$

$$-\int_{\cosh^{-1}\frac{x_i}{\beta r_j}}^{0} \frac{\partial}{\partial x_i} F_m(x_i - \beta r_i \cosh\sigma)\bar{B}(\sigma_1 \beta r_i)\,d\sigma \qquad (D.5)$$

If the condition that the source strength at the body apex is equal to zero is now imposed, $F_m(0)=0$, Eq. (D.5) is then expressed as

$$\frac{\partial \phi_j}{\partial x_i} = -\int_{\cosh^{-1}\frac{x_i}{\beta r_i}}^{0} \frac{\partial}{\partial x_i} F_m(x_i - \beta r_i \cosh\sigma)\bar{B}(\sigma_1 \beta r_i)\,d\sigma \qquad (D.6)$$

Eq. (D.6) after discretization along the body axis and upon applying the Harmonic Gradient model can be expressed as

$$\frac{\partial \phi_j}{\partial x_i} = -\sum_{j=1}^{i} a_m^j\, e^{-i\mu x_i} \int_{\sigma_j}^{\sigma_{j+1}} \cos(\lambda \beta r_i \sinh\sigma)\,d\sigma \qquad (D.7)$$

Since the integrands of Eq. (D.7) are regular the integrals of Eq. (D.7) are evaluated numerically by a Gaussian gradrature.

The velocity in the r direction is given by

$$\frac{\partial \phi_j}{\partial r_i} = \frac{\partial}{\partial r_i}\left[\cosh^{-1}\frac{x_i}{\beta r_i}\right] F_m(0)\bar{B}\left(\cosh^{-1}\frac{x_i}{\beta r_i},\ \beta r_i\right)$$

$$-\int_{\cosh^{-1}\frac{x_i}{\beta r_i}}^{0} \frac{\partial}{\partial r_i}\left[F_m(x_i - \beta r_i \cosh\sigma)\bar{B}(\sigma_1 \beta r_i)\right] d\sigma \qquad (D.8)$$

Now applying again $F_m(0) = 0$ and after discretization and making use of the Harmonic Gradient model Eq. (D.8) can be expressed as

$$\frac{\partial \phi_1}{\partial r_i} = \sum_{j=1}^{i} a_m^j \int_{\sigma_j}^{\sigma_{j+1}} [\beta \cosh\sigma \; e^{-i\mu\beta r_i \cosh\sigma} \cdot \cos(\lambda\beta r_i \sinh\sigma)$$

$$+ (e^{-i\mu\beta r_i \cosh\sigma} - e^{-i\mu x_i}) \frac{\lambda\beta}{i\mu} \sinh\sigma \cdot \sin(\lambda\beta r_i \sinh\sigma)] d\sigma \qquad (D.9)$$

The integrals appearing on Eq. (D.9) are also evaluated numerically by Gaussian quadrature.

Note that the transformations in Eq. (D.2), as previously used by von Karman (Ref. 13) and Tsien (Ref. 40), provides only the principal value for the integral. Furthermore, it also removes the singularities along the Mach cone $x - \beta r = 0$, rendering the numerical evaluation of the integral much easier.

APPENDIX E

EXPLICIT EXPRESSIONS OF MATRICES $[A]_i$, $[Y]_{ji}$ AND $[H]_i$ IN EQ. (7.11)

APPENDIX E

The explicit expressions of matrices $[A]_i$, $[Y]_{ji}$ and $[H]_i$, involving all the elements, in Eq. (7.11) are as follows:

$$[A]_i = \begin{bmatrix} \sum_{h=m-1}^{m+1} W_h (S_i^{i+1})^2 & \sum_{h=m-1}^{m+1} W_h S_i^{i+1} D_i^{i+1} \cos\bar{\theta}_h & \sum_{h=m-1}^{m+1} W_h S_i^{i+1} D_i^{i+1} \sin\bar{\theta}_h \\ \sum_{h=m-1}^{m+1} W_h S_i^{i+1} D_i^{i+1} \cos\bar{\theta}_h & \sum_{h=m-1}^{m+1} W_h (D_i^{i+1} \cos\bar{\theta}_h)^2 & \sum_{h=m-1}^{m+1} W_h (D_i^{i+1})^2 \sin\bar{\theta}_h \cos\theta_h \\ \sum_{h=m-1}^{m+1} W_h S_i^{i+1} D_i^{i+1} \sin\bar{\theta}_h & \sum_{h=m-1}^{m+1} W_h (D_i^{i+1})^2 \sin\bar{\theta}_h \cos\bar{\theta}_h & \sum_{h=m-1}^{m+1} W_h (D_i^{i+1} \sin\bar{\theta}_h)^2 \end{bmatrix}$$

$$[Y]_{ji} = \begin{bmatrix} \sum_{h=m-1}^{m+1} W_h S_j^{j+1} S_i^{i+1} & \sum_{h=m-1}^{m+1} W_h D_j^{j+1} S_i^{i+1} \cos\bar{\theta}_h & \sum_{h=m-1}^{m+1} W_h D_j^{j+1} S_i^{i+1} \sin\bar{\theta}_h \\ \sum_{h=m-1}^{m+1} W_h S_j^{j+1} D_i^{i+1} \cos\bar{\theta}_h & \sum_{h=m-1}^{m+1} W_h D_j^{j+1} D_i^{i+1} \cos^2\bar{\theta}_h & \sum_{h=m-1}^{m+1} W_h D_j^{j+1} D_i^{i+1} \sin\bar{\theta}_h \cos\bar{\theta}_h \\ \sum_{h=m-1}^{m+1} W_h S_j^{j+1} D_i^{i+1} \sin\bar{\theta}_h & \sum_{h=m-1}^{m+1} W_h D_j^{j+1} D_i^{i+1} \sin\bar{\theta}_h \cos\bar{\theta}_h & \sum_{h=m-1}^{m+1} W_h D_j^{j+1} D_i^{i+1} \sin^2\bar{\theta}_h \end{bmatrix}$$

$$[H]_i = \begin{bmatrix} W_{m-1} S_i^{i+1} & W_m S_i^{i+1} & W_{m+1} S_i^{i+1} \\ W_{m-1} D_i^{i+1} \sin\bar{\theta}_{m-1} & W_m D_i^{i+1} \cos\bar{\theta}_m & W_{m+1} D_i^{i+1} \cos\bar{\theta}_{m+1} \\ W_{m-1} D_i^{i+1} \sin\bar{\theta}_{m-1} & W_m D_i^{i+1} \sin\bar{\theta}_m & W_{m+1} D_i^{i+1} \sin\bar{\theta}_{m+1} \end{bmatrix}$$

REFERENCES

1. Farrar, D.J., "Structures," *Journal of the Royal Aeronautical Society,* Vol. 60, November 1956, pp. 712-720.

2. Woodward, F.A., "An Improved Method for the Aerodynamic Analysis of Wing-Body-Tail Configuration in Subsonic and Supersonic Flow," NASA CR-2228, 1973.

3. Magnus, A.E. and Epton, M.A., "PANAIR - A Computer Program for Predicting Subsonic or Supersonic Linear Potential Flows about Arbitrary Configurations Using a Higher Order Panel Method, Vol. 1. Theory Document (Version 1.0)," NASA CR-3251, 1980.

4. Chen, P.C. and Liu, D.D., "A Harmonic Gradient Method for Unsteady Supersonic Flow Calculations," *Journal of Aircraft*, Vol. 22, May 1985, pp. 371-379.

5. Adams, M.C. and Sears, W.R., "Slender Body Theory - Review and Extension," *Journal of Aeronautical Sciences,* Vol. 20, No. 2, Feb. 1953, pp. 85-98.

6. Miles, J.W. and Young, D., "Generalized Missile Dynamics Analysis III - Aerodynamics," GM-TR-0165-00360, Space Tech. Labs, The Ramo-Wooldridge Corp., Apr. 7, 1958.

7. Lansing, D.L., "Velocity Potential and Forces on Oscillating Slender Bodies of Revolution in Supersonic Flow Expanded to the Fifth Power of the Frequency," NASA TND-1225, 1962.

8. Platzer, M.F. and Sherer, A.D., "Dynamic Stability Analysis of Bodies of Revolution in Supersonic Flow," *Journal of Space and Rockets,* Vol. 5, No. 7, July 1968, pp. 833-837.

9. Tobak, M. and Wehrend, W.R., "Stability Derivatives of Cones at Supersonic Speeds," NASA-TN 3788, September 1956.

10. Van Dyke, M.D., "First and Second Order Theory of Supersonic Flow Past Bodies of Revolution," *Journal of Aeronautical Sciences*, Vol. 18, No. 3, March 1951, pp. 161-178.

11. Bond, R. and Packard, B.B., "Unsteady Aerodynamic Forces on a Slender Body of Revolution in Supersonic Flow," NASA-TND-859, May 1961.

12. Hoffman, G. and Platzer, M.F., "On Supersonic Flow Past Oscillating Bodies of Revolution," *AIAA Journal*, Vol. 4, Feb. 1966, p. 370.

13. von Karman, T. and Moore, N.B., "The Resistance of Slender Bodies," *Trans. ASME 54*, pp. 303-310.

14. Hanson, P.W. and Doggett, R.V., "Wind-Tunnel Measurements of Aerodynamic Damping Derivatives of a Launch Vehicle Vibrating in Free-Free Bending Modes at Mach Numbers from 0.80 to 2.87 and Comparisons with Theory," NASA TND-1391, Oct. 1962.

15. Hanson, P.W. and Doggett, R.V., "Aerodynamic Damping of a 0.02-Scale Saturn SA-1 Model Vibrating in the First Free-Free Bending Mode," NASA TND-1956, Sept. 1963.

16. Sewall, J.L., Hess, R.W. and Watkins, C.E., "Analytical and Experimental Investigation of Flutter and Divergence of Spring-Mounted Cone Configurations at Supersonic Speeds," NASA TND-1021, April 1962.

17. Platzer, M.F. and Liu, D.D., "A Linearized Characteristics Method for Supersonic Flow Past Bodies of Revolution Performing Bending Oscillations," LMSC/HREC A 784262 Lockheed Missiles and Space Company, May 1967.

18. Hoffman, G.H. and Platzer, M.F., "Higher Approximations for Supersonic Flow Past Slowly Oscillating Bodies of Revolution," *Acta Mechanica*, Vol. 5, 1968, pp. 143-162.

19. McCanless, G.F., "Aerodynamic First-Order Method for Flexible Bodies," *Journal of Spacecraft and Rockets*, Vol. 7, No. 9, Sept. 1970, pp. 1037-1042.

20. Lighthill, M.J., "Note on the Swimming of Slender Fish," *Journal of Fluid Mechanics*, Vol. 9, 1960, pp. 305-317.

21. Revell, J.D., "Second-Order Theory for Unsteady Supersonic Flow Past Slender, Pointed Bodies of Revolution," *Journal of the Aerospace Sciences*, Vol. 27, No. 10, Oct. 1960, pp. 730-740.

22. Sauer, R., *Introduction to Theoretical Gas Dynamics*, 1st Ed., J.W. Edwards, Ann Arbor, Mich. 1947, pp. 77-81.

23. Ferri, A., *Elements of Aerodynamics of Supersonic Flows*, 1st Ed., pp. 210-235; The Macmillan Company, New York, 1949.

24. Krasnov, N.F., *Aerodynamics of Bodies of Revolution*, American Elsevier Publishing Company, 1970, pp. 239-263.

25. Schiff, L.B. and Sturek, W.B., "Numerical Simulation of Steady Supersonic Flow over an Ogive-Cylinder-Boattail Body," AIAA Paper No. 80-0066, 1980.

26. Garrick, I.E., "Nonsteady Wing Characteristics," Vol. 7, High Speed Aerodynamics and Jet Propulsion, Princeton University Press, 1957, pp. 668-679.

27. Laschka, B., "Der harmonisch Schwingende Rechteckflugel bei Überschallströmung," Bericht der Ernst Keinkel Flugzugbau GmbH, 1960.

28. Landahl, M.T., *Unsteady Transonic Flow*, Pergamon Press, New York, 1961, p. 19.

29. Ashley, H. and Zartarian, G., "Piston theory: A New Aerodynamic Tool for the Aeroelastician," *Journal of Aeronautical Sciences*, Vol. 23, No. 12, Dec. 1956, pp. 1109-1118.

30. Liu, D.D. and Pi, W.S., "Transonic Kernel Function Method for Unsteady Flow Calculations Using a Unified Linear Pressure Panel Procedure," AIAA Paper No. 80-0737-CP.

31. Brong, E.A., "The Flow Field above a Right Circular Cone in Unsteady Flight," AIAA Paper No. 65-398, 1965.

32. Ericsson, L.E., "Viscous Effects On Missile Aerodynamics at Low Angles of Attack," *Journal of Spacecraft and Rockets*, Vol. 18, No. 5, Sept.-Oct. 1981, pp. 401-405.

33. Fung, Y.C., *An Introduction to the Theory of Aeroelasticity*, John Wiley and Sons, New York, 1955.

34. Ward, G.N., *Linearized Theory of Steady High-Speed Flow*, Cambridge University Press, Cambridge, 1955.

35. Devan, L., "Conical, Noncircular, Second-Order, Potential Theory of Supersonic Flow," *AIAA Journal*, Vol. 22, May, 1984, pp. 618-623.

36. Woodward, F.A. and Landrum, E.J., "The Supersonic Triplet -- A New Aerodynamic Panel Singularity with Directional Properties," *AIAA Journal*, Vol. 18, No. 2, Feb. 1980.

37. Dowell, E.H. and Widnall, S.E., "Generalized Aerodynamic Forces on an Oscillating Cylindrical Shell," Quarterly of Applied Mathematics, No. 1, 1966, pp 1-17.

38. Platzer, M.F., Brix Jr., C.W. and Webster, K.A., "Linearized Characteristics Method for Supersonic Flow Past Vibrating Shells," *AIAA Journal*, Vol. 11, No. 9, 1973, pp. 1302-1305.

39. Arfken, G., *Mathematical Methods for Physicists*, Academic Press, New York, 1970.

40. Tsien, Hsue-Shen, "Supersonic Flow over an Inclined Body of Revolution," *Journal of the Aeronautical Sciences*, Vol. 5, No. 12, Oct. 1938, pp. 480-483.

41. Stannard, E.A., "Nonsteady Transonic and Supersonic Flow about Flexible Slender Bodies of Revolution," Ph.D. Thesis, University of Illinois, 1961.

42. Labrujere, T.E., Roos, R. and Erkelens, L.J.J., "The Use of Panel Methods with a View to Problems in Aircraft Dynamics," NLR MP-77009U.

43. Liepmann, H.W. and Roshko, A., *Elements of Gas Dynamics*, John Wiley and Sons, New York, 1957.

44. Tobak, M., "Damping-in-Pitch of Low-Aspect-Ratio Wings at Subsonic and Supersonic Speeds," NACA RM A52L04a, 1953.

45. Heitmeyer, J.C., "Lift, Drag, and Pitching Moment of Low-Aspect-Ratio Wings at Subsonic and Supersonic Speeds -- Plane Triangular Wing of Aspect Ratio 3 with NACA 0003-63 Sections," NACA RM A51H02, 1951.

46. Henderson Jr., Arthur, "Pitching-Moment Derivatives C_{m_q} and C_{α} at Supersonic Speeds for a Slender-Delta-Wing and Slender-Body Configuration and Approximate Solutions for Broad-Delta-Wing and Slender-Body Combinations," NACA TNL553, 1951.

47. Garcia-Fogeda, P. and Liu, D.D., "A Harmonic Potential Panel Method for Flexible Bodies in Unsteady Supersonic Flow," AIAA 24th Aerospace Sciences Meeting, January 6-9, 1986, Reno, Nevada, AIAA Paper No. 86-0007.

48. Garcia-Fogeda, P. and Liu, D.D., "Aeroelastic Applications of Harmonic Potential Panel Method to Oscillating Flexible Bodies in Supersonic Flow," May 19-21, 1986, San Antonio, Texas, AIAA Paper No. 86-0864-CP.

49. Liu, D.D., Garcia-Fogeda, P., and Chen, P.C., "Oscillating Wings and Bodies with Flexure in Supersonic Flow -- Applications of Harmonic Potential Panel Method," September 7-12, 1986, London, U.K., International Council of the Aeronautical Sciences, I.C.A.S. Paper No. 86-2.9.4.

50. Garcia-Fogeda, P. and Liu, D.D., "Three Dimensional Analysis of Supersonic Flows Around Arbitrary Bodies Using Boundary Collocation Method," *Boundary Element Techniques: Applications in Fluid Flow and Computational Aspects*, Computational Mechanics Publications (edited by Brebbia and Venturini) pp. 75-88, June 1987.

51. Garcia-Fogeda, P. and Liu, D.D., "Analysis of Unsteady Aerodynamics for Elastic Bodies in Supersonic Flow," *Journal of Aircraft*, Vol. 24, No. 12, December 1987, pp. 833-840.

52. Garcia-Fogeda, P., Chen, P.C., and Liu, D.D., "Unsteady Supersonic Flow Calculations for Wing-Body Combinations Using Harmonic Gradient Method," January 11-14, 1988, Reno, Nevada, AIAA 26th Aerospace Sciences Meeting, AIAA Paper No. 88-0568.

53. Garcia-Fogeda, P. and Liu, D.D., "Supersonic Aeroelastic Applications of Harmonic Potential Panel Method to Oscillating Flexible Bodies," *Journal of Spacecraft and Rockets*, Vol. 25, No. 4, July-August 1988, pp. 271-277.

54. Liu, D.D., Garcia-Fogeda, P. and Chen, P.C., "Oscillating Wings and Bodies with Flexure in Supersonic Flow," *Journal of Aircraft*, Vol. 25, No. 6, June 1988, pp. 507-514.

55. Liu, D.D. and Garcia-Fogeda, P., "Operational Manual for HPP1 Code: Unsteady Supersonic Aerodynamics for Flexible Bodies," ASU Report CR-R-86003, January 1986.

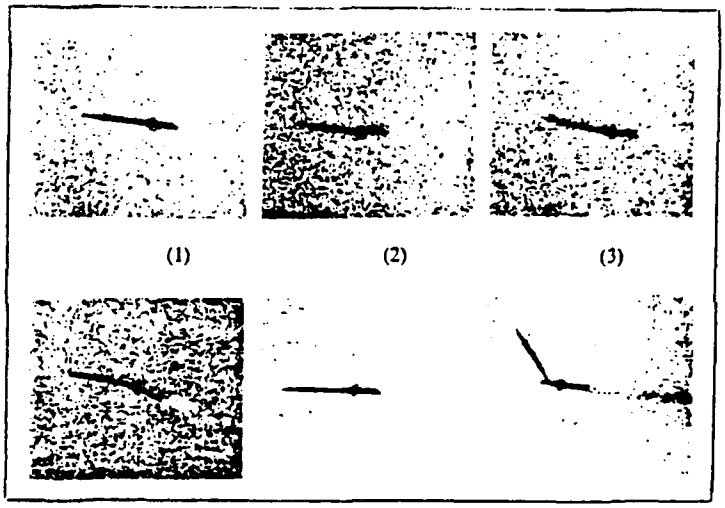

Fig. 1 Body bending flutter of British J.T.V.I. ramjet missile.

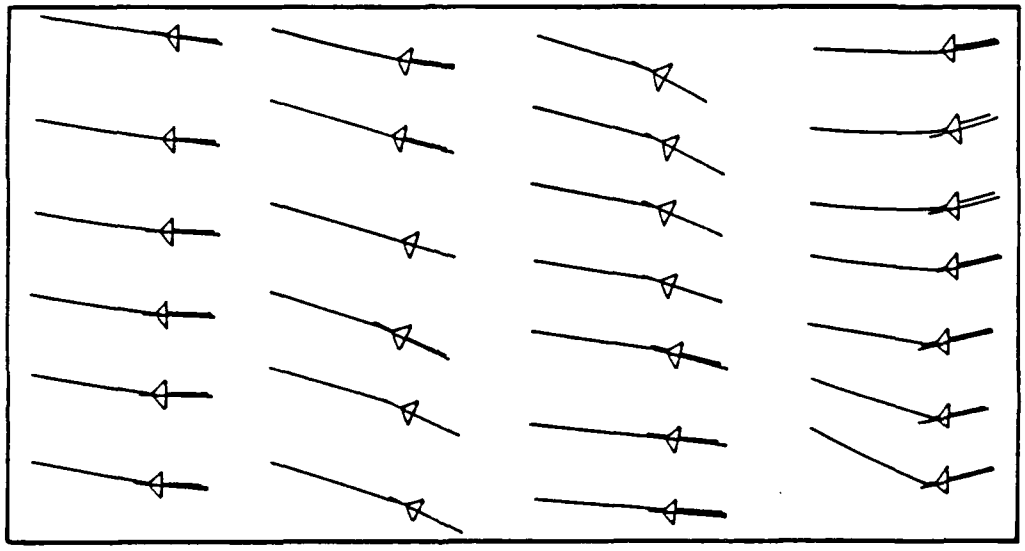

Fig. 2 Sequence of flutter modes at intervals of 1/100 second during the flutter incident.

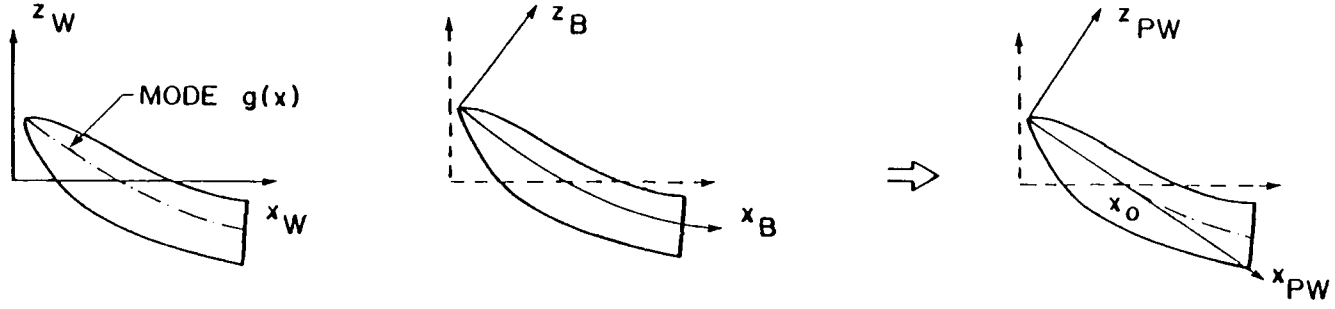

Fig. 3 Wind-fixed, body-fixed, pseudo-wind-fixed coordinate system.

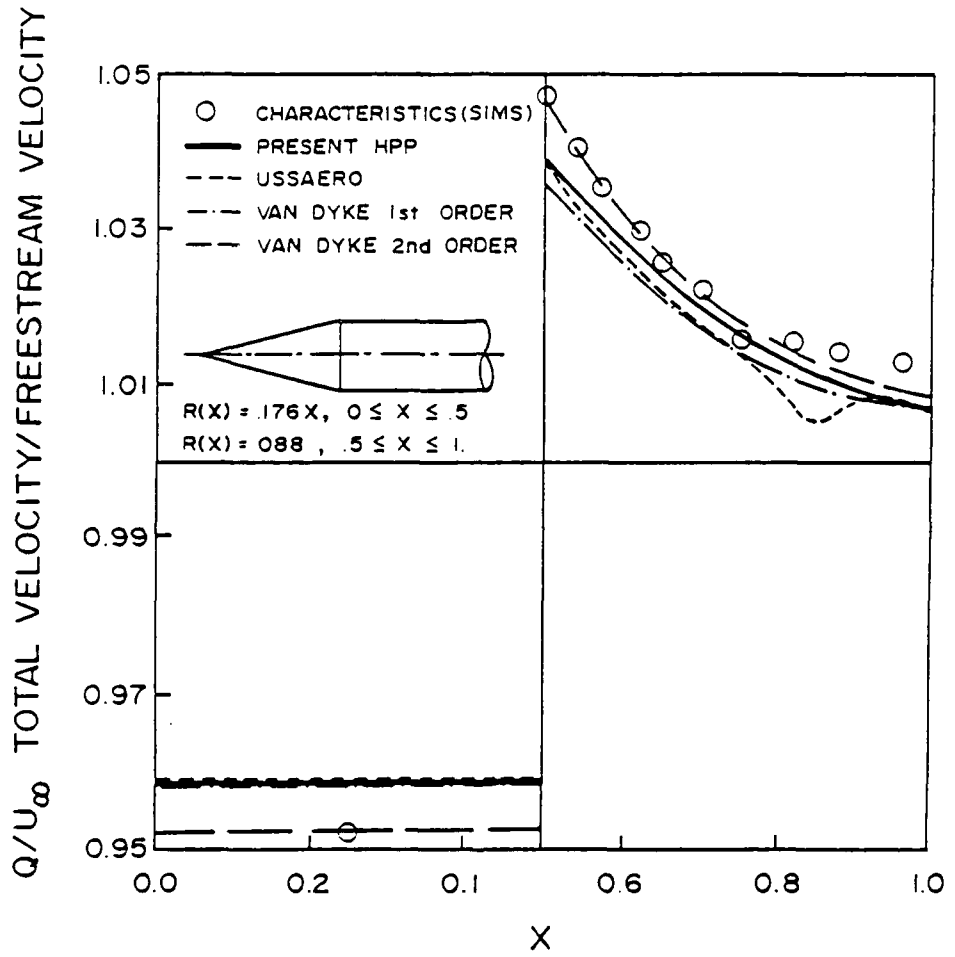

Fig. 4 Comparison of normalized velocities on a cone-cylinder surface at M_∞=2.075 and angle of attack α=0°.

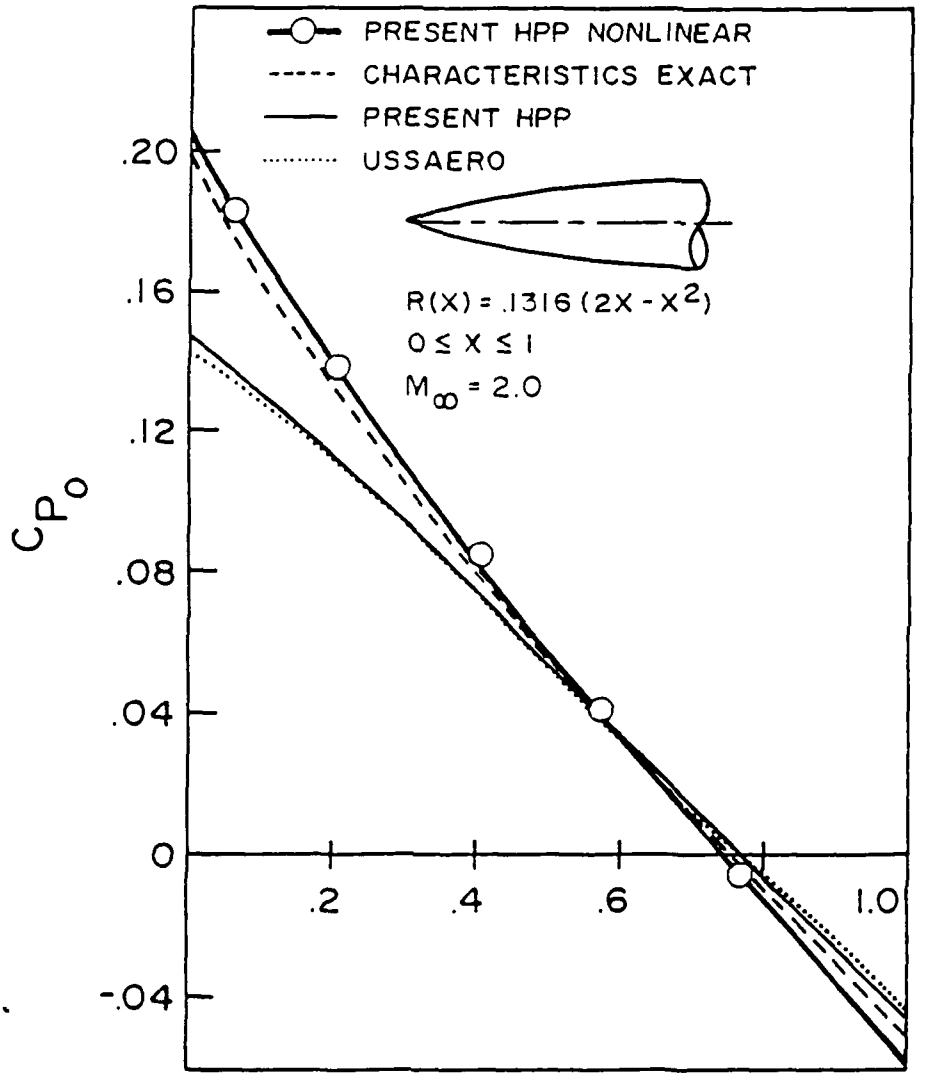

Fig. 5 Mean flow pressures for a parabolic-ogive at M_∞=2.0 and angle of attack α=0°.

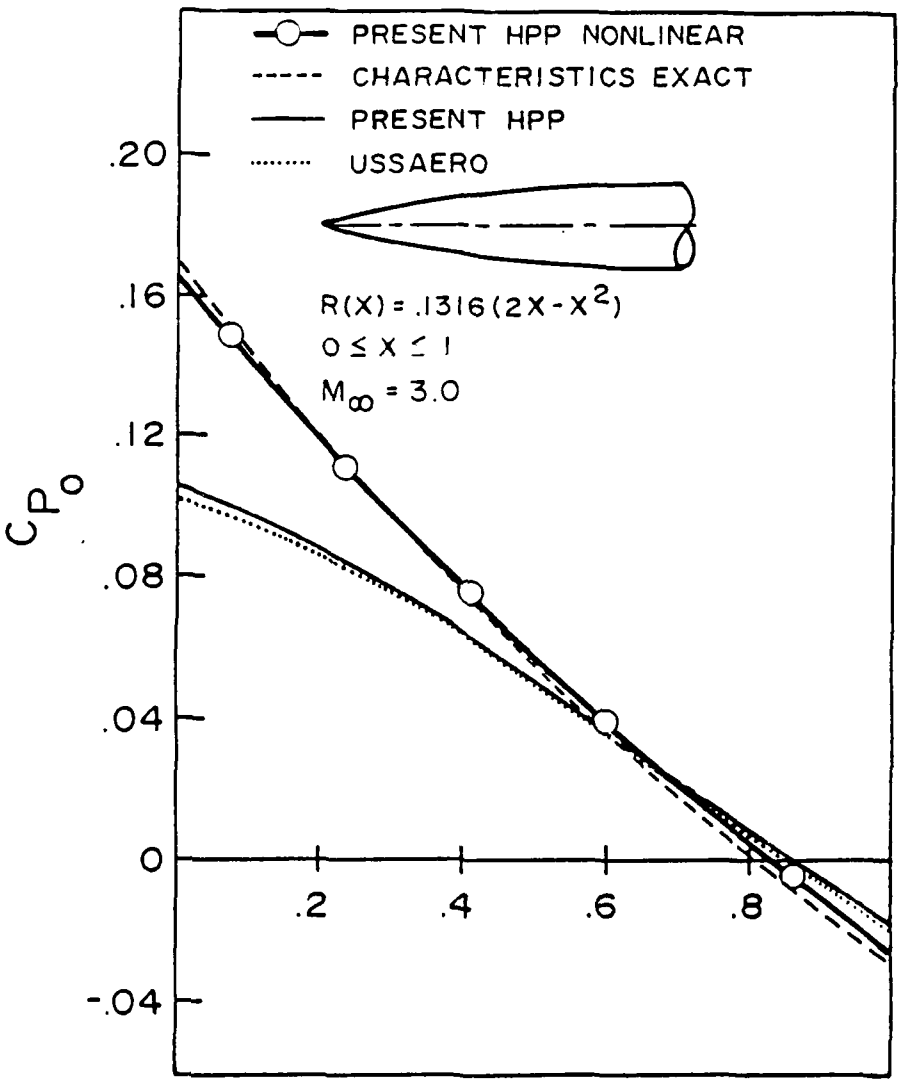

Fig. 6 Mean flow pressures for a parabolic-ogive at M_∞=3.0 and angle of attack α=0°.

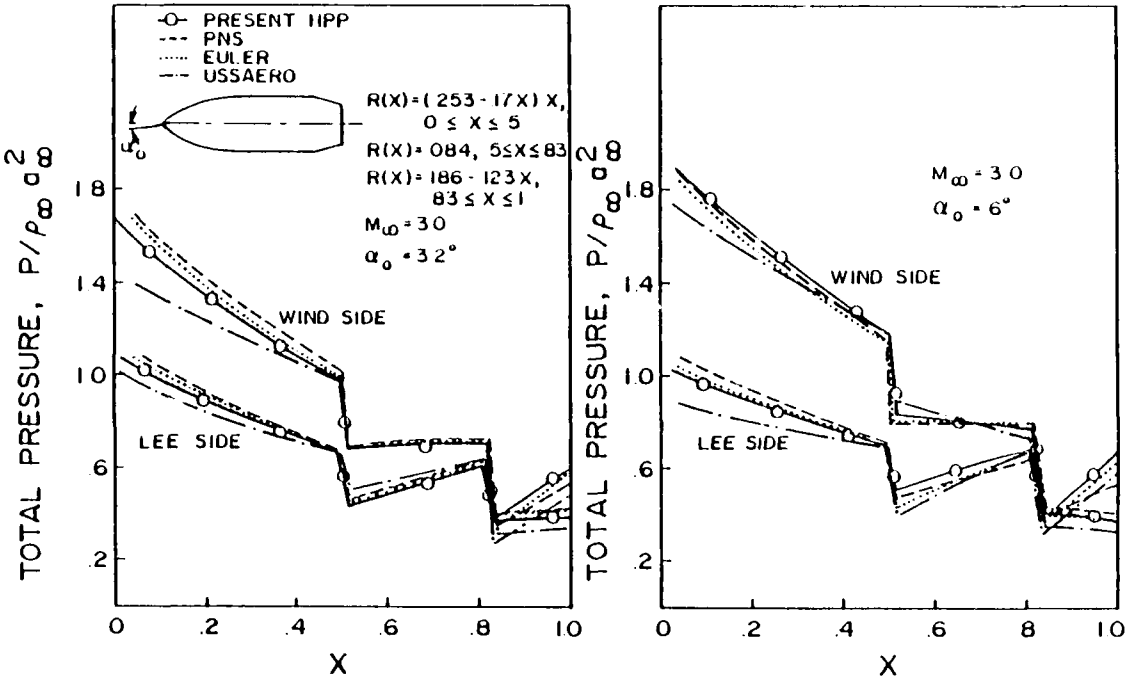

a) Angle of attack α=3.2° b) Angle of attack α=6.3°

Fig. 7 Total pressure distributions of an ogive-cylinder-boattail body at M_∞=3.0.

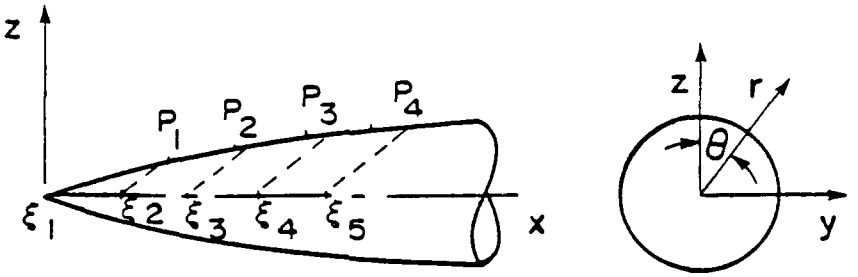

$$P_j = (X_j,\ R(X_j))$$

Fig. 8 Panel arrangement for axisymmetric bodies.

HPP METHOD

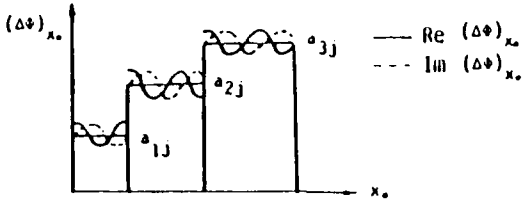

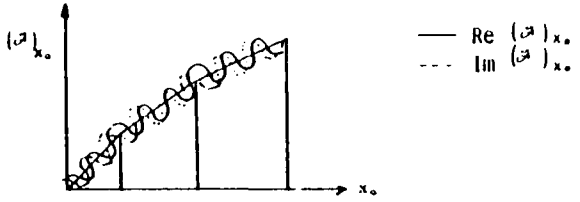

- H-G Model (Wing)

$$\frac{\partial}{\partial x_0}\left|\Delta\varphi_{1j}\, e^{-i\mu x_0}\right| = a_{1j}\, e^{-i\mu x_0}$$

- HPP Model (Body)

$$\frac{\partial}{\partial x_0}\left|F_1(x_j-x_0)\, e^{-i\mu x_0}\right| = (a_1(x_j-x_0)+b_1)e^{-i\mu x_0}$$

Fig. 9 Harmonic gradient model.

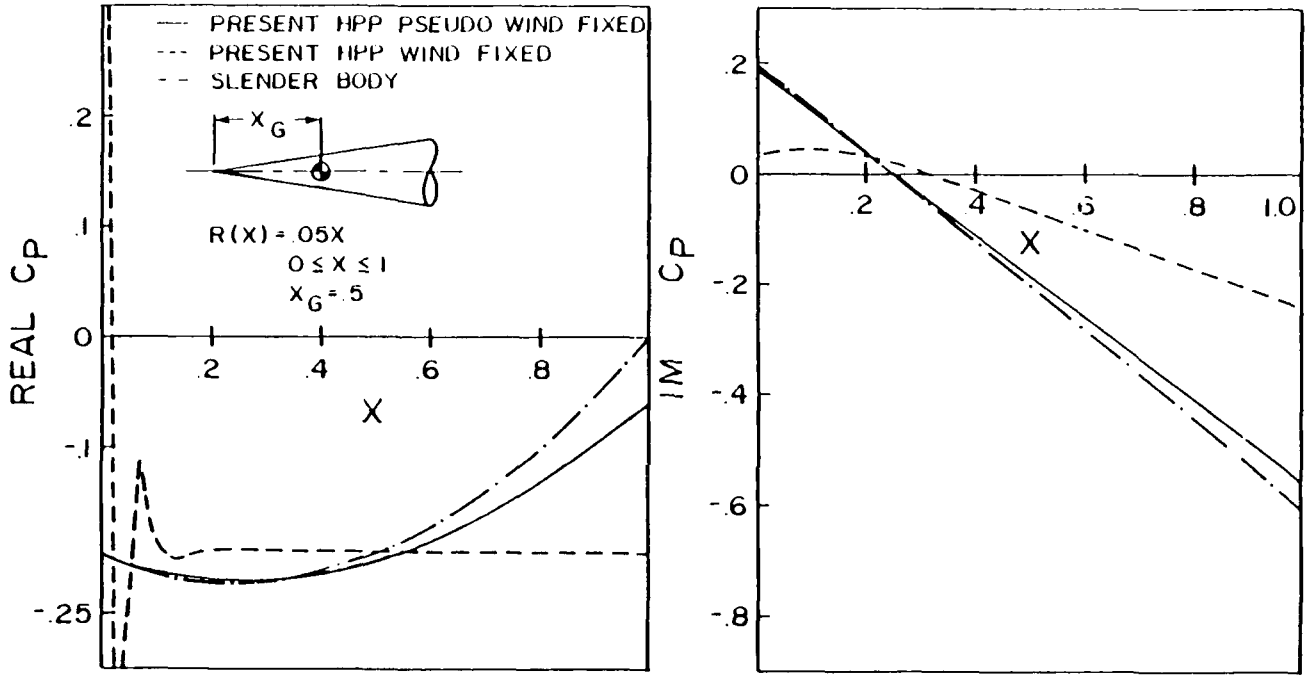

Fig. 10 In-phase and out-of-phase pressure coefficients for a cone in pitching mode at M_∞=2.0 and reduced frequency k=2.0.

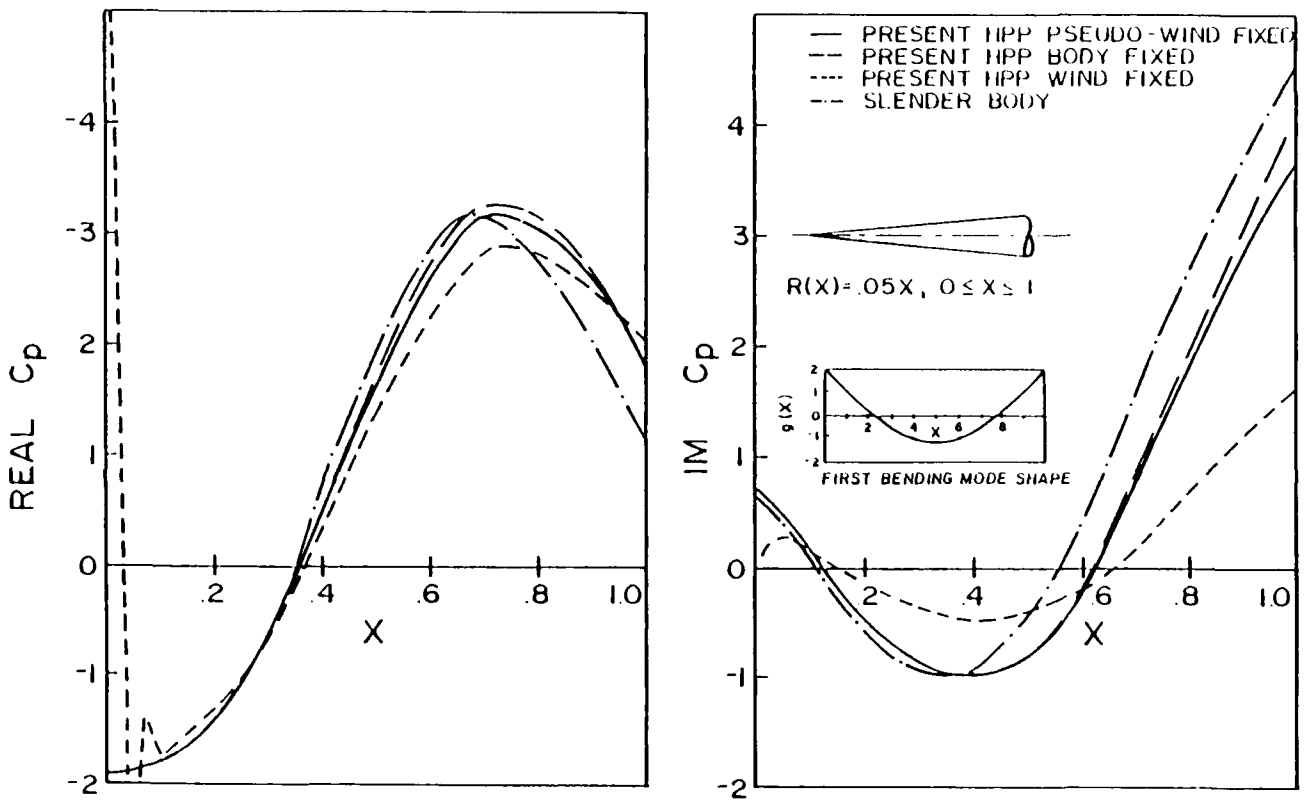

Fig. 11 In-phase and out-of-phase pressure coefficients for a cone in first bending mode at M_∞=2.0 and reduced frequency k=2.0.

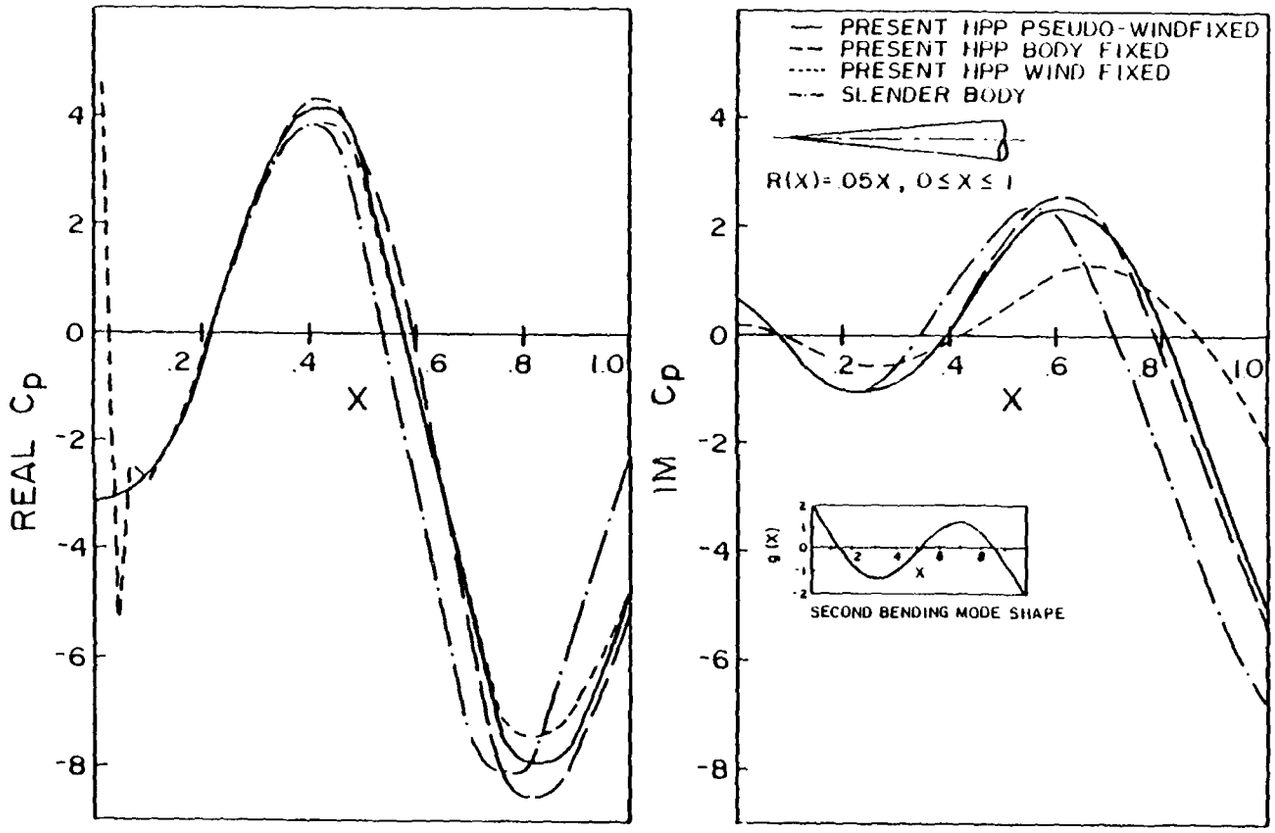

Fig. 12 In-phase and out-of-phase pressure coefficients for a cone in second bending mode at M_∞=2.0 and reduced frequency k=2.0.

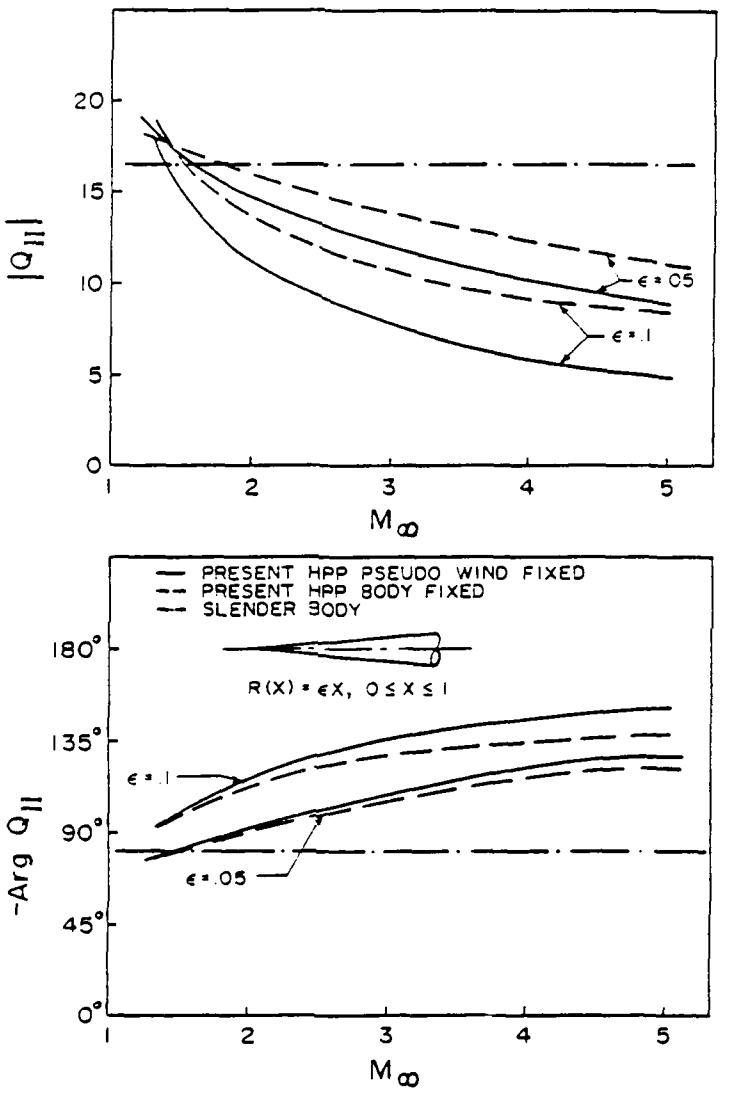

Fig. 13 Modulus and argument of the generalized forces versus Mach number for a cone in first bending mode (I=3) at reduced frequency k=2.0.

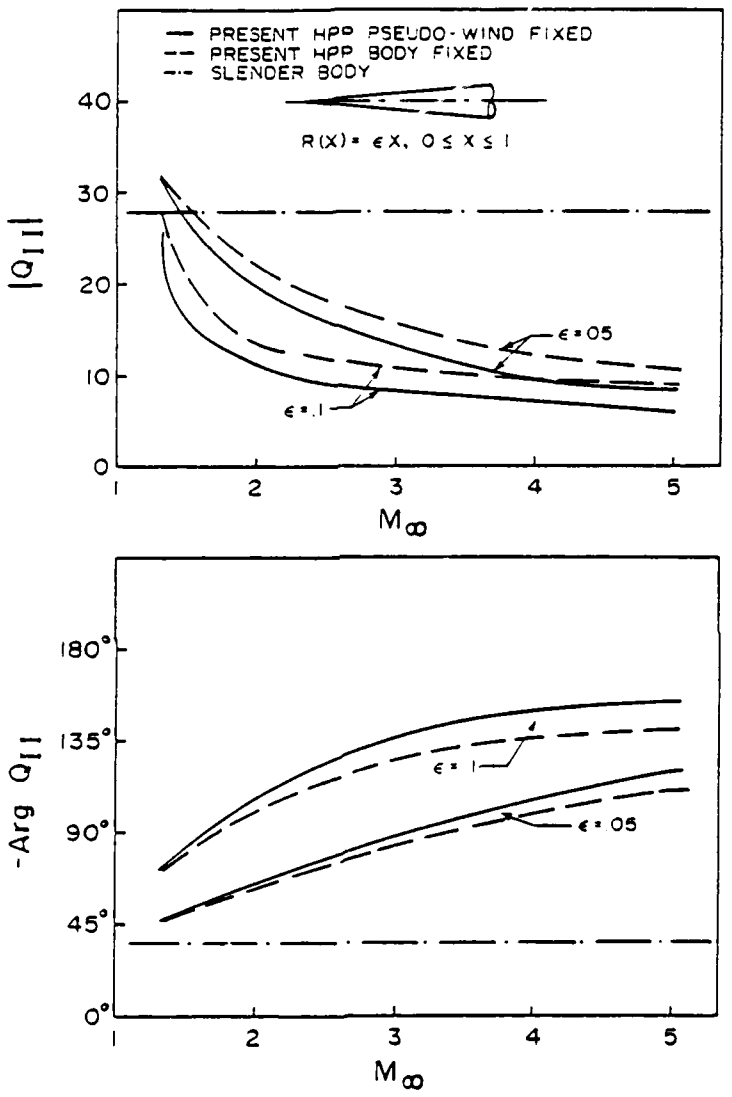

Fig. 14 Modulus and argument of the generalized forces versus Mach number for a cone in first bending mode (I=4) at reduced frequency k=2.0.

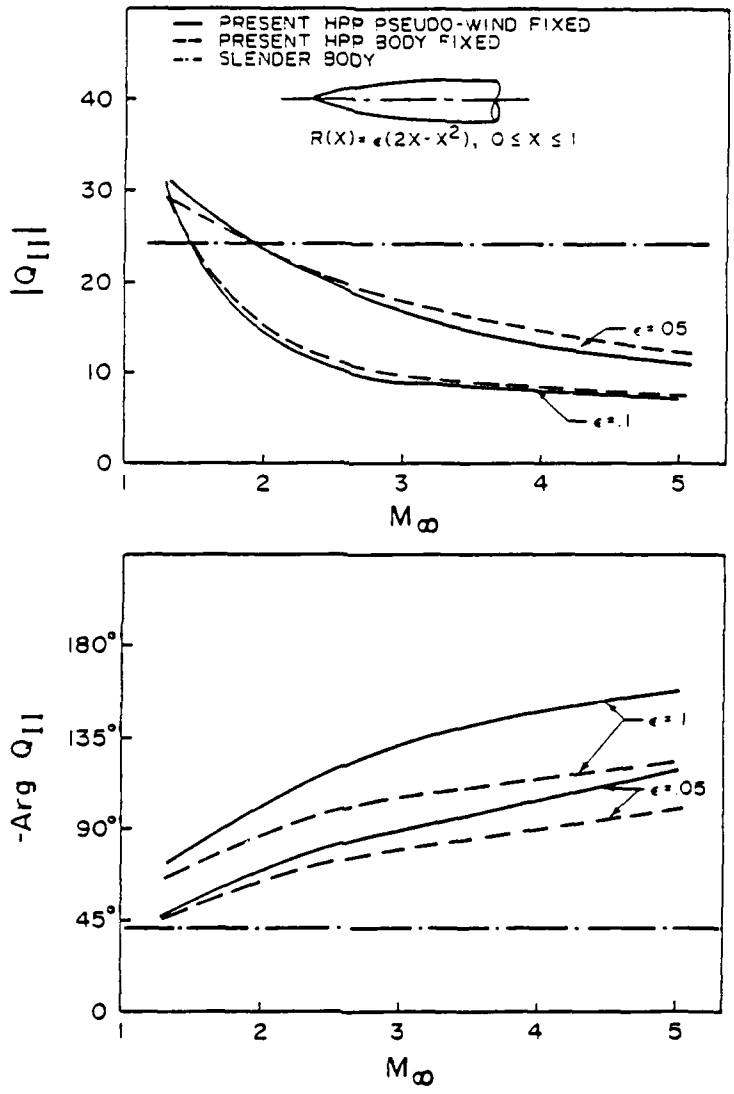

Fig. 15 Modulus and argument of the generalized forces versus Mach number for a parabolic-ogive in first bending mode (I=3) at reduced frequency k=2.0.

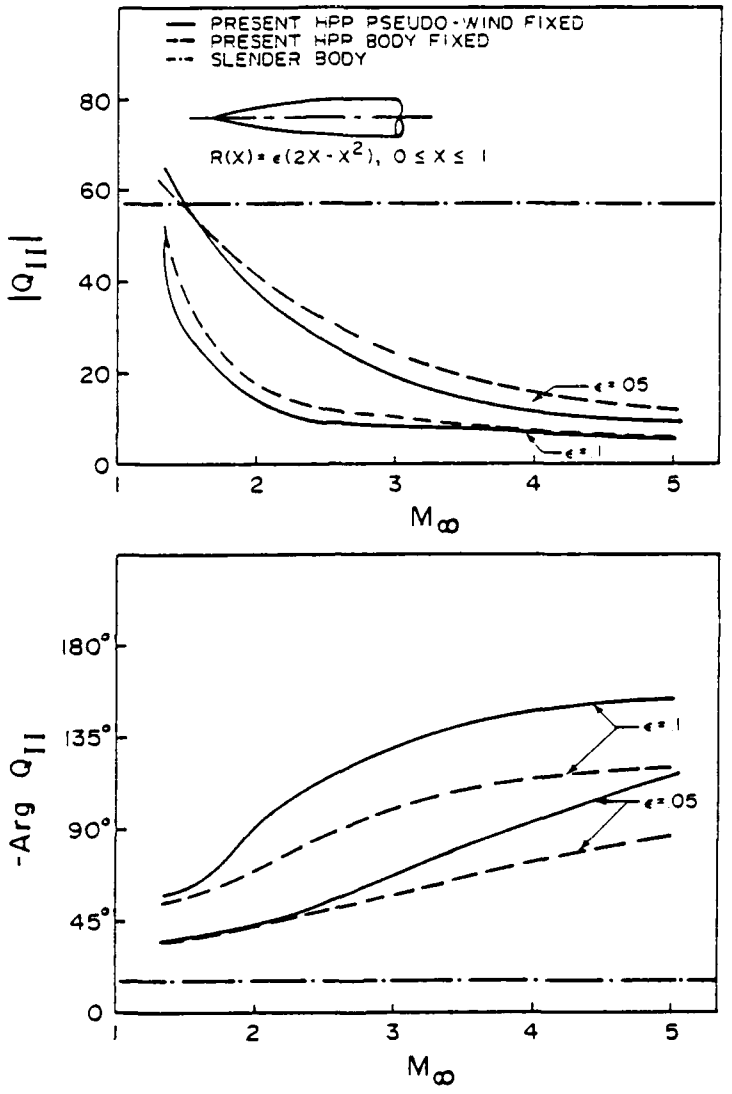

Fig. 16 Modulus and argument of the generalized forces versus Mach number for a parabolic-ogive in second bending mode (I=4) at reduced frequency k=2.0.

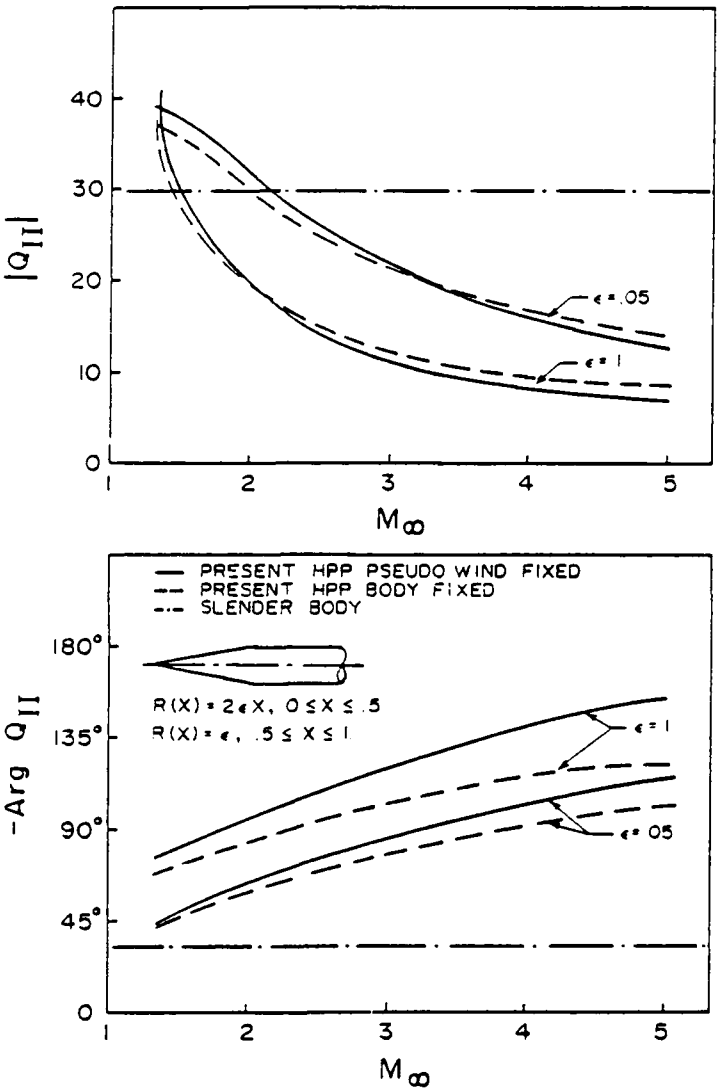

Fig. 17 Modulus and argument of the generalized forces versus Mach number for a cone-cylinder in first bending mode (I=3) at reduced frequency k=2.0.

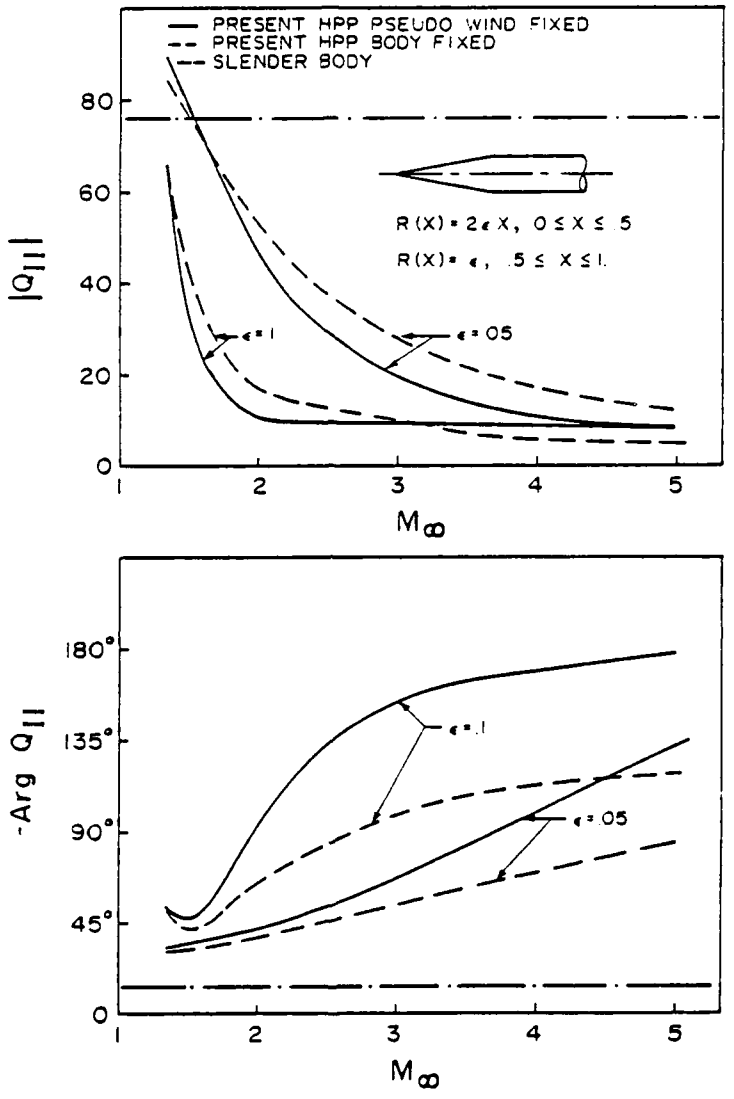

Fig. 18 Modulus and argument of the generalized forces versus Mach number for a cone-cylinder in second bending mode (I=4) at reduced frequency k=2.0.

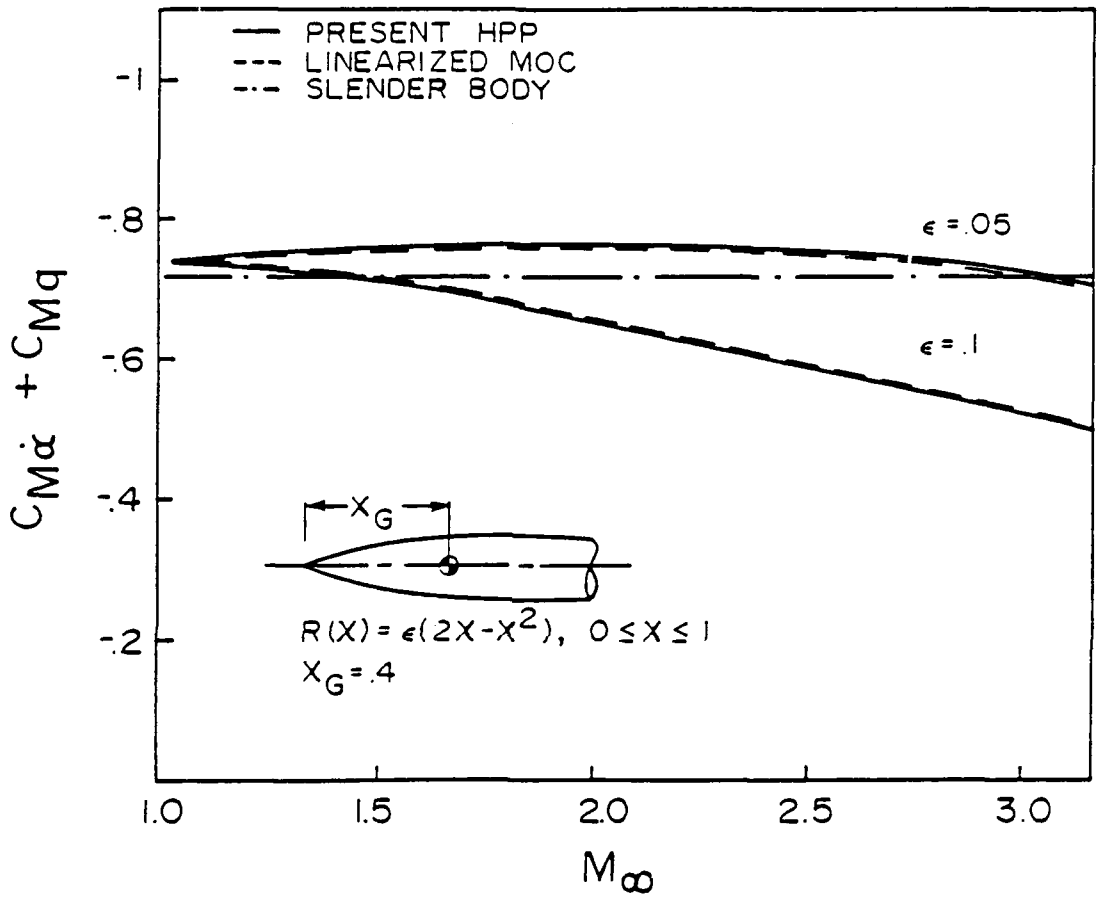

Fig. 19 Comparison of theoretical damping-in-pitch moment coefficients for a parabolic ogive at various Mach numbers.

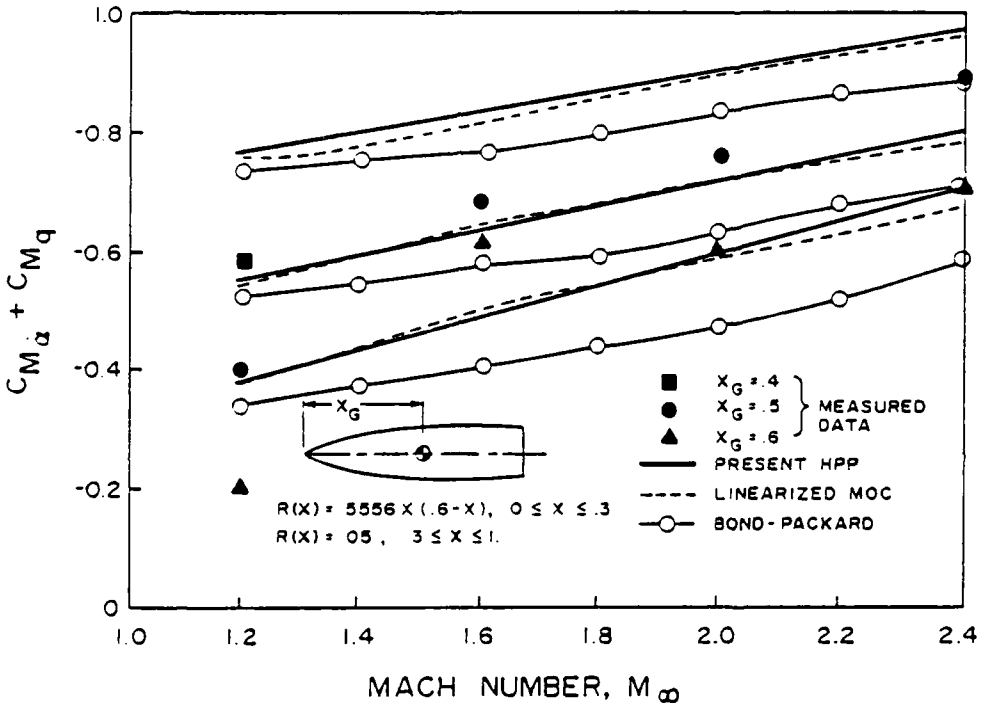

Fig. 20 Comparison of theoretical and experimental damping-in-pitch moment coefficients for a parabolic-ogive cylinder at various Mach numbers.

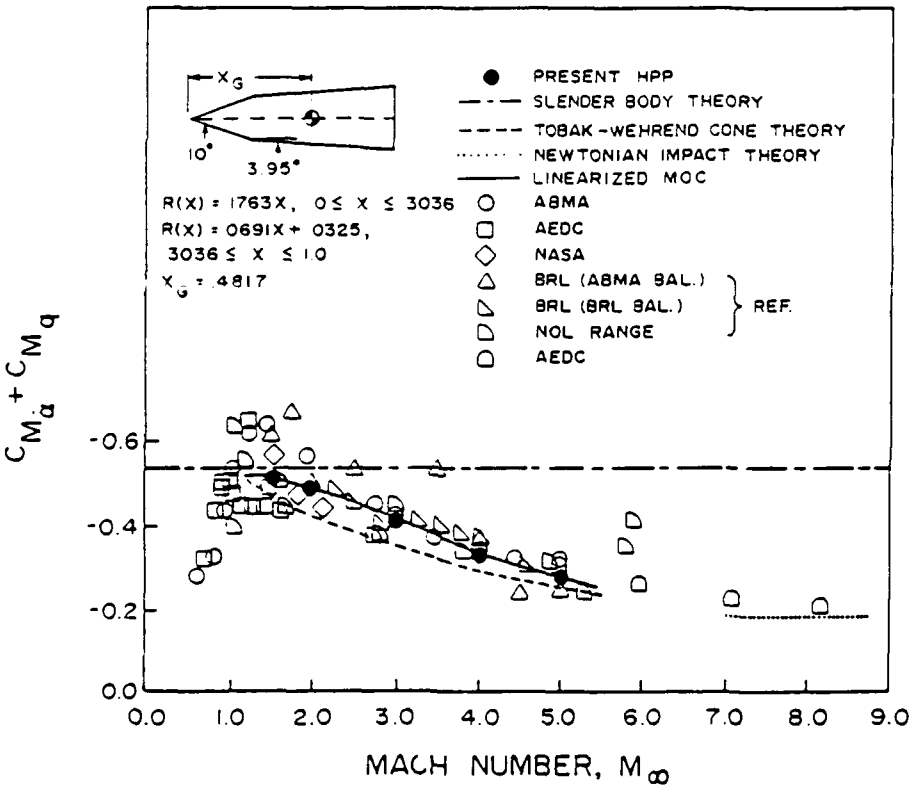

Fig. 21 Comparison of theoretical and experimental damping-in-pitch moment coefficients for a cone frustrum at various Mach numbers.

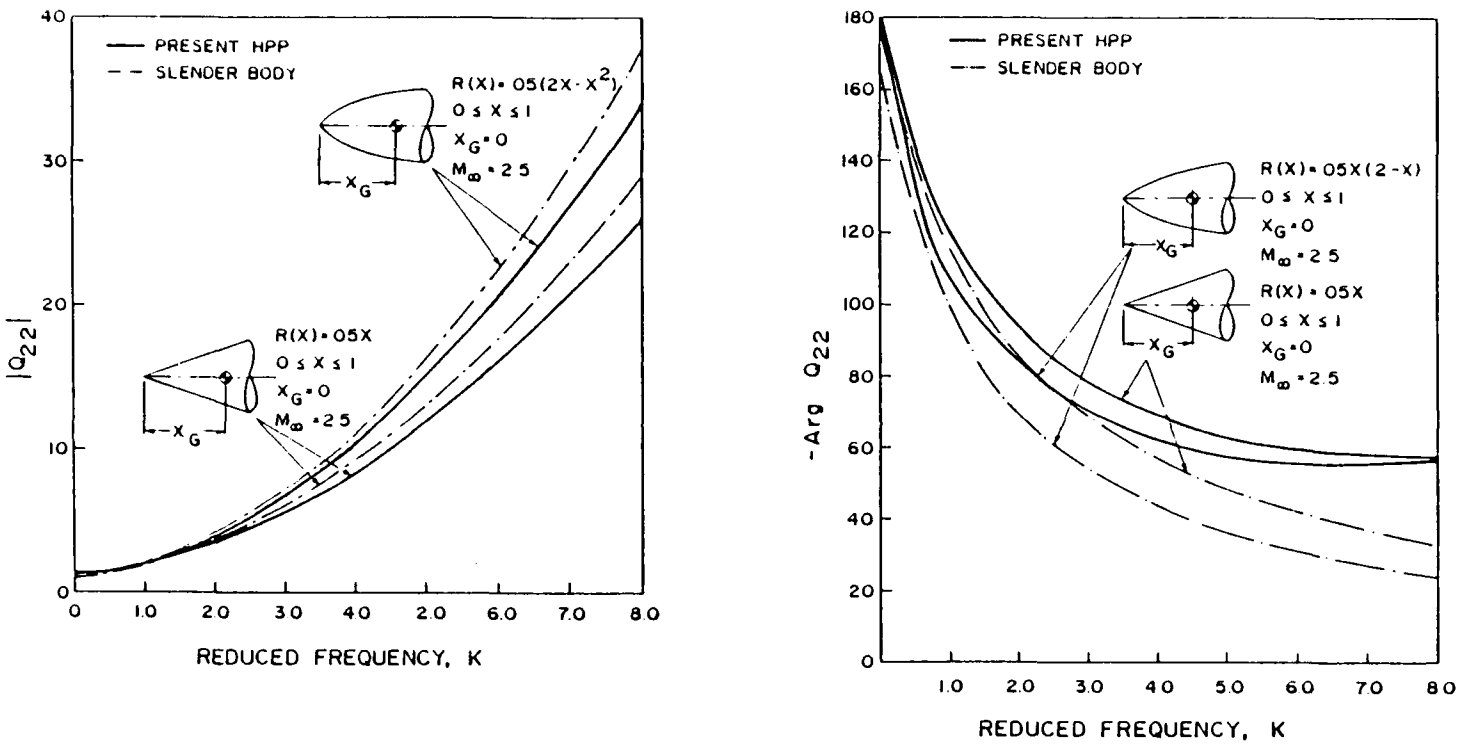

Fig. 22 Modulus and argument of the generalized forces versus reduced frequency for a cone and a parabolic ogive in pitching mode at M_∞=2.5.

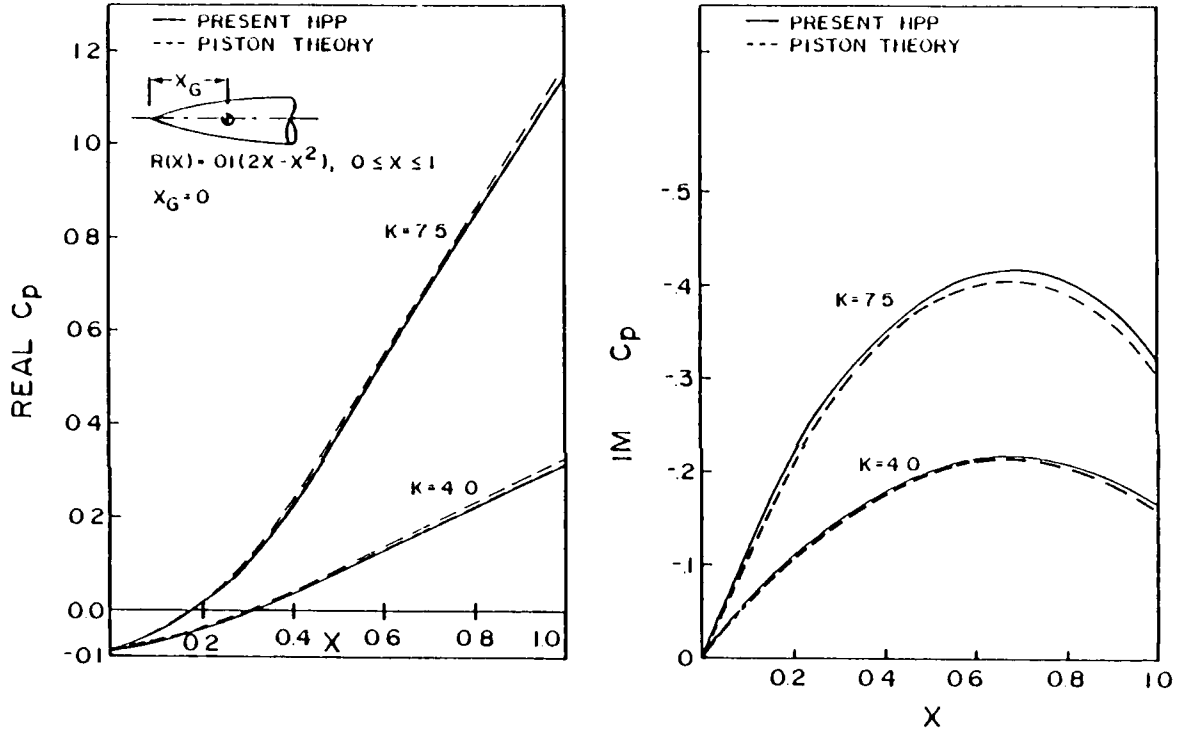

Fig. 23 In-phase and out-of-phase pressure coefficients for a parabolic ogive in pitching mode at M_∞=1.5 and high reduced frequencies.

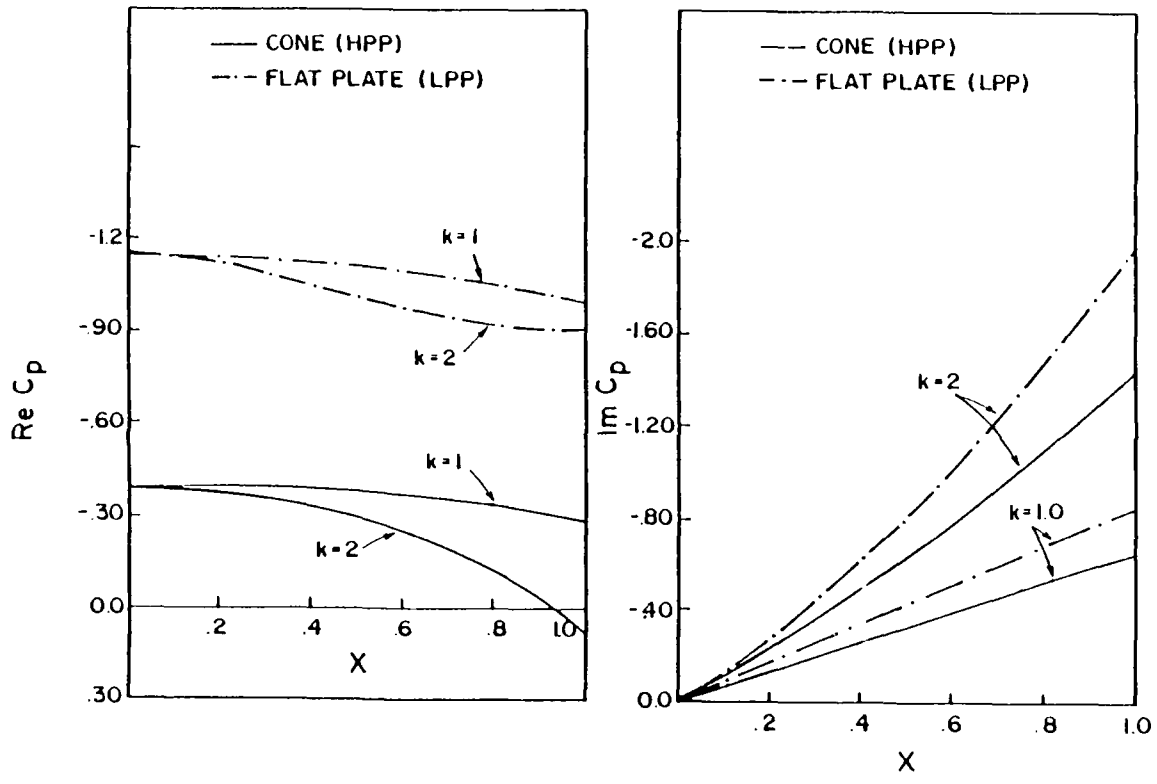

Fig. 24 Comparison of the in-phase and out-of-phase pressure coefficients at M_∞=1.5 for a 5.7° cone and a flat plate pitching at the apex.

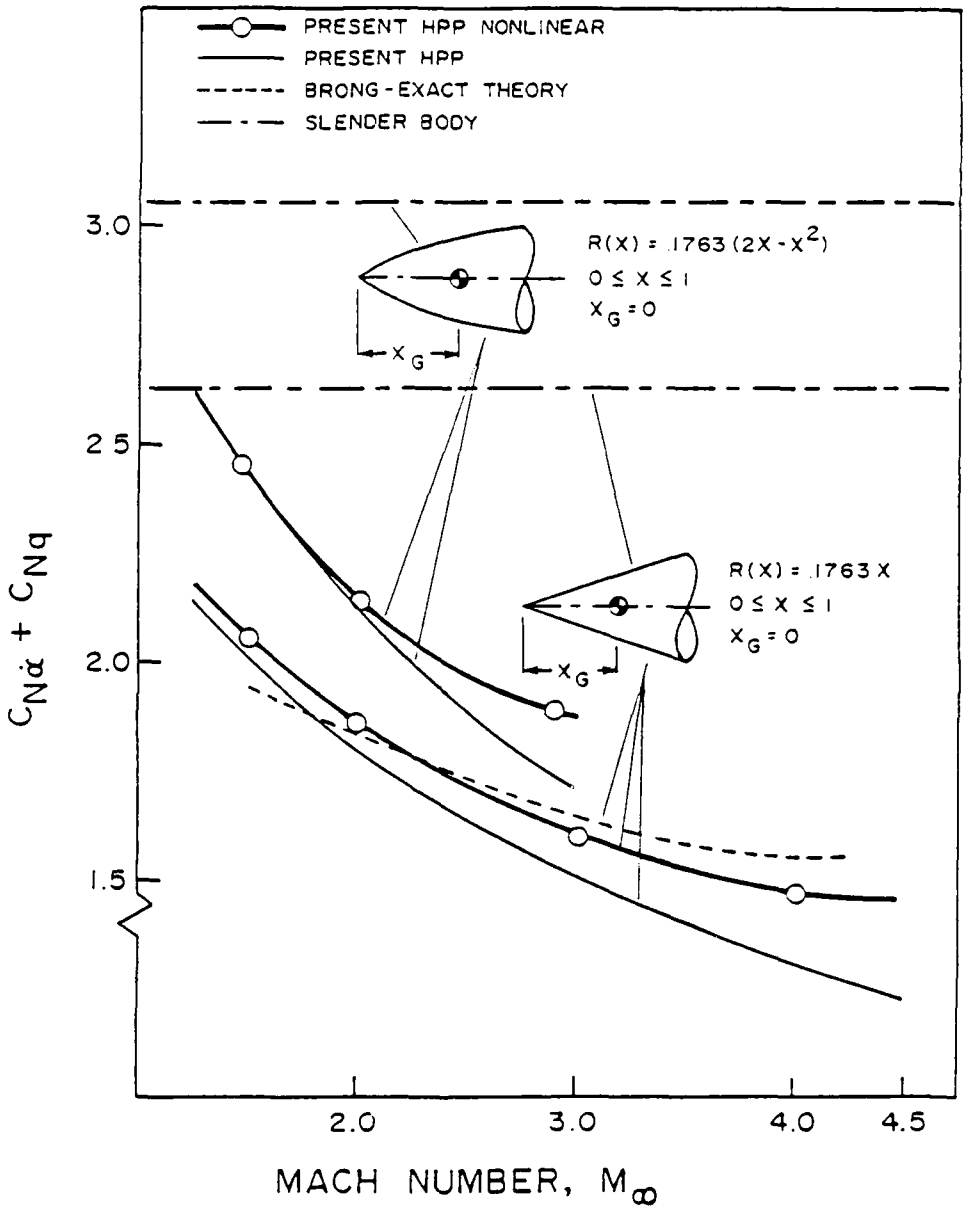

Fig. 25 Damping-in-pitch normal force coefficients versus Mach number for a cone and a parabolic-ogive.

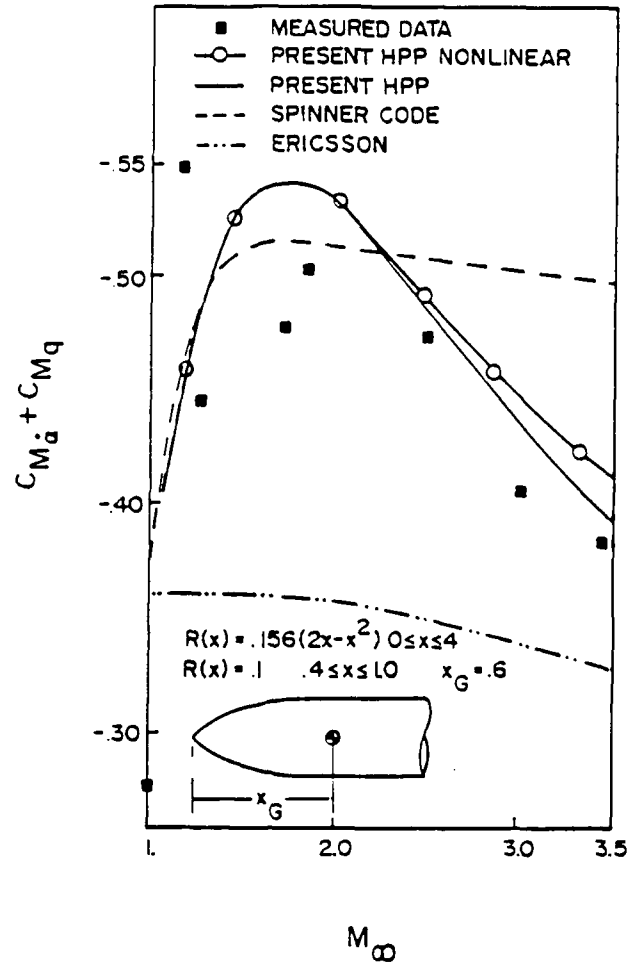

Fig. 26 Damping-in-pitch moment coefficient for a parabolic-ogive-cylinder at various Mach numbers.

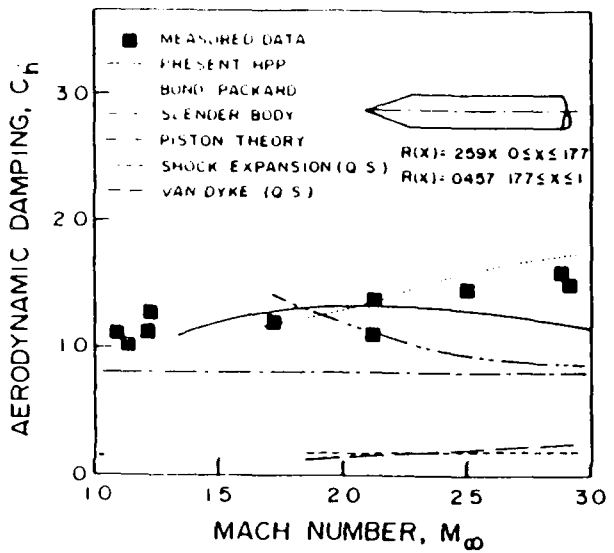

a) Vibrating in first bending mode.

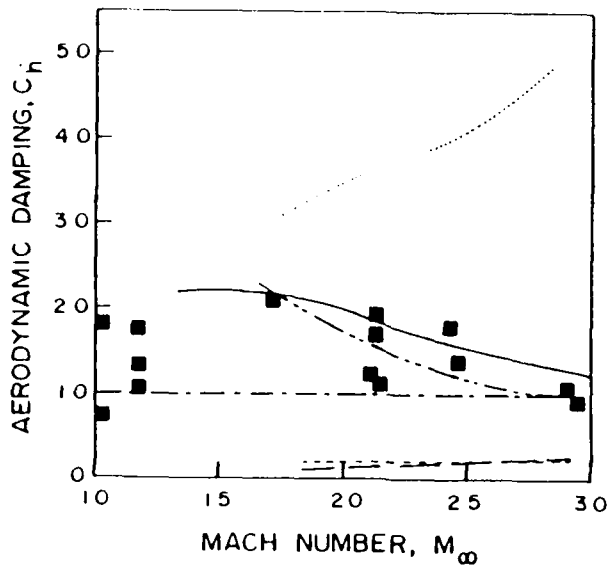

b) Vibrating in second bending mode.

Fig. 27 Aerodynamic damping coefficient versus Mach number, for a cone cylinder

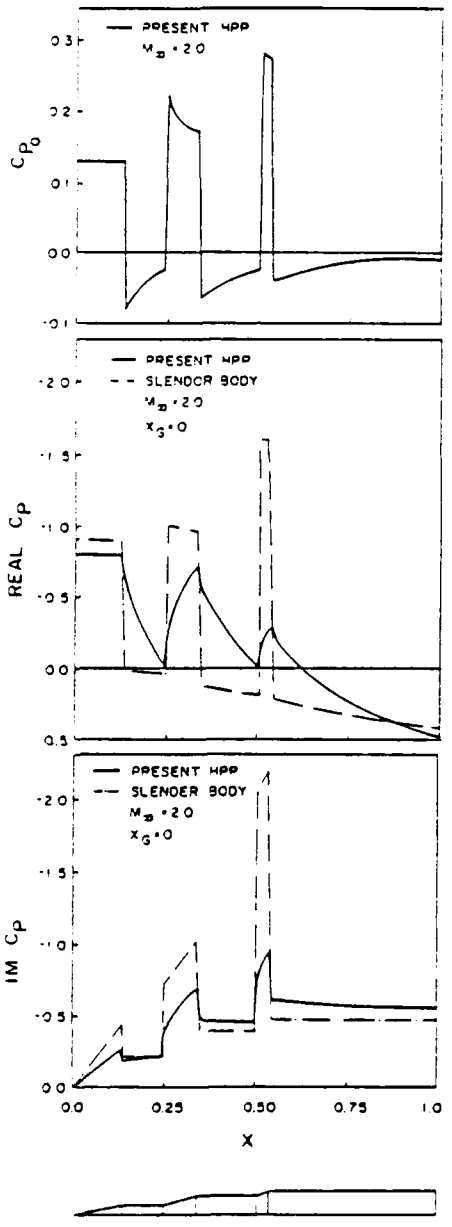

a) Mean flow pressure.

b) In-phase pressure.

c) Out-out-phase pressure.

Fig. 28 Pressure coefficients for a Saturn SA-1 configuration at M_∞=2.0, reduced frequency k=1.8 and center of rotation at the apex.

SATURN SA-I MODEL

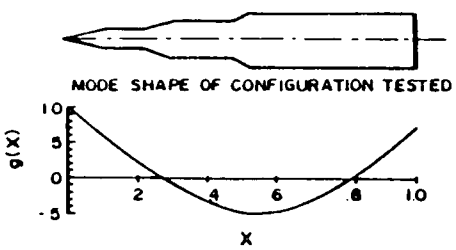

GEOMETRY OF THE CONFIGURATION

R(X)= .2296 X	0 ≤ X ≤ .1317
R(X)= .03024	.1317 ≤ X ≤ .241
R(X)= .268X-.03445	.241 ≤ X ≤ .3353
R(X)= .05541	.3353 ≤ X ≤ .5066
R(X)= .4515X-.17332	.5066 ≤ X ≤ .5288
R(X)= .06543	.5288 ≤ X ≤ 1.0

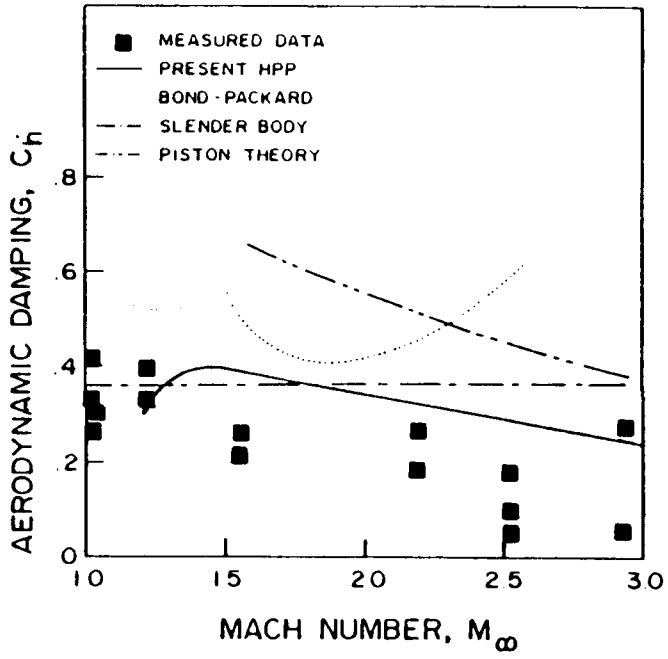

Fig. 29 Comparison of computed and experimental aerodynamic damping coefficients versus Mach number for a Saturn SA-1 configuration vibrating in first bending mode.

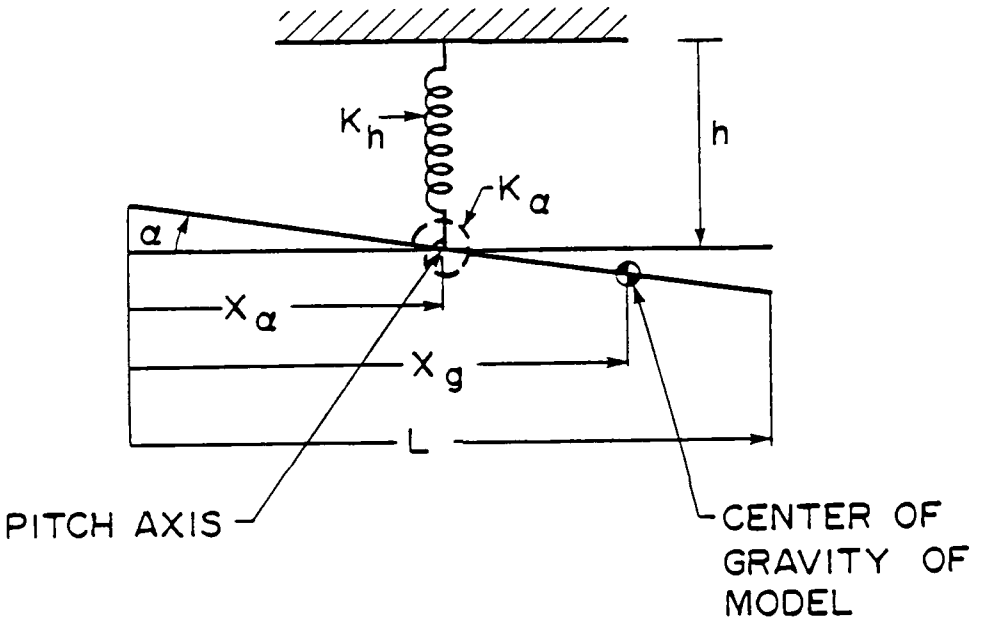

Fig. 30 Schematic view of body in pitching and plunging motion.

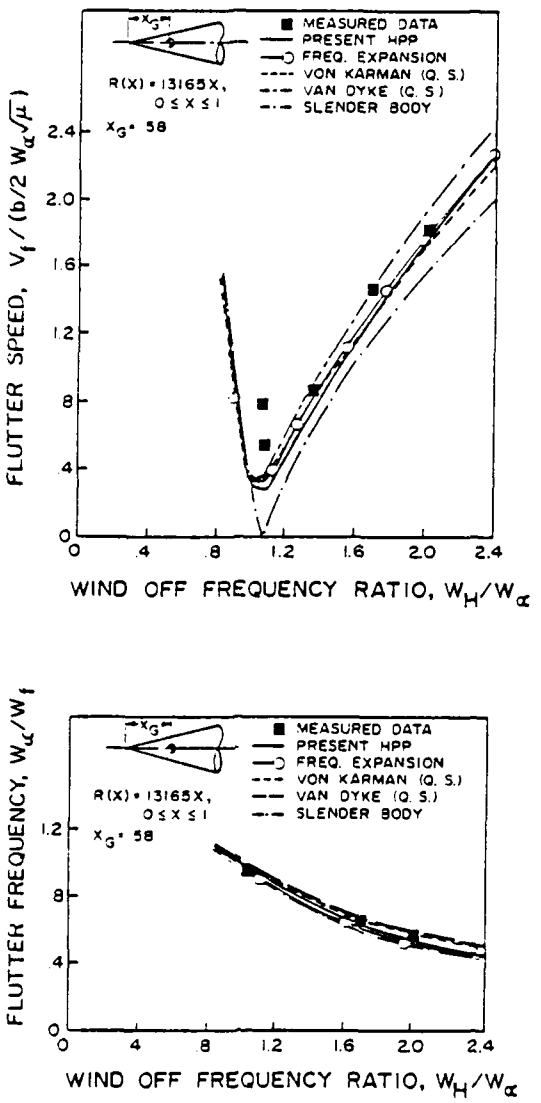

Fig. 31 Flutter boundaries for a 7.5° cone at M_∞=2.0.

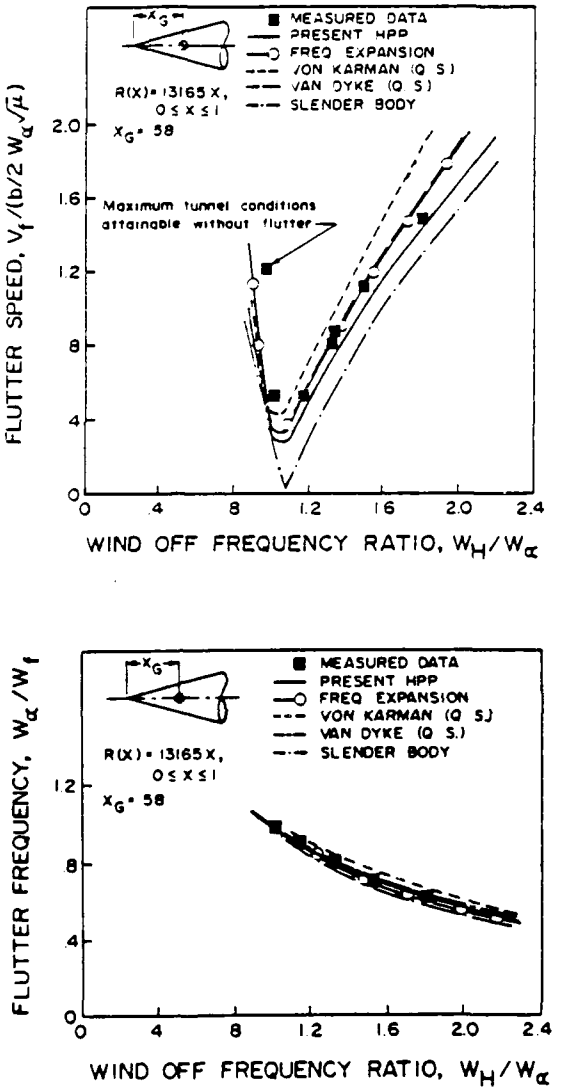

Fig. 32 Flutter boundaries for a 7.5° cone at M_∞=3.0.

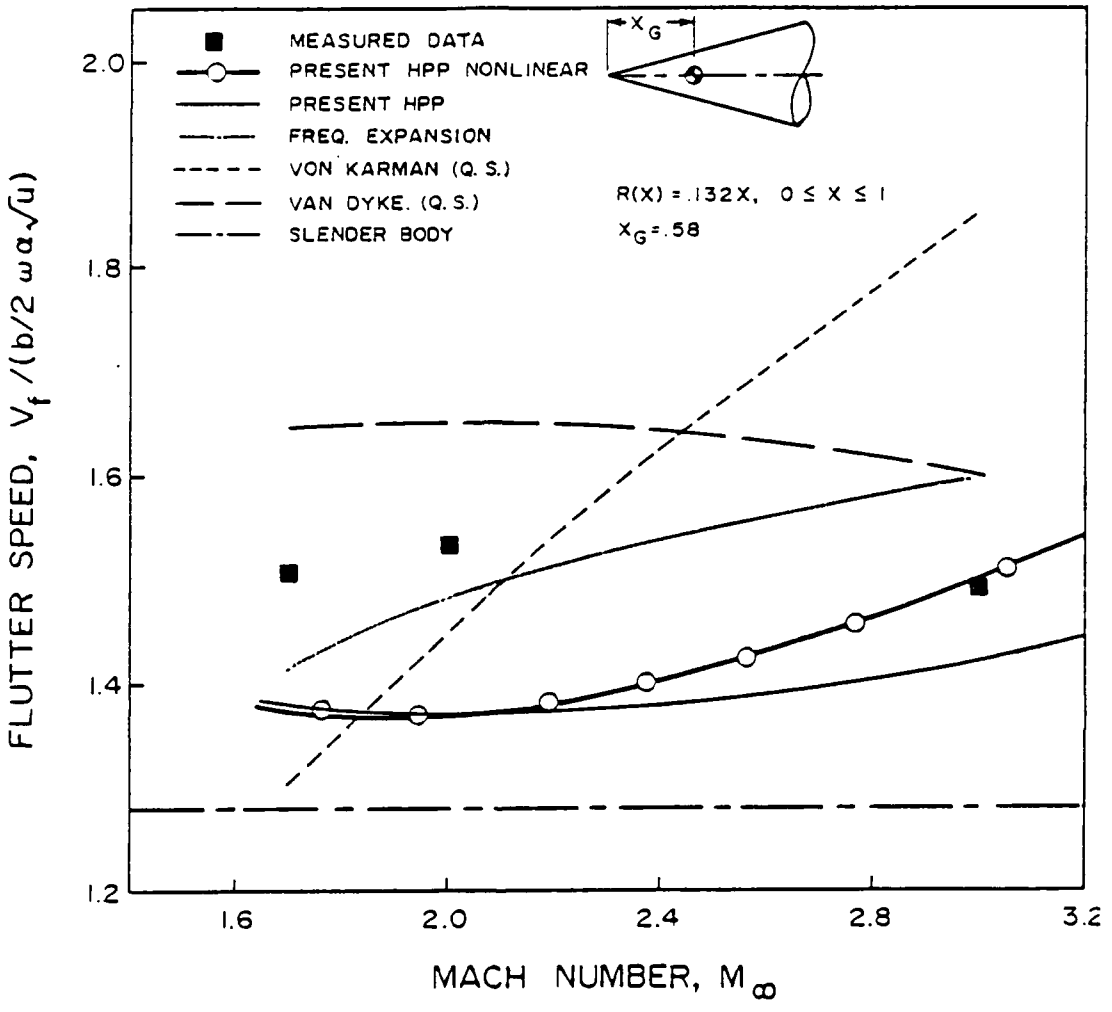

Fig. 33 Flutter speed boundaries versus Mach number for a 7.5° cone.

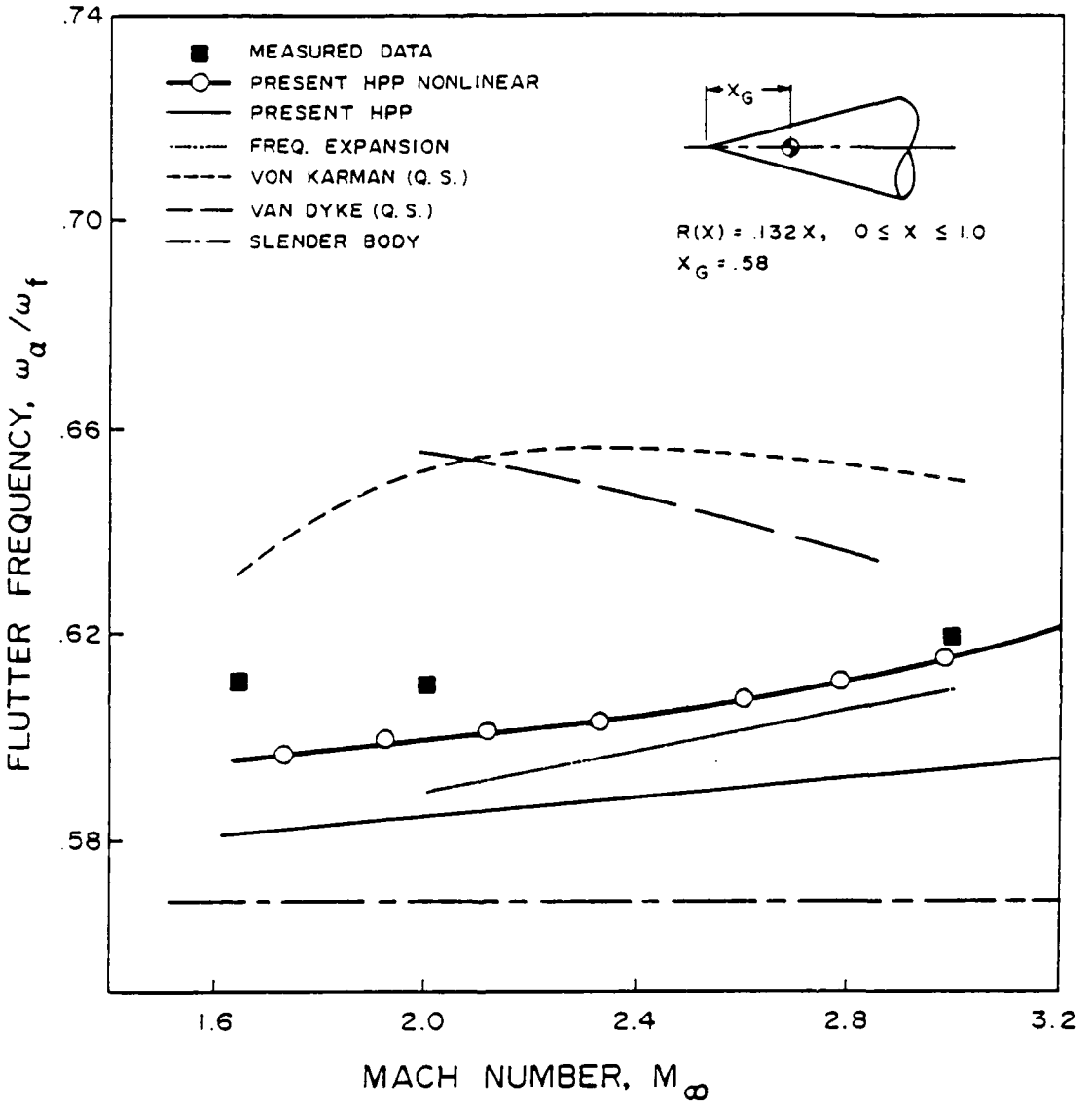

Fig. 34 Flutter frequency boundaries versus Mach number for a 7.5° cone.

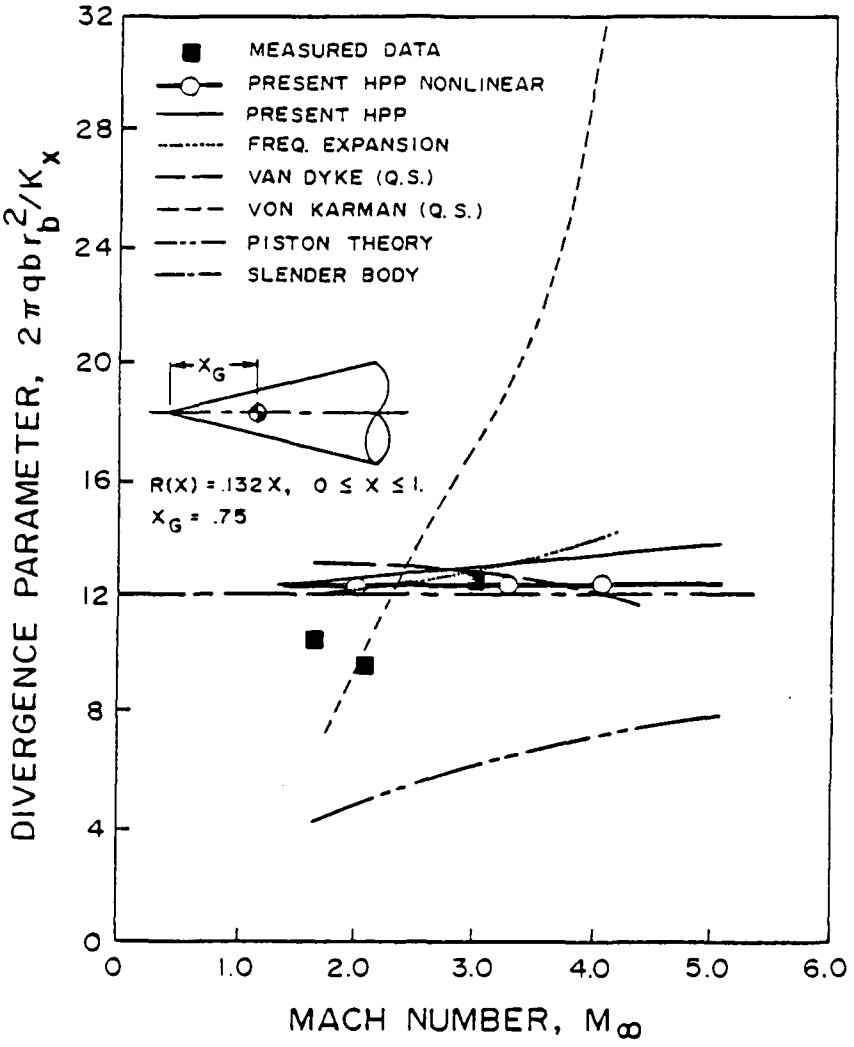

Fig. 35 Divergence boundaries versus Mach number for a 7.5° cone.

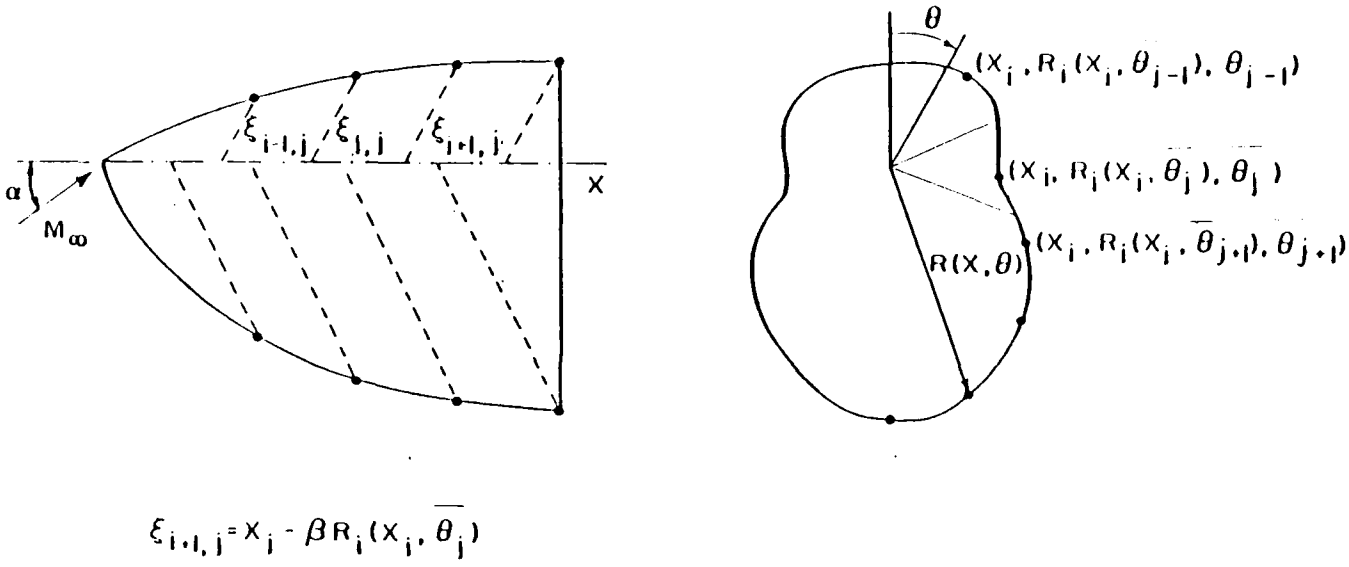

$$\xi_{i+1,j} = X_j - \beta R_i(X_i, \bar{\theta}_j)$$

Fig. 36 Panel and control points arrangement for asymmetric bodies.

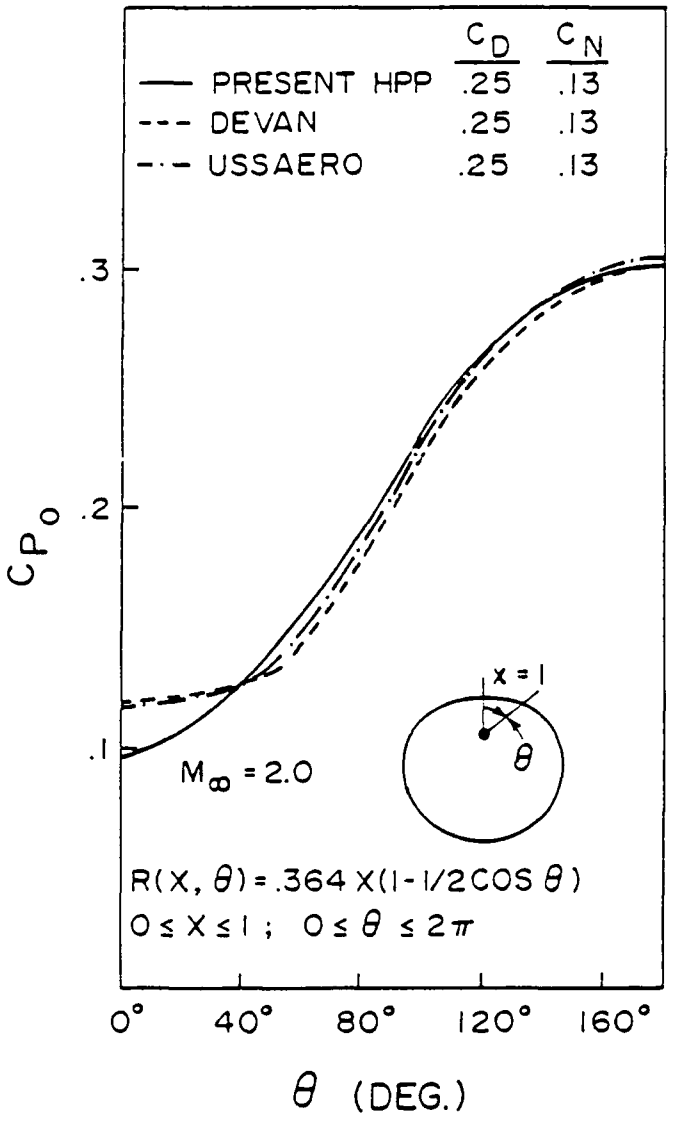

Fig. 37 Pressure coefficient for an asymmetric cone at M_∞=2.0, α=0 deg.

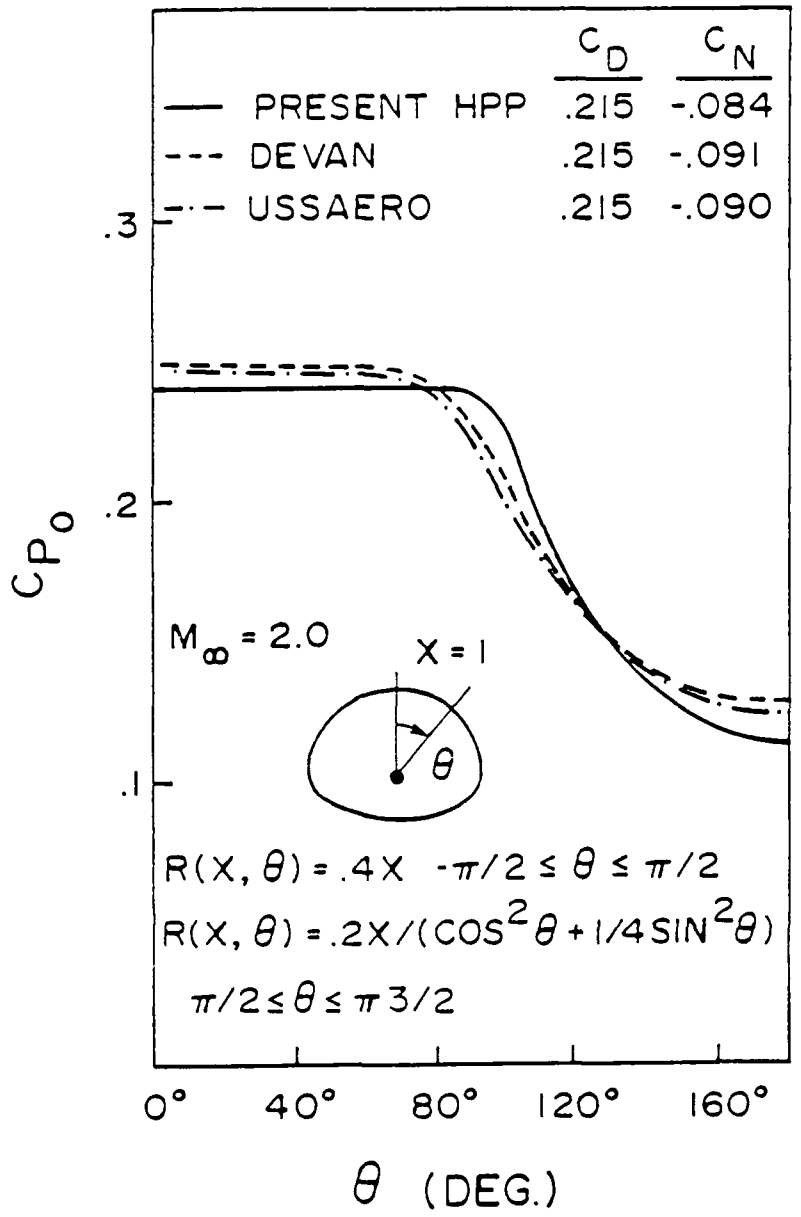

Fig. 38 Pressure coefficient for a half circle; half ellipse cone at M_∞=2.0, α=0 deg.

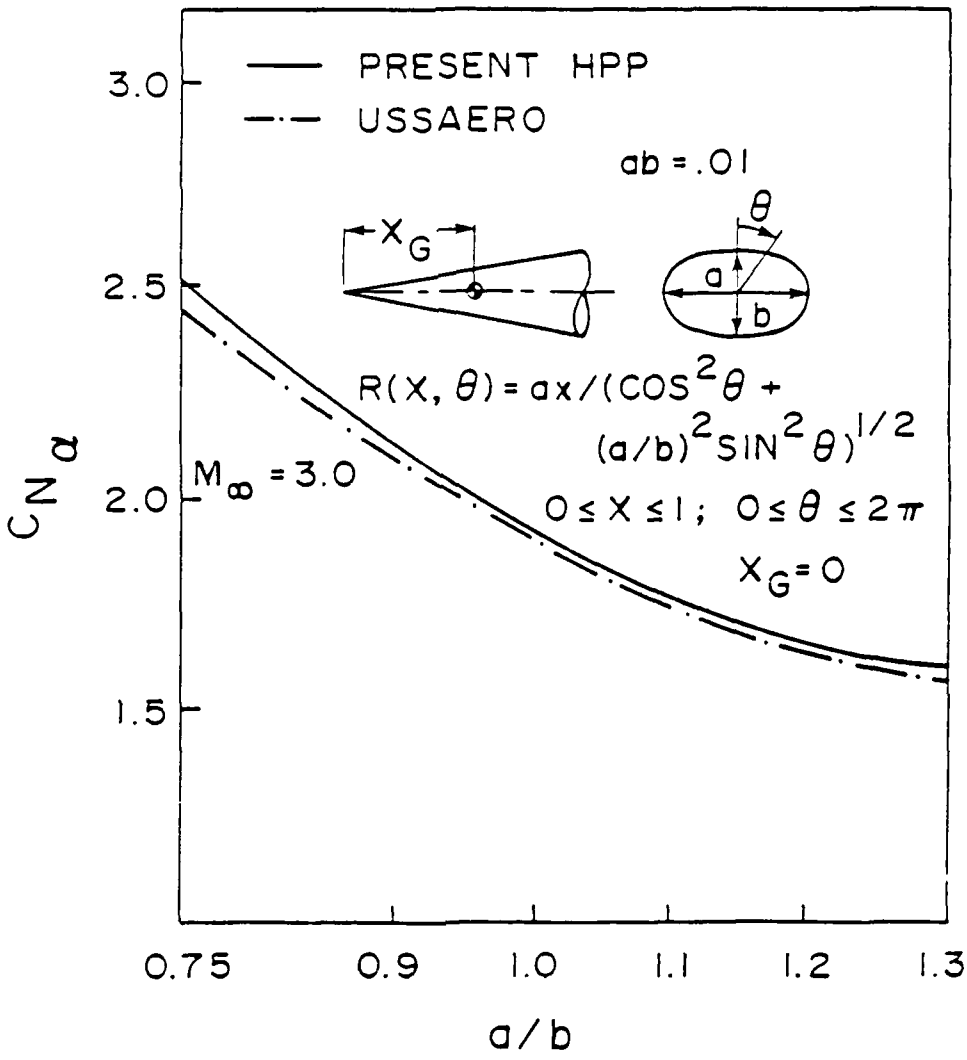

Fig. 39 Normal-force coefficient for elliptic cones versus the ellipticity ratio a/b at M_∞=3.0.

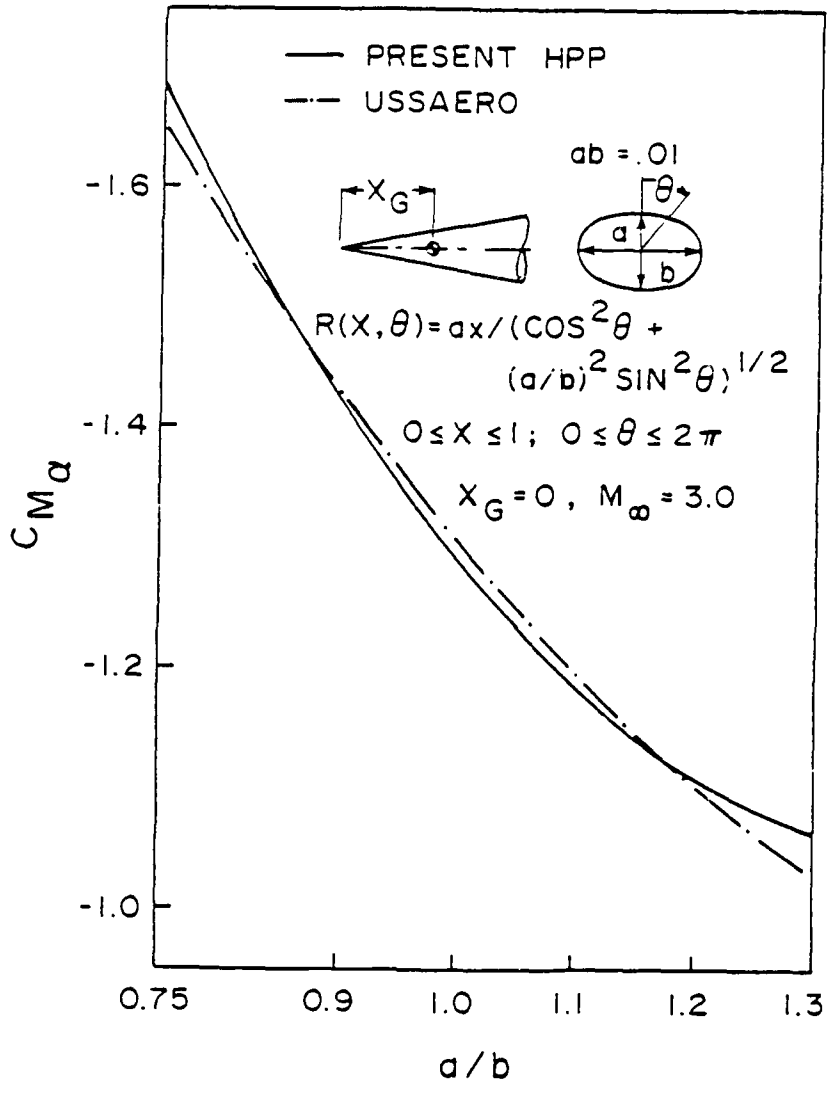

Fig. 40 Pitching moment coefficient for elliptic cones versus the ellipticity ratio a/b at M_∞=3.0.

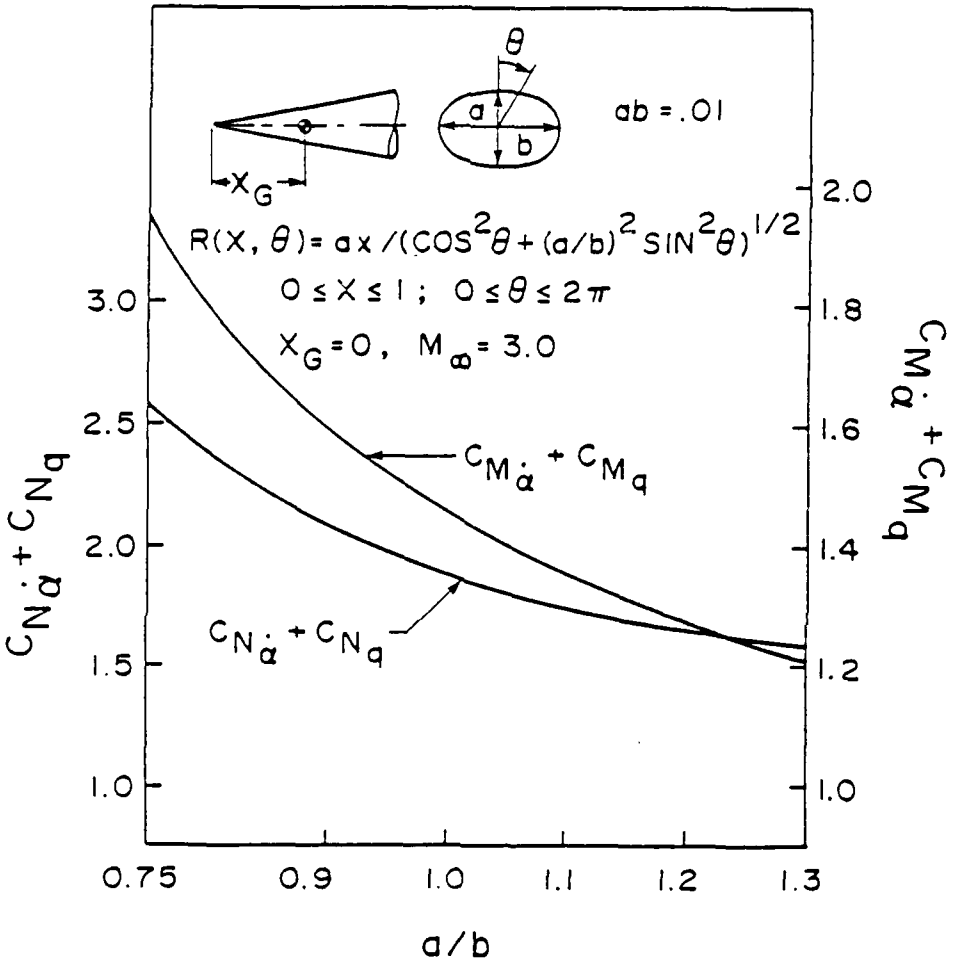

Fig. 41 Damping-in-pitch normal force coefficient and damping-in-pitch moment coefficient for elliptic cones versus the ellipticity ratio a/b at M_∞=3.0.

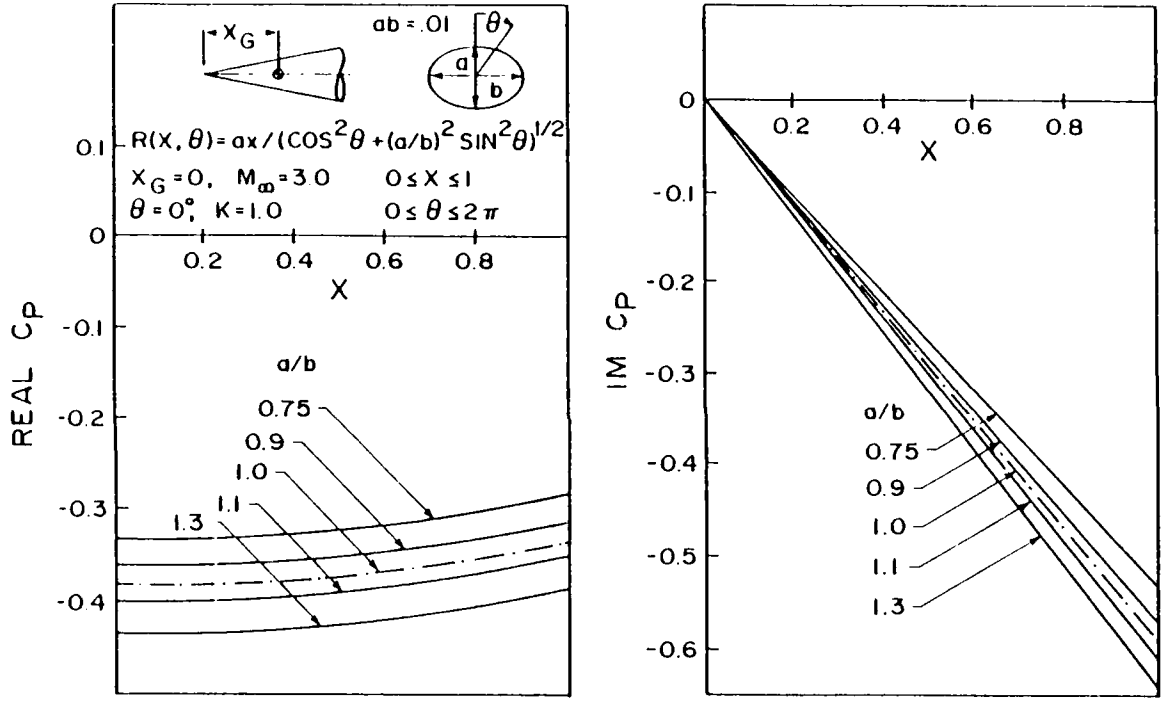

Fig. 42 In-phase and out-of-phase pressure coefficient for elliptic cones in pitching mode at $M_\infty = 3.0$ and reduced frequency k=1.0 along the x-axis.

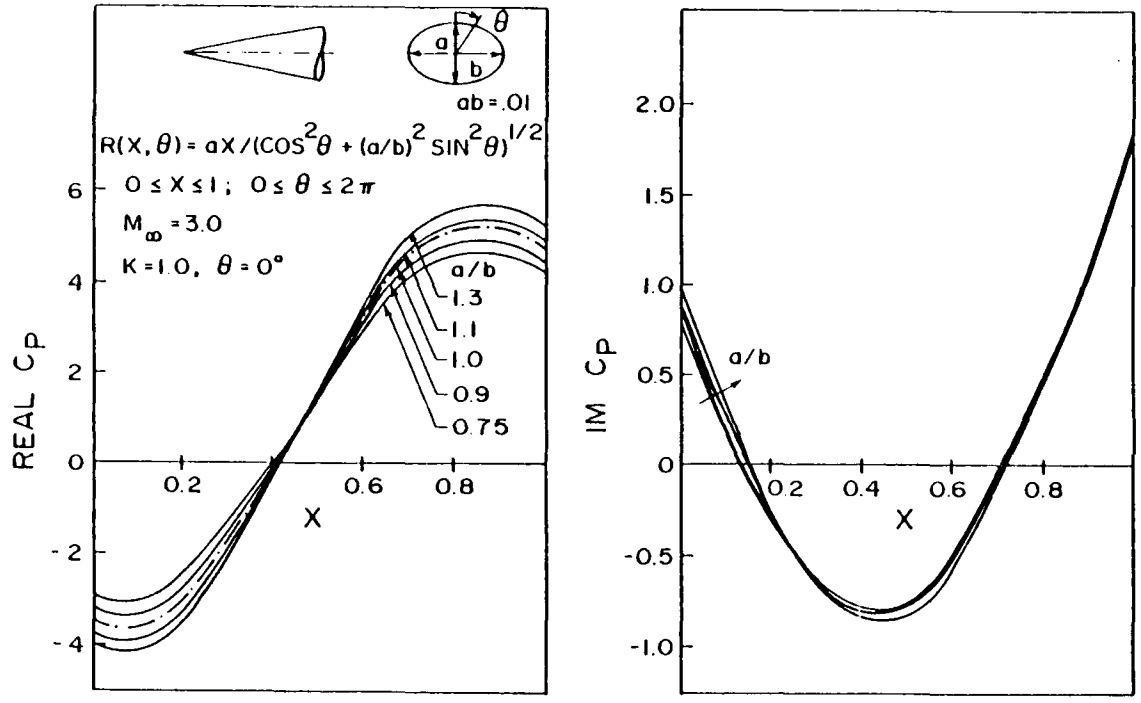

Fig. 43 In-phase and out-of-phase pressure coefficient for elliptic cones in first bending mode at M_∞=3.0 and reduced frequency k=1.0 along the x-axis.

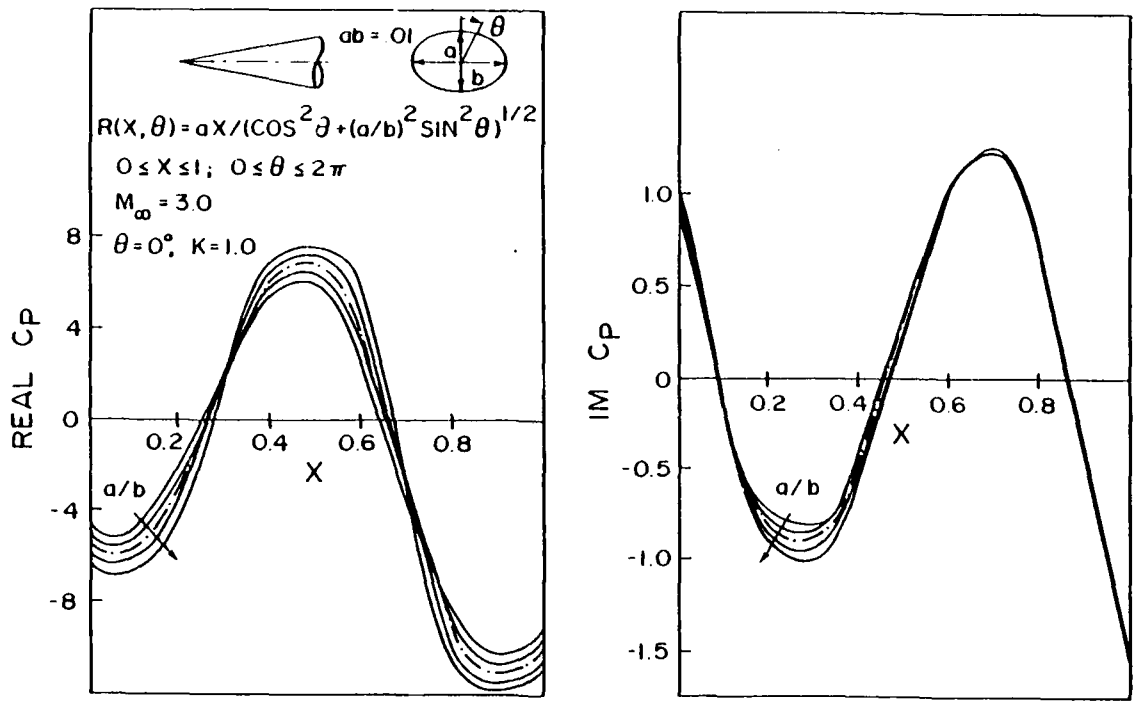

Fig. 44 In-phase and out-of-phase pressure coefficient for elliptic cones in second bending mode at M_∞=3.0 and reduced frequency k=1.0 along the x-axis.

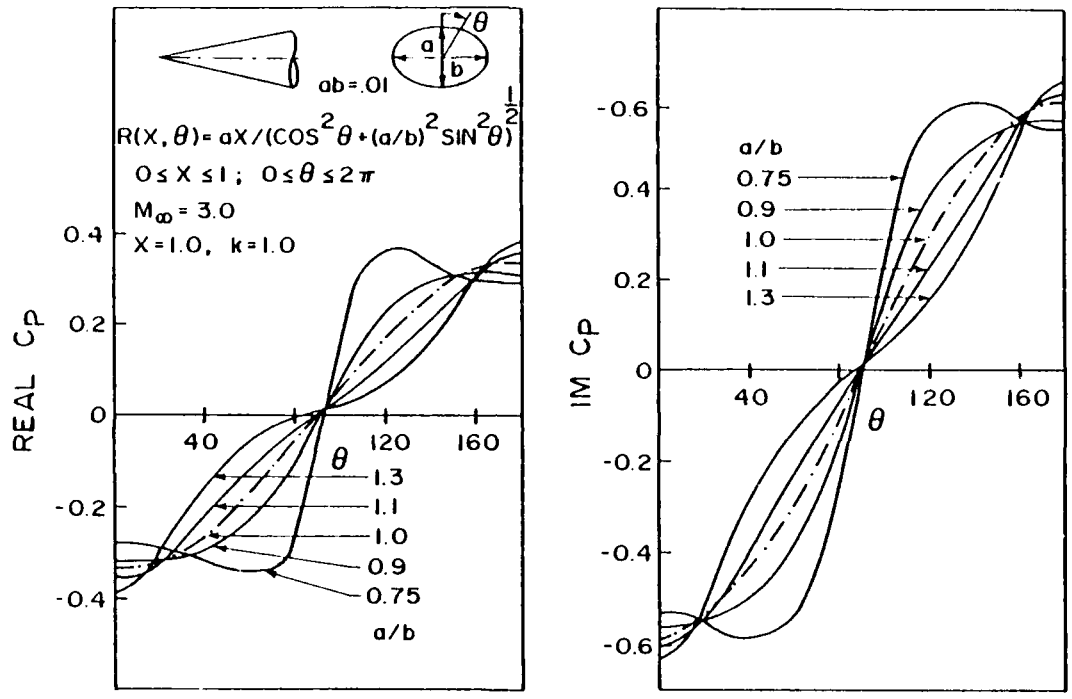

Fig. 45 In-phase and out-of-phase pressure coefficient for elliptic cones in pitching mode at M_∞=3.0 and reduced frequency k=1.0 along the polar angle θ

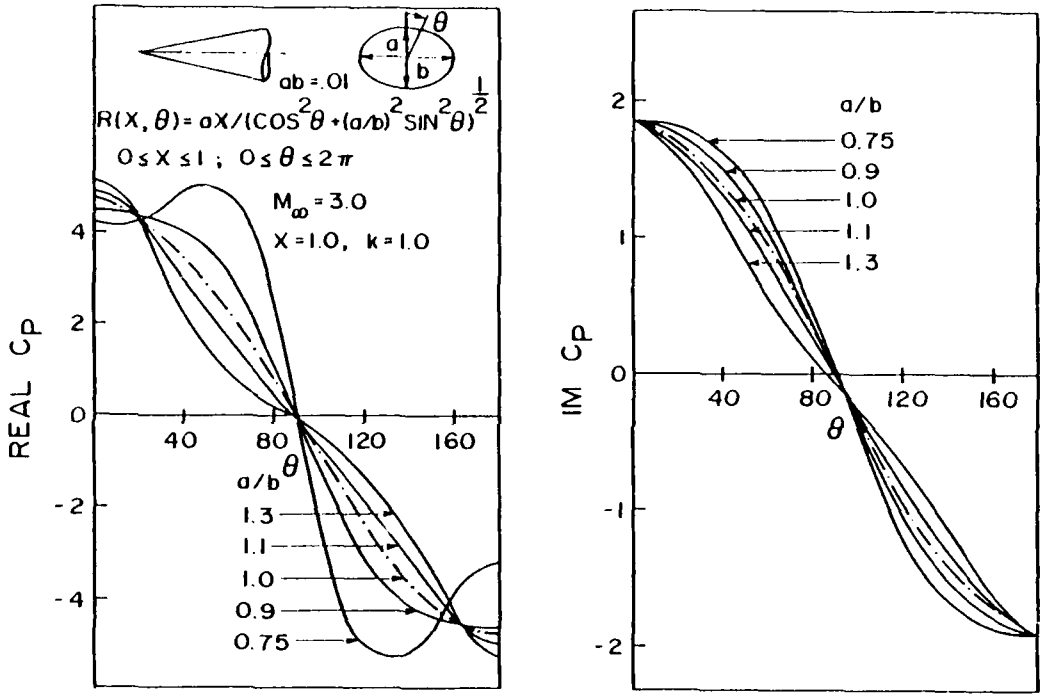

Fig. 46 In-phase and out-of-phase pressure coefficient for elliptic cones in first bending mode at M_∞=3.0 and reduced frequency k=1.0 along the polar angle θ.

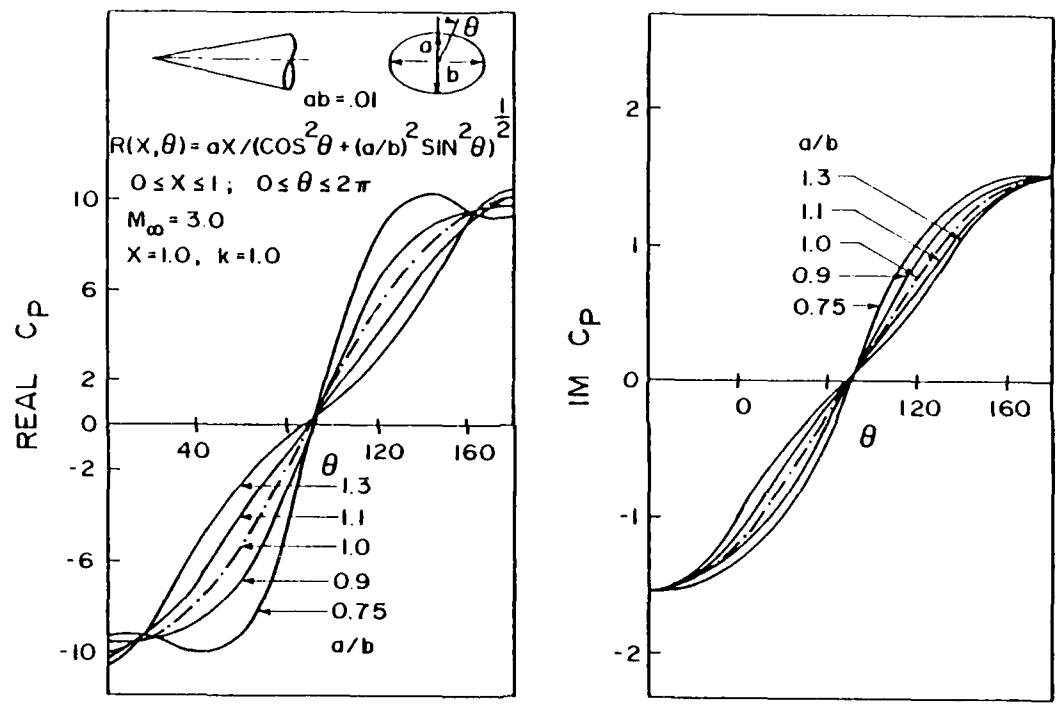

Fig. 47 In-phase and out-of-phase pressure coefficient for elliptic cones in second bending mode at M_∞=3.0 and reduced frequency k=1.0 along the polar angle θ.

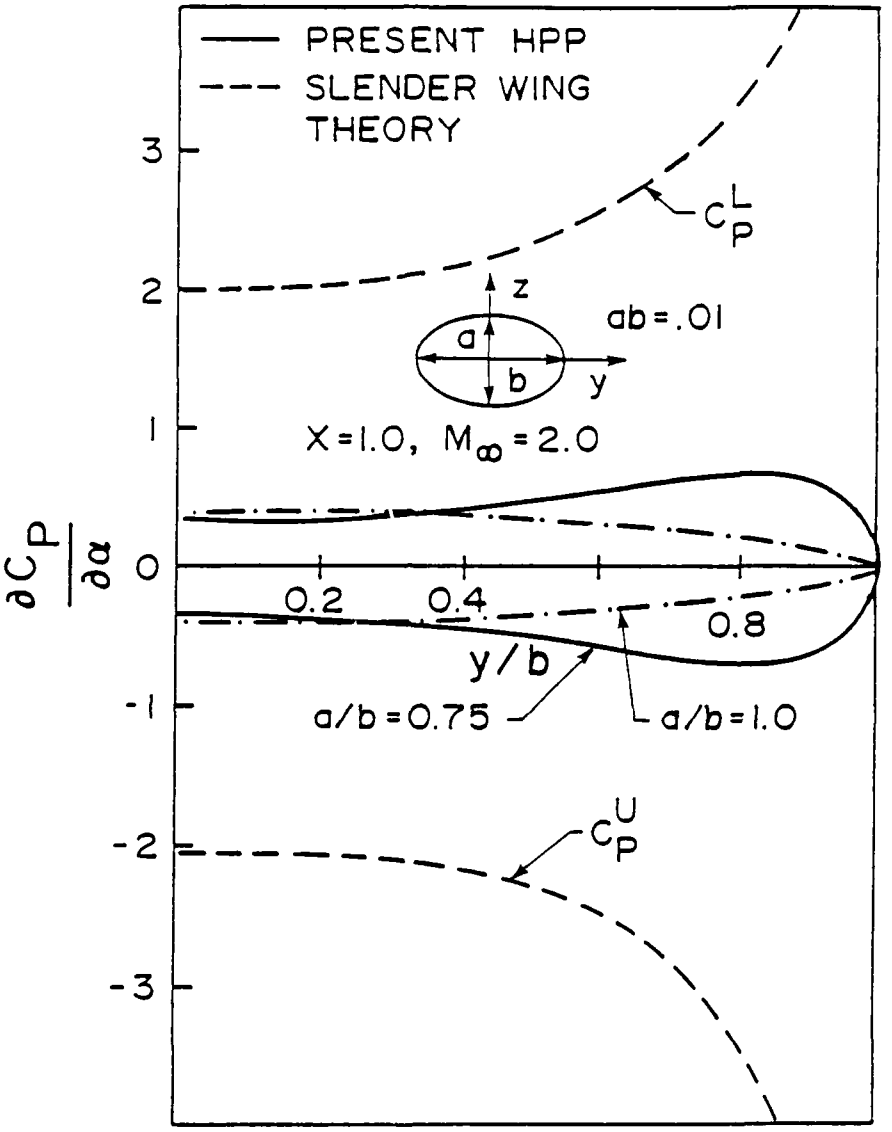

Fig. 48 Pressure distribution per unit angle of attack along the y-axis for a circular cone, elliptic cone and a flat plate at M_∞=2.0.

BUNDLED TRIPLET (BTM) METHOD FOR SUPERSONIC FLOW

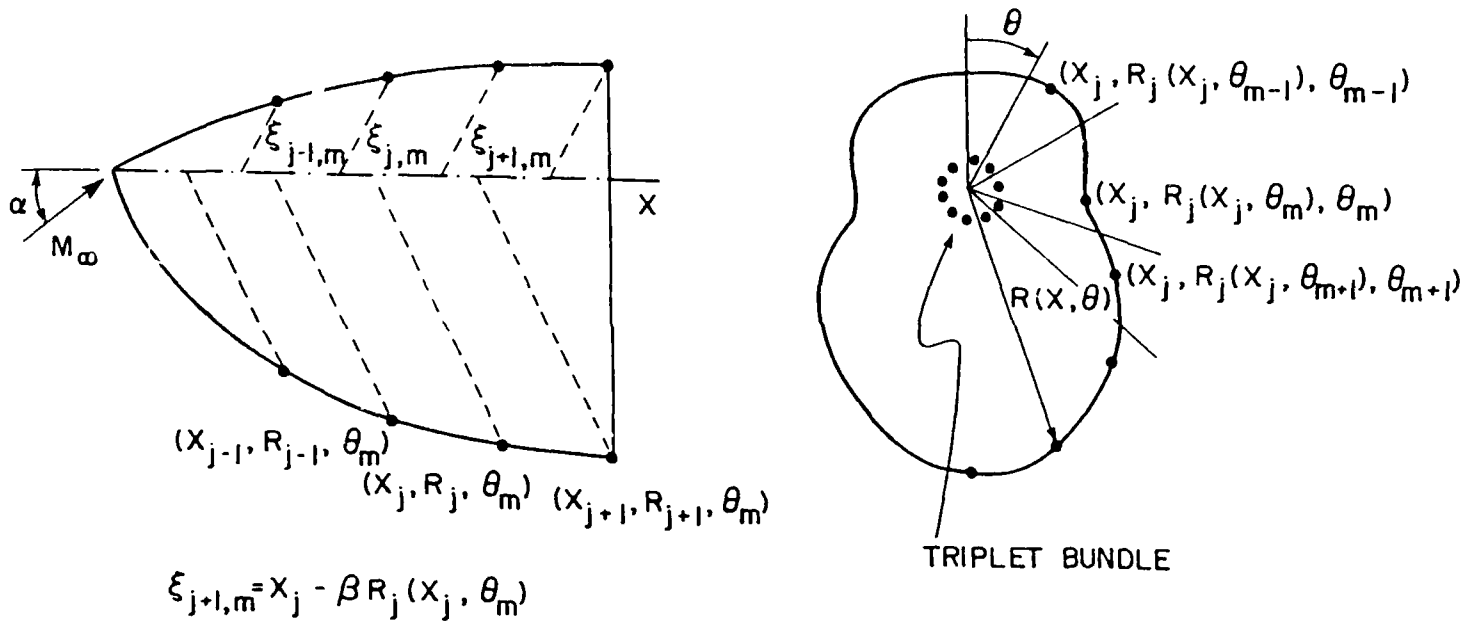

Fig. 49. Sketch Showing Bundled Triplet Arrangements.

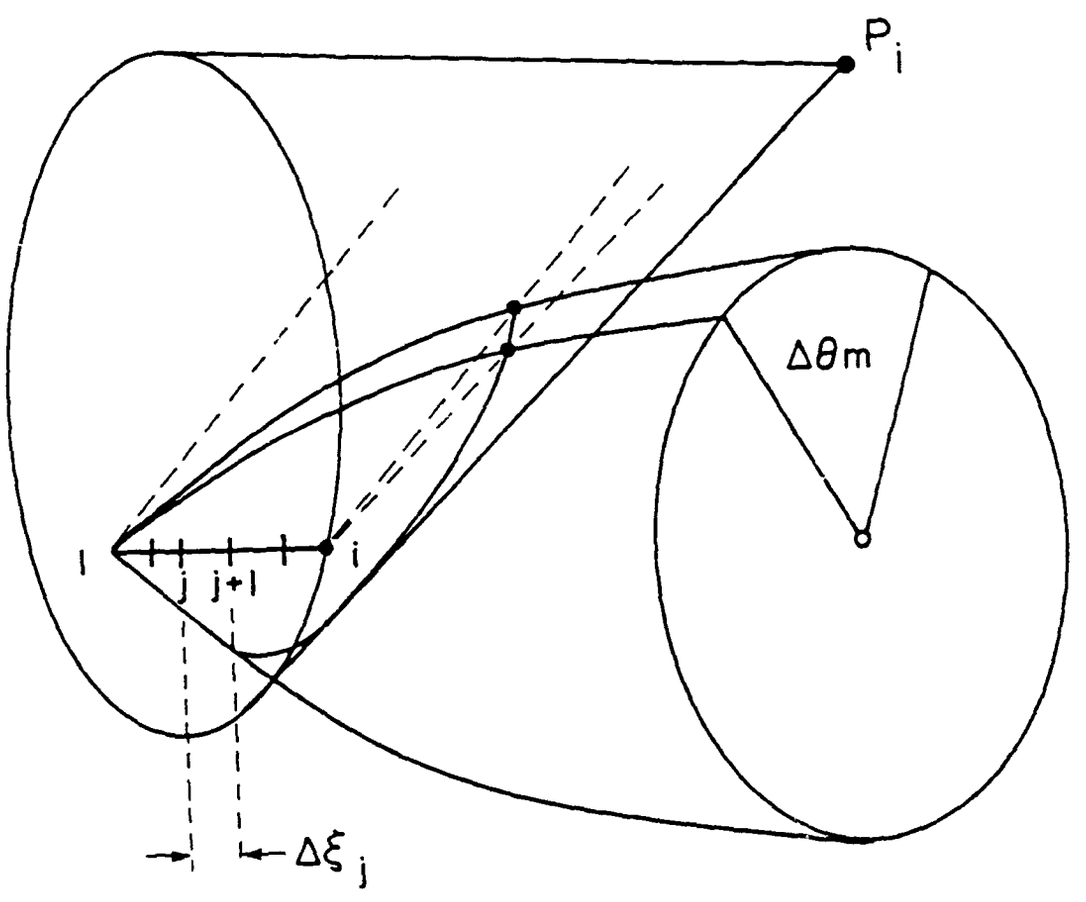

Fig. 50. Sketch Showing the Domain of Influence Based on the Bundled Triplet Method.

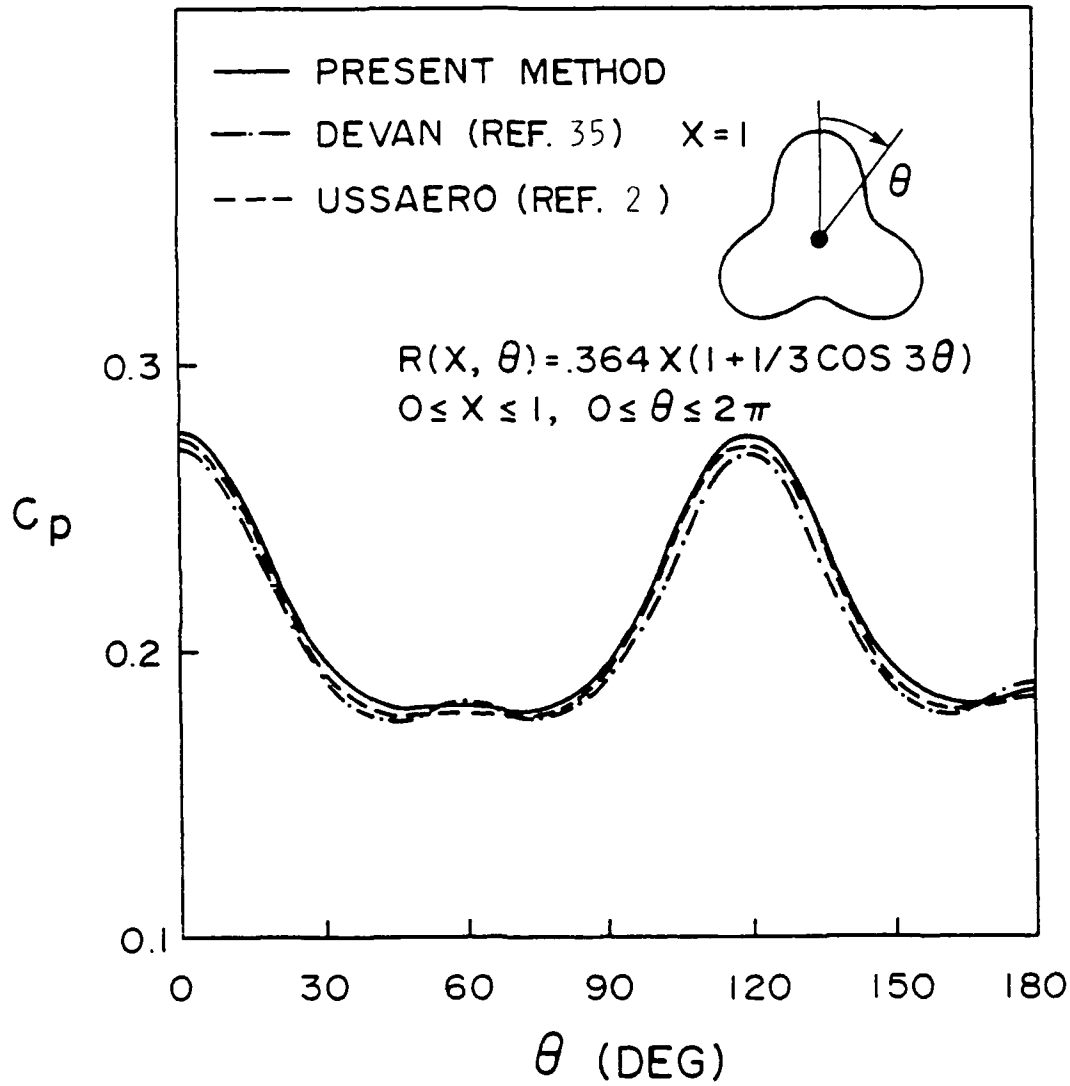

Fig. 51 Steady Pressure Distributions for an Asymmetric Cone at M_∞ = 2.0 and Angle of Attack α = 0°.

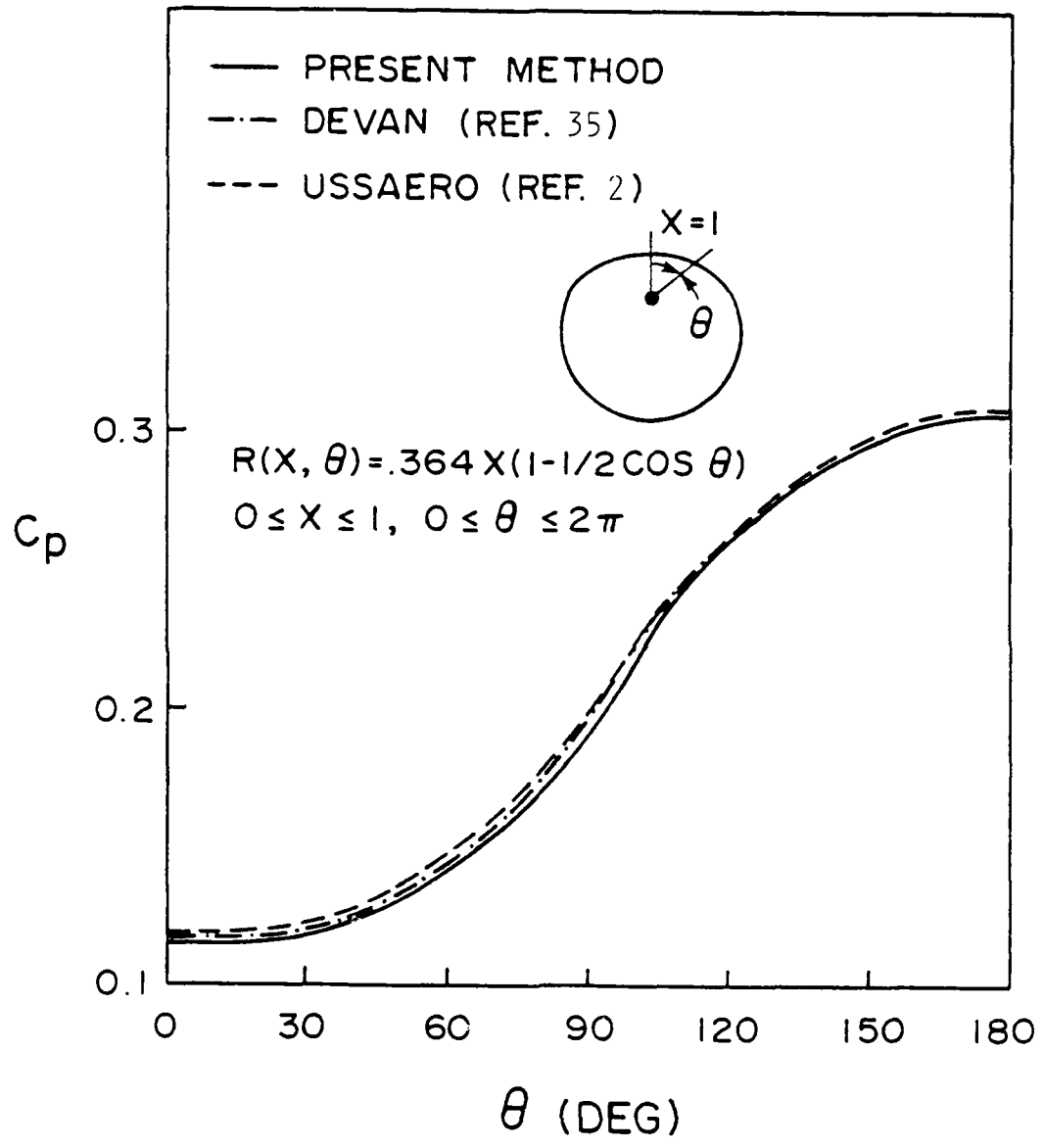

Fig. 52 Steady Pressure Distributions for an Asymmetric Cone at M_∞ = 2.0 and Angle of Attack α = 0°.

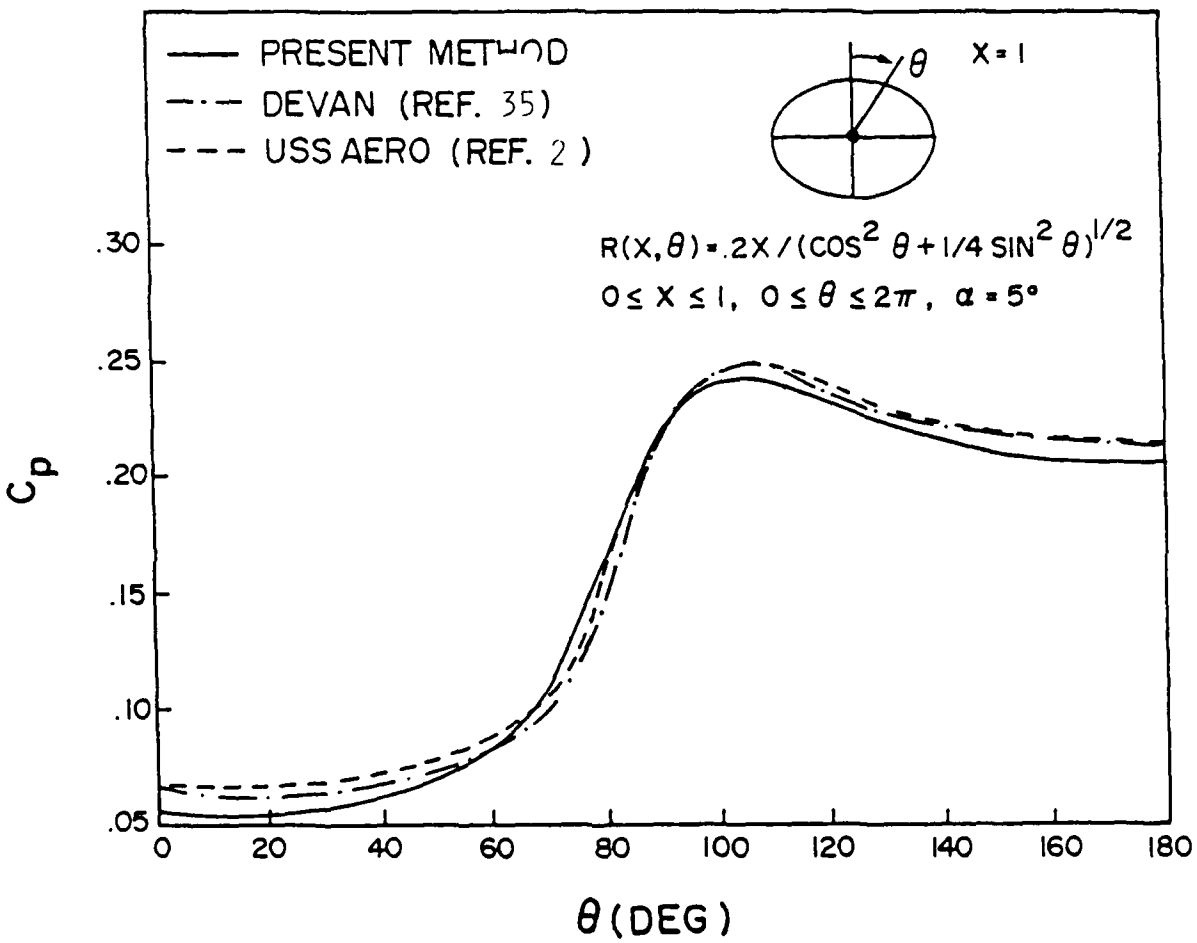

Fig. 53 Steady Pressure Distributions for an Elliptic Cone at M_∞ = 2.0 and Angle of Attack α = 5°.

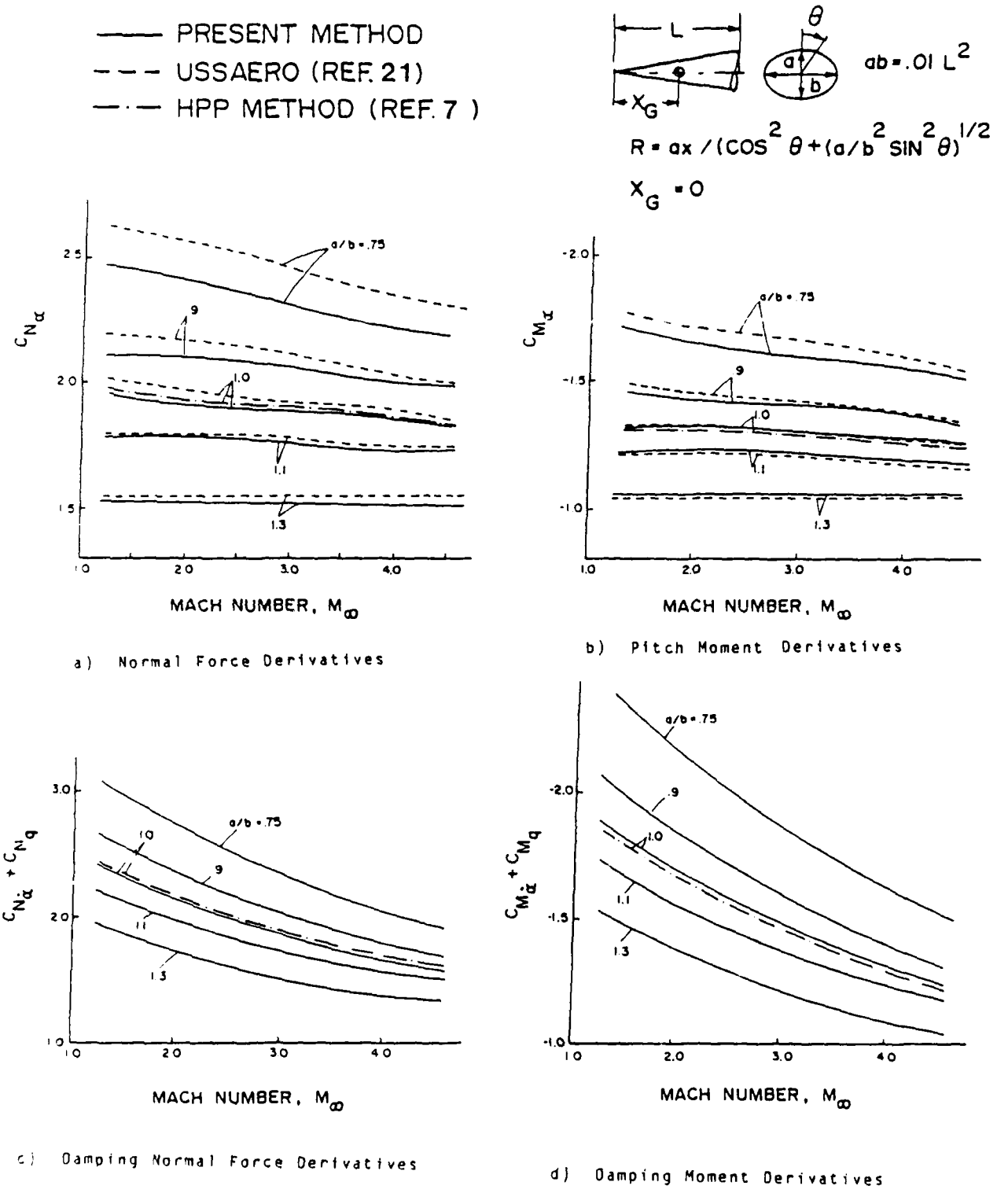

Fig. 54 Stability Derivatives of a Family of Elliptic Cones at Various Mach Numbers.

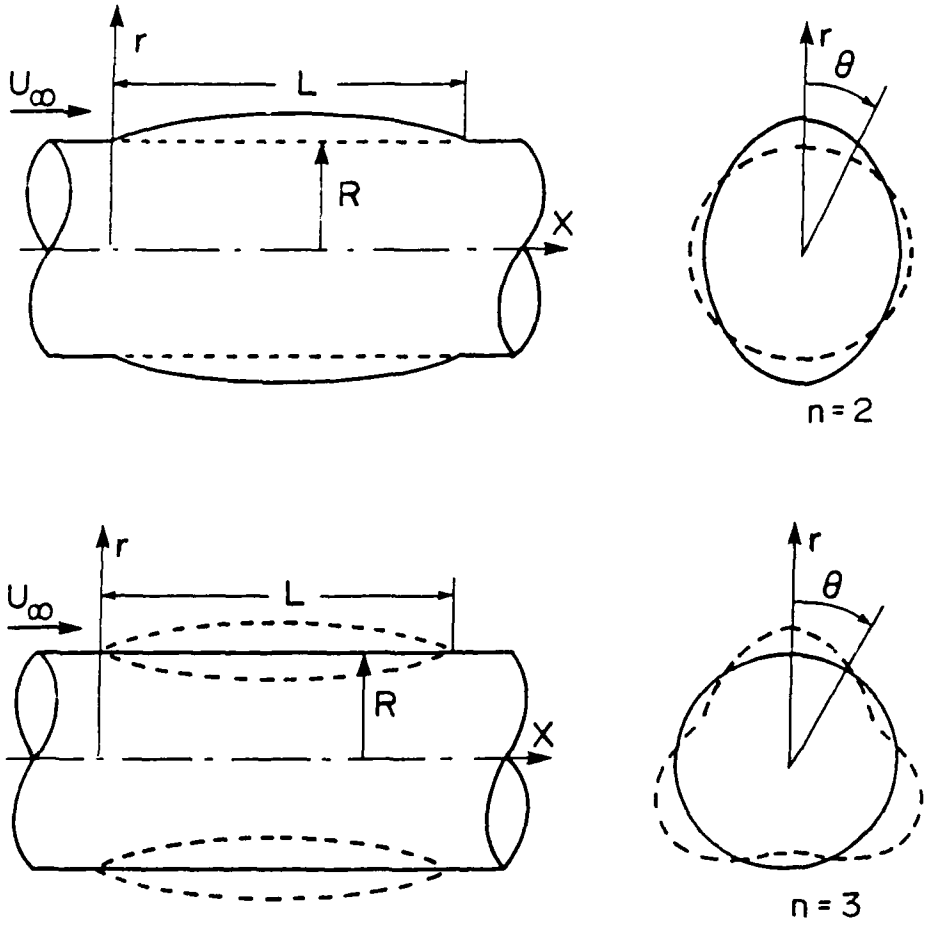

Fig. 55 Cylindrical Flutter Showing Two Vibrating Modes.

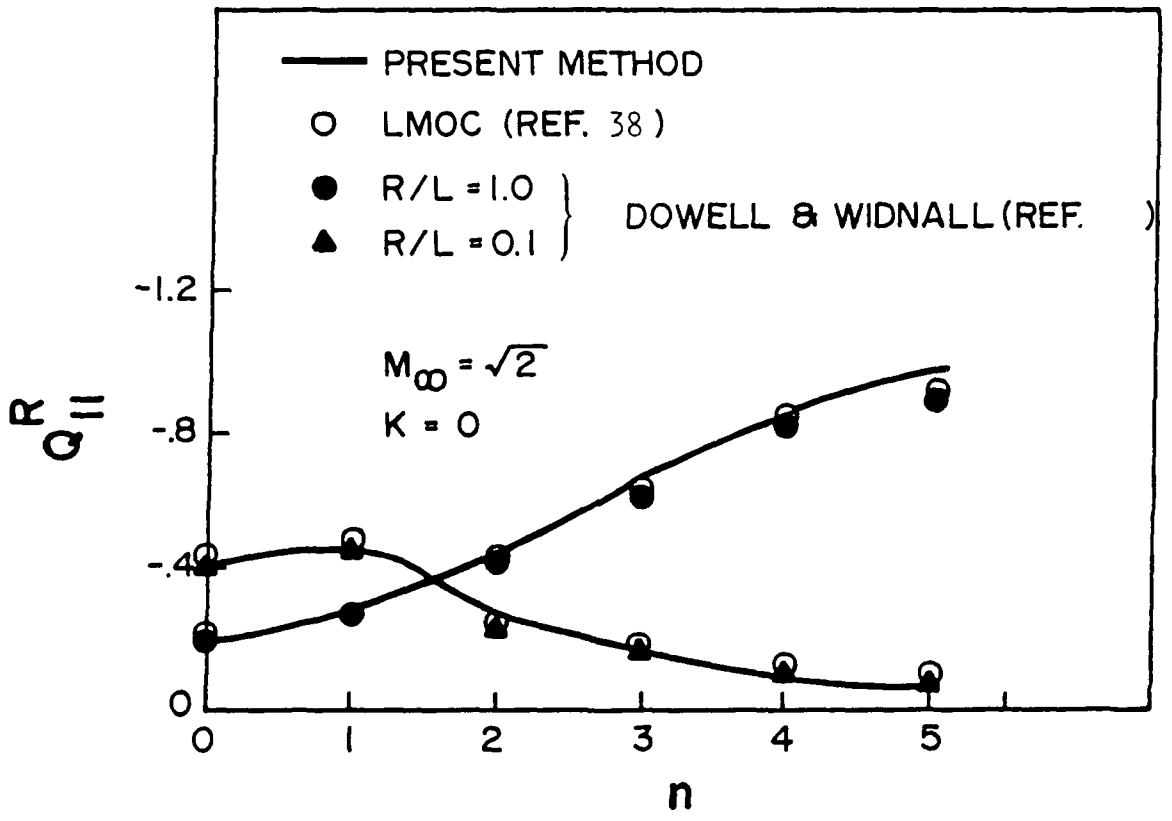

Fig. 56 Real Part of the Generalized Aerodynamic Force Q_{11} Versus Circumferential Mode Number.

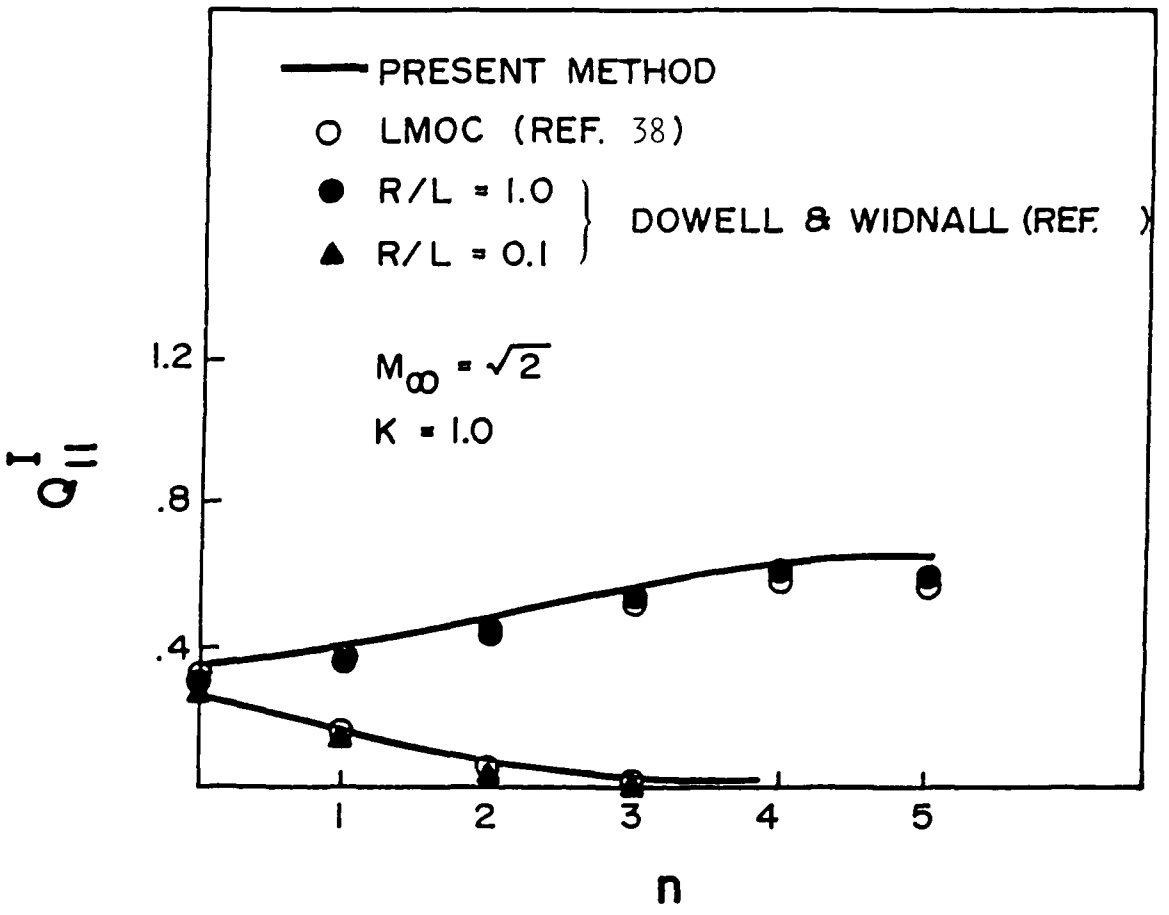

Fig. 57. Imaginary Part of the Generalized Aerodynamic Force Q_{11} Versus Circumferential Mode Number.

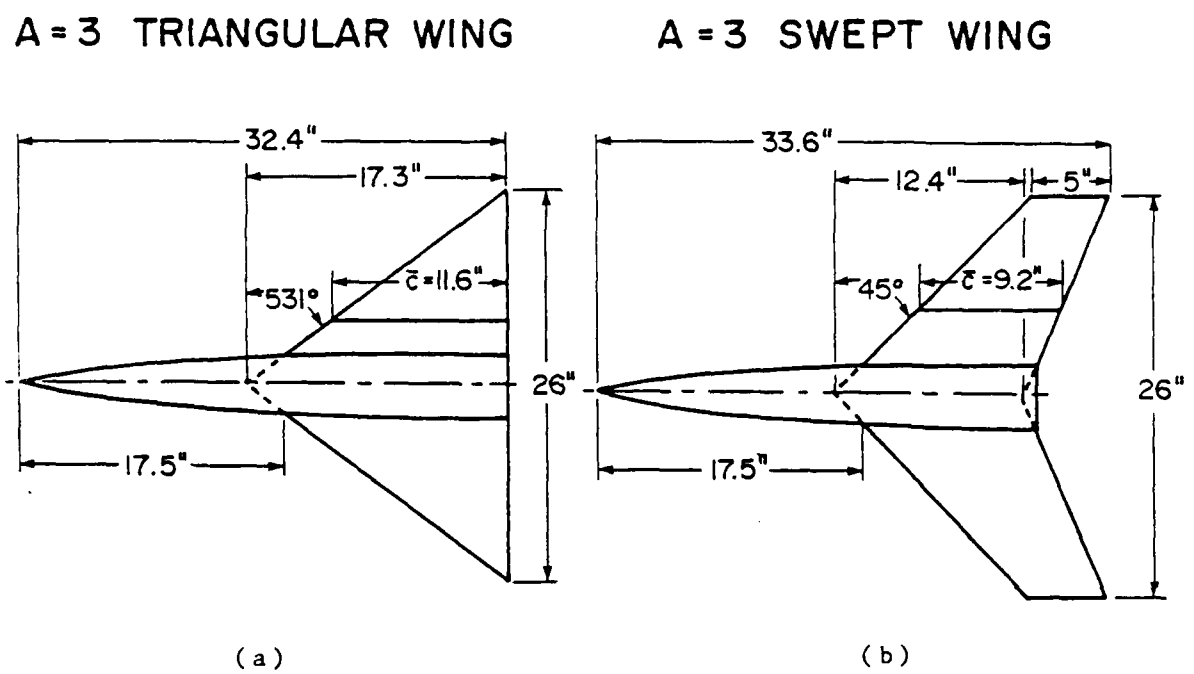

Fig. 58 Sketches of Wing-Body Configurations
a) Aspect Ratio AR = 3 Triangular Wing-Body
b) Aspect Ratio AR = 3 Swept Wing-Body

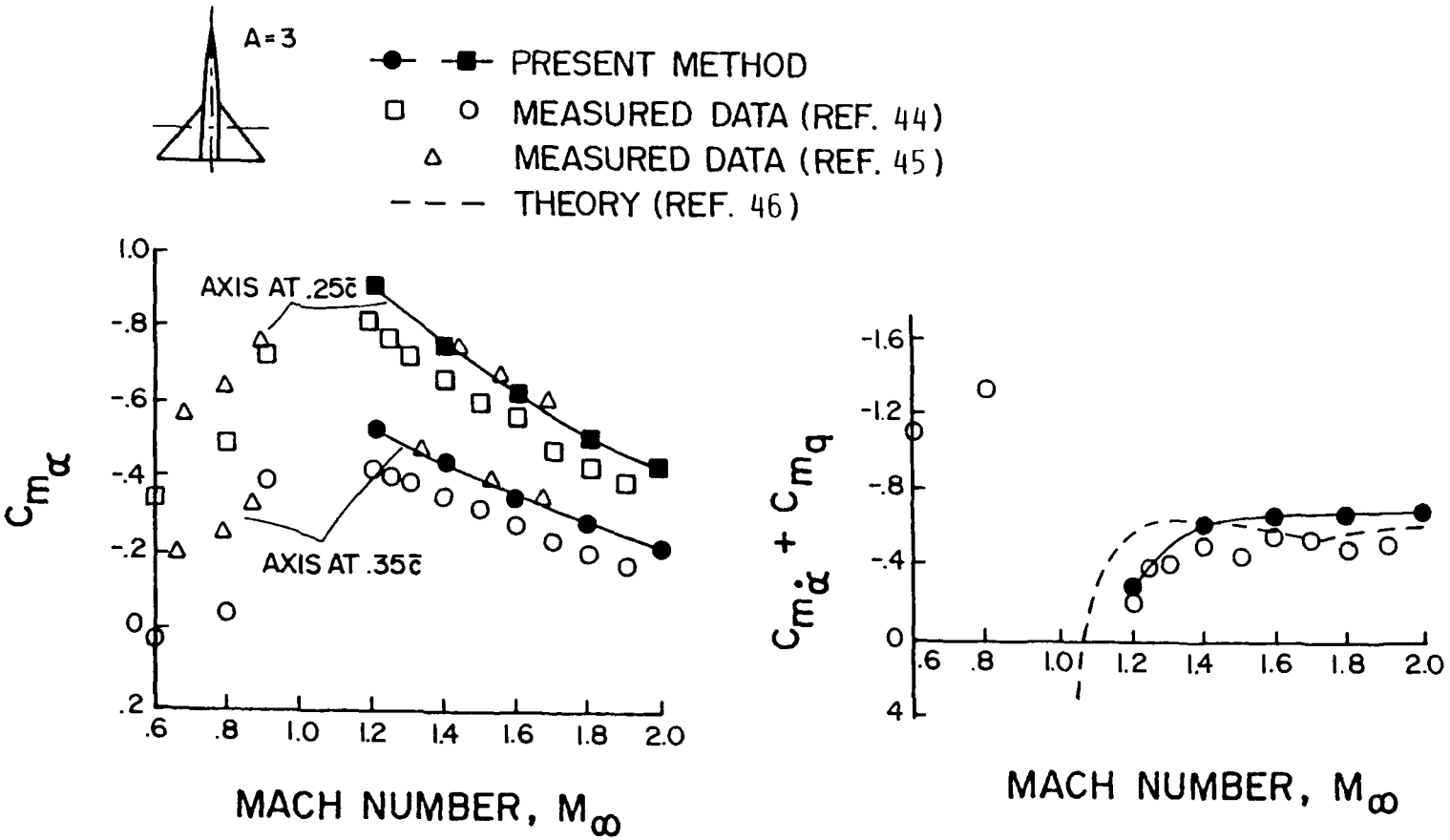

Fig. 59 Static and Dynamic Moment Derivatives for an Aspect Ratio AR = 3 Triangular Wing-Body.

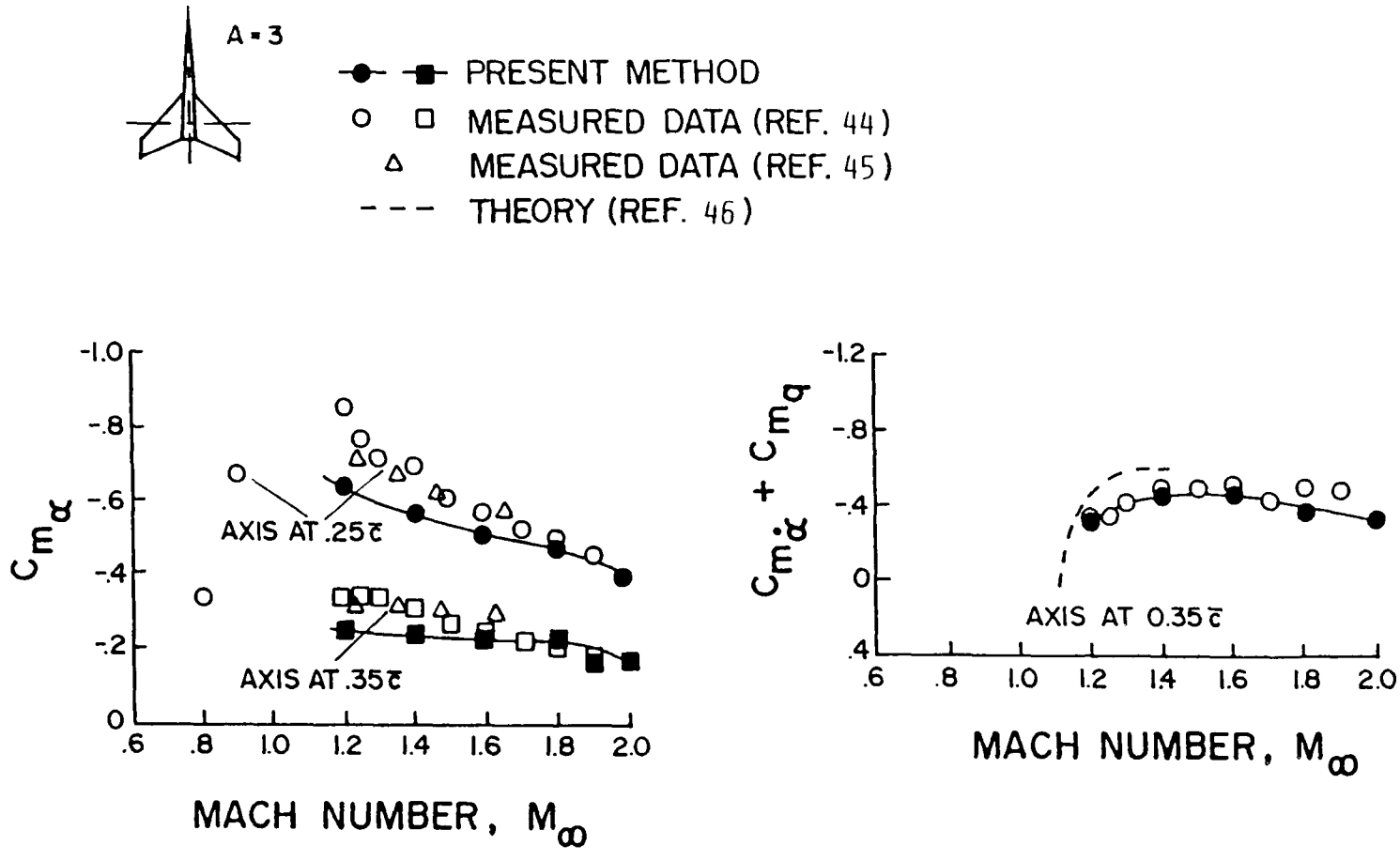

Fig. 60 Static and Dynamic Moment Derivatives for an Aspect Ratio AR = 3 Swept Wing-Body.

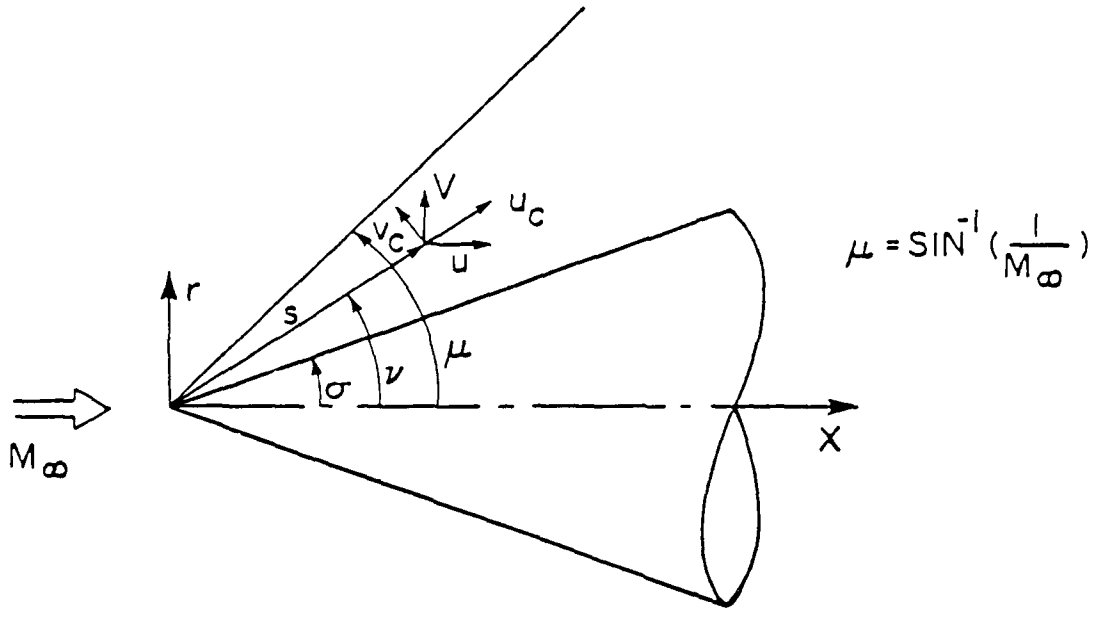

Fig. 61 Conical Coordinate and Cylindrical Coordinate Systems for a Circular Cone.